PALACKÝ UNIVERSITY OLOMOUC
Faculty of Science
Department of Physical Chemistry

Functional Groups on Carbon Nanomaterials: The Matter That Matters

Ph.D. Thesis

Kateřina Holá

Supervisor: prof. RNDr. Radek Zbořil, Ph.D.

Olomouc 2017

Declaration of the Author

I declare that I have written this thesis by myself using the cited references. Neither the thesis nor any of its part was previously used for obtaining any other academic degree.

Olomouc, April 2017

Kateřina Holá

Contents

Abstract

Carbon nanomaterials have a significant importance in materials science worldwide. Their superiority lies in the variability of their main building block, the C–C bond. This unit can build diverse sp^3 and sp^2-based nanoarchitectures and even covalently incorporate various non-metallic elements. All members of the carbon nanomaterials family (fullerenes, carbon nanotubes, nanodiamonds or graphene) possess extraordinary mechanical, optical, electronic or magnetic properties. In addition, their functionalization can dramatically boost their properties and improve scientific or technical importance in various applications. This dissertation gives a brief view how the functional groups can determine the application potential of current carbon nanomaterials. Mainly, the last frontiers of carbon nanomaterials, fluorographene (GF) and carbon quantum dots (CDs), are discussed in detail. The attention is paid to the functional groups of CDs and how they can affect CD photoluminescence. Similarly, the study focuses how the functional groups on GF can induce magnetism in its honeycomb lattice or boost its genosensing properties. The given results will clearly demonstrate that the functional groups on carbon nanomaterials are the matter that really matters.

1

Carbon Nanomaterials

Carbon nanomaterials have attracted enormous scientific attention in last three decades.[1–3] Since the first recognition of Buckminsterfullerene in 1985,[4,5] the exploring of new carbon nanostructures have witnessed an impressive growth thanks to their unique mechanical, electronic and optical properties; Figure 1 shows the breakthrough years in the discovery of the most significant carbon nanomaterials. In addition to the zero-dimensional material in the form of fullerenes or nanodiamonds, the carbon nanostructures possess also the one-dimensional nanostructures (nanotubes) and two-dimensional nanostructures (graphene). This fact, in combination with robust carbon chemistry, makes the carbon nanofamily the most variable framework for numerous applications.

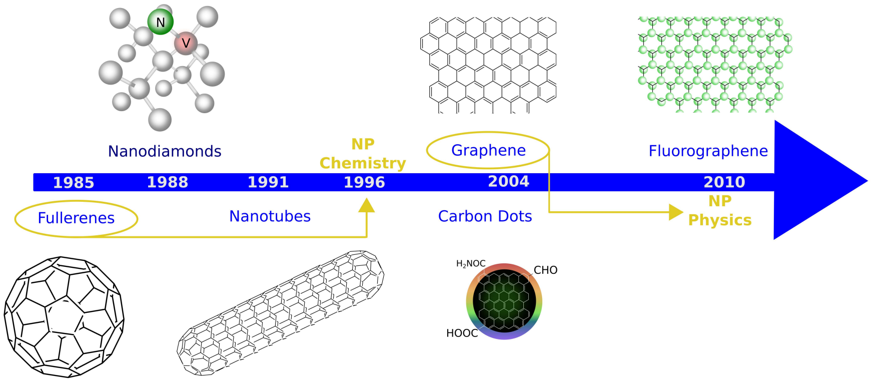

Figure 1. Timeline showing the most significant years in carbon nanomaterials´ development.* The Nobel prices in Chemistry and in Physics for discovery of fullerenes and graphene are there also highlighted.

---

* Other carbon nanomaterials as carbon nanohorns, carbon onions, carbon nanofoams, graphene nanosheets or nanoribbons and other allotropes are not included.

The exceptional properties of carbon nanomaterials are due to their main building block, the C–C bond. This robust bond possesses all of the important hybridization (sp^3, sp^2 and sp). It is a building block for graphite and diamond as well as for organic chemistry and biochemistry. Therefore, carbon nanomaterials are so unique; they are something in between organic chemistry and inorganic materials. They typically do not need a polymer/organic shell for stabilization/ functionalization as traditional metallic nanoparticles. Hence, their mechanic, optoelectronic or magnetic properties can be tuned also by incorporation of nonmetallic elements, like oxygen, nitrogen, sulphur, phosphorous, boron or fluorine. All these features provide to carbon nanomaterials a unique place in the nanoworld. The present work is focused on the two latest members of carbon nanomaterials, carbon quantum dots (CDs, section 2) and fluorographene (GF, section 3), with particular attention to the role of their functional groups. However, the following section also brings a very brief view of the most significant properties/applications related to functional groups of other members of this unique carbon family.

1.1 Fullerenes

The most important breakthrough in fullerene discovery came in 1985 when Kroto, Curl and Smalley were studying possible carbon structures formed in interstellar space.[5] Fortunately, the discovered molecule C_{60} was named fullerene and not ballene, spherene or carbonsoccer as the authors also suggested.[5] Up to date, many types of fullerenes (e.g. C_{70}, C_{76}, C_{82}, C_{88}) have been described.[6] The applications of fullerenes are very closely related to their physicochemical properties. The most recognized characteristics of this material is the ability to act as an electron acceptor or as a radical scavenger.[6] Therefore, fullerene finds its main applications in catalysis,[7] in photovoltaic cells[8] or as an antioxidant.[6,9] The antioxidant properties of fullerenes have been used in cosmetics, e.g. in sunscreen or “anti-aging” creams.[10] However, the potential risk of water pollution caused by fullerenes does not allow any commercial success so far.[11] Still, the application of hydrophilic derivatives of fullerene in biomedical field at academic level is very well established.[12] Fullerene exhibits antibacterial activity against several Gram-positive and Gram-negative bacteria and its antiviral activity was also demonstrated.[13–15] This material has also a potential as a radioprotecting agent for healthy tissue during radiotherapy or as a retardant of neurological damage during Alzheimer's disease.[16,17] Moreover, this wide spectrum of applications becomes even larger upon fullerenes derivatization.

The improving of physicochemical properties of fullerene by functionalization can be divided into many subcategories. In general, there are six categories of fullerene derivatives (Figure 2): endohedral fullerenes (modified internally), heterofullerenes, exohedral fullerenes (modified externally), open-cage fullerenes, fullerene salts and quasi-fullerenes.[18] The most significant categories are endohedral and exohedral fullerenes. The first mentioned with encapsulated metals (metalofullerenes) exhibit extraordinary electronic properties (small band gap) thanks to the unique charge transfer between the carbon cage and the metal.[19] They have been tested in spintronics[20] or as molecular cage for gadolinium in Magnetic Resonance Imaging (MRI).[21] The exohedral fullerenes are the widest category. There can be included the fullerenes with carboxyl or polyhydroxyl groups that provide better hydrophilicity making them suitable for biomedical use,[12] fluorinated fullerenes used as p-dopants

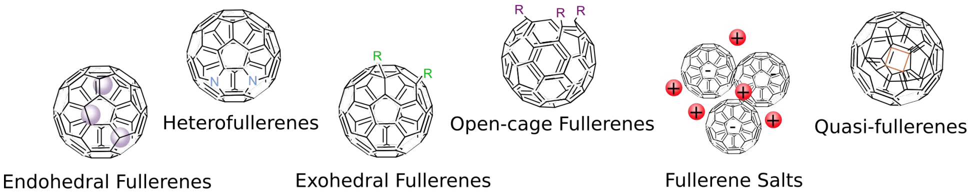

Figure 2. The main six categories of fullerene derivatives. Adapted according to ref. 18.

in optoelectronic devices,[22] fullerenes functionalized with various porphyrins as an ideal system mimicking the photosynthesis[23] and many others. All mentioned functionalizations of fullerenes have so far dramatically improved the scientific or technical importance of this material. It is obvious that the chemical functionalization of fullerenes drives strongly its application potential.

1.2 Carbon Nanotubes

The intense interest in carbon nanostructures after the discovery of fullerene led to the discovery of carbon nanotubes in 1991.[24] The arc-discharge evaporation method used for the production of fullerenes developed by Kratchmer *et al.* was also used for the first preparation of carbon nanotubes.[25] Nanotubes with diameter of 3–40 nm and length of more than 1 mm produced by this technique grew just on the negative end of the carbon electrode.[24] These cylindrical nanostructures appeared there in double-walled and multi-walled forms.[24] The other key parameter for the classification of carbon nanotubes is their chirality, that is the angle between the nanotube axis and the hexagonal pattern.[6] The most typical examples are zigzag, armchair and chiral patterns. The well recognized characteristics of carbon nanotubes are high flexibility and superelasticity in combination with remarkable strength.[26,27] Moreover, they also exhibit great conductivity and capacity for energy storage.[28] So far, carbon nanotubes are the most commercially valuable carbon nanomaterial mainly thanks to their mechanical properties. For example, they were used for the construction of the bicycle winning the Tour de France in 2005, their superhydrophobicity is used for hull ship coating and they can be found in printed electronics.[29]

The classification of carbon nanotubes derivatives is almost identical to the classification of fullerenes. The most recognized and used derivatives are carboxylated nanotubes with improved hydrophilicity[30] and also nitrogen- and boron- doped nanotubes.[31] The nitrogen-doped carbon nanotubes are typically prepared by chemical vapor deposition where the source of carbon is methane and N_2 or ammonia is used as the source of nitrogen. Precursors with carbon and nitrogen in the structure (for example pyridine or acetonitrile) can be also used.[32,33] The nitrogen atoms in the structure dramatically influence the electronic properties (the nitrogen-doped nanotubes have semiconducting properties)[34] but it can also boost the capacity of this material for lithium storage.[32] This is due to nitrogen defects in the walls connected with lithium diffusion into the whole structure of nanotubes (see Figure 3). The capacity can be even 10 000 times higher compared to non-doped material. These alkali-doped nanotubes can also exhibit very high hydrogen uptake for hydrogen storage.[35] As it can be seen, the derivatization/functionalization of nanotubes with various functionalities can have a very high impact on the application potential of this carbon nanomaterial.

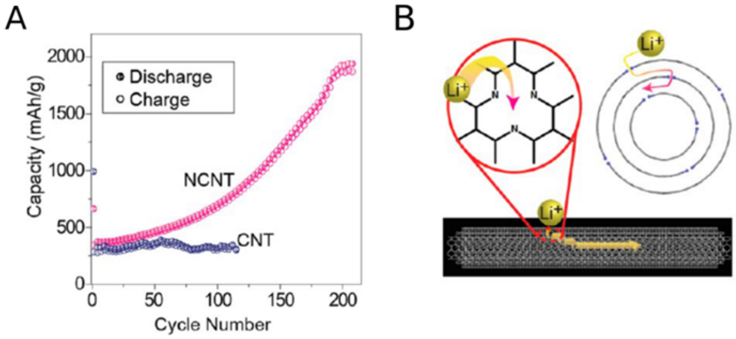

Figure 3. The capacity of nitrogen-doped carbon nanotubes (A) and the mechanism of lithium diffusion into the inner space of nanotubes (B). Reprinted with permission from ref. 32. Copyright 2012 of American Chemical Society.

1.3 Graphene

The latest "star" amongst the carbon nanomaterials is graphene. Graphene was already prepared in 1992 as a single layer of carbon honeycomb on platinum (111) surface and also as a layer on HOPG (highly oriented pyrolytic graphite) formed from decomposed diamond nanoparticles in 2001.[36,37] However, there was a general assumption that a single layer of graphene cannot be thermodynamically stable without a solid support. In 2004, Novoselov and collective came up with a simple mechanical exfoliation of HOPG and the isolated graphene started to be in a spotlight of the scientific community.[38] The extraordinary physical properties and potential applications portfolio of graphene is almost countless. It is worth to mention that graphene excels in mechanical stability, electronic properties and thermal conductivity.[6] However, the commercialization (e.g. flexible display screens) suffers from the difficult industrial preparation of single layer graphene with appropriate size. Still, many interesting physical phenomena have been observed in this material (e.g. quantum Hall effect,[39] Kerr effect[40] etc.), making graphene an excellent platform for the basic research.

The most important examples of covalently modified graphene derivatives are graphene oxide,[41] reduced graphene oxide,[42] graphane[43] and fluorographene (discussed in section 3).[44] Moreover, in addition to these types of graphene there exists graphene with heteroatoms in the structure (doped graphene)[45,46] and graphene with intercalated metals between the layers (graphite intercalation compounds are used as supercapacitators for lithium batteries).[47] All these subgroups have a significant importance in many applications. For example, graphene oxide is a subject of intense study because of its simple preparation, variable chemistry, excellent solvent dispersability[48] and it is also the most applied graphene in the biomedical field.[49] Graphane (hydrogenated graphene) has a potential as a material for hydrogen storage,[50] and also exhibits very weak room temperature ferromagnetic properties (0.006 emu.g^{-1}).[51] A very interesting magnetic behavior was also observed for nitrogen- and sulfur-doped graphene structures.[52,53] All mentioned derivatives have dramatically expanded the application portfolio of this material.

1.4 Nanodiamonds

The only sp^3 representatives of the nanocarbon family are nanodiamonds. The diamond lattice arranged in a cubic crystal is very different compared to the other honeycomb-based carbon nanomaterials.[54] One of the breakthrough in this field came in 1988 with the discovery of nanodiamonds in detonation soot.[55,56] A similar experiment was already made in 1962 but without any significant notice by the scientific community.[57] However, this material started to attract more scientific attention many years later with the preparation of fluorescent nanodiamond dispersions.[58–60] Except their hardness and chemical stability exploited for example in oil additives,[61] nanodiamonds possess excellent fluorescent properties resulting in a vast array of applications in the biomedical field. The most important functionality of fluorescent nanodiamonds is their post-preparatively induced nitrogen vacancy (NV) centers or also the silicon vacancy (SV) centers responsible for their stable photoluminiscence.[62] The wavelength of their fluorescence is related to the zero phonon line of their two charge states: NV^0 center at 575 nm and NV^- at 637 nm.[63] More importantly, they do not exhibit any photobleaching and have very low cytotoxicity.[60] Therefore, nanodiamonds can be considered as close relatives of carbon dots, which are discussed in the following section. Both materials find their main applications in the biomedical field (e.g. cell labelling, optical imaging or drug delivery).[64] Still, both have some limitations, like for example low amount of NV centers in nanodiamonds or low fluorescent quantum yields of carbon dots in the red region of the optical spectrum.

The functional groups of the surface of nanodiamonds can determine their photoluminiscence properties and also their applications. The surface groups and their environment can determine the stabilization of the NV^{-} centers which is connected with the intensity of their emission. This can be utilized e.g. in metal sensing[65] or in sensing of the charge of surrounding species.[66] In this way, the covalently attached fluorine atoms can also boost the emission at 637 nm.[67] From the given examples, it is clear that the role of surface functional groups in nanodiamonds can attract notable interest.

The discussed carbon nanomaterials have a significant importance in materials science worldwide. As a general remark, their properties and importance are not determined only by their peculiar structural features, but also by the different functional groups directly connected to their C-C lattice. This is also the reason why carbon nanomaterials are so special. Functional group can boost their application potential as shown in the previous examples. The following section is devoted to carbon dots, and in particular the influence of the functional groups on their fluorescent properties is discussed in details.

2

Carbon Dots

Carbon quantum dots (CDs) were firstly synthetized in 2004.[68] They have been isolated as an impurity during the purification of single walled carbon nanotubes prepared from arc-discharge soot.[68] Since their discovery, CDs have attracted huge scientific attention thanks to their extraordinary fluorescent properties in combination with excellent biocompatibility.[69] They have been tested as a potential non-toxic variant of traditional quantum dots based on heavy metals in many applications. So far, the main attention has been paid to their excitation wavelength-dependent emission (this characteristic is illustrated in Figure 4). The understanding of the origin of their photoluminescence behavior is more complicated than in the case of other semiconducting inorganic fluorescent materials. This happens because CDs are a combination of inorganic graphite and large aromatic organic molecules with oxygen-rich edge functional groups. As a result, the fluorescence of CDs can be determined not just by their size or dopants as in the case of semiconductor quantum dots (e.g. CdSe) but also by their "surface-organic chemistry".[70,71] Therefore, the surface functional groups play a critical role in their photoluminescence.

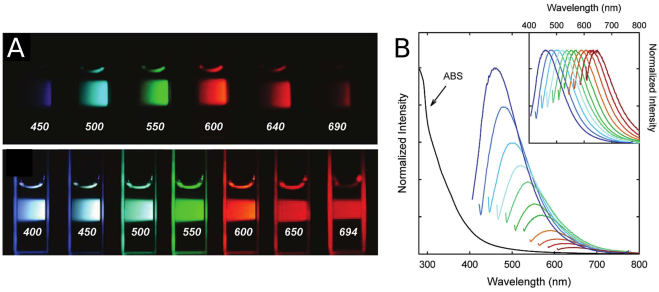

Figure 4. The characteristic fluorescent features of CDs: excitation-dependent emission. The solution of CDs exhibit all colors of visible spectrum depending on the excitation wavelength (A–B). Reprinted with permission from ref. 72. Copyright 2006 of American Chemical Society.

2.1 Structure of Carbon Dots

Under the general denotation “CDs” three subcategories can be identified: Graphene dots, carbon dots and polymer/polymeric dots.[73] The first ones are typically prepared directly from graphene or other graphene-based precursors. They have the characteristic graphene honeycomb lattice with lateral dimension up to 100 nm while their high profile does not exceed four or five graphene layers.[74–77] The second and most typical group is carbon (nano)dots, sometimes denoted as carbogenic dots, which are semi-spherical and with dimension not bigger than 10 nm, typically 2–3 nm. Their structure just copies the structure of graphite: reflected by the interlayer distance of 335 pm (see Figure 5). The polymer dots are typically cross-linked polymers with a very small carbon core or sometimes just with cross-linked organic fluorophores formed during decomposition of the precursors. This subcategory originated from the knowledge that some preparations of CDs (e.g. thermal decomposition of citric acid and ethanolamine) form highly fluorescent citrazinic acid under

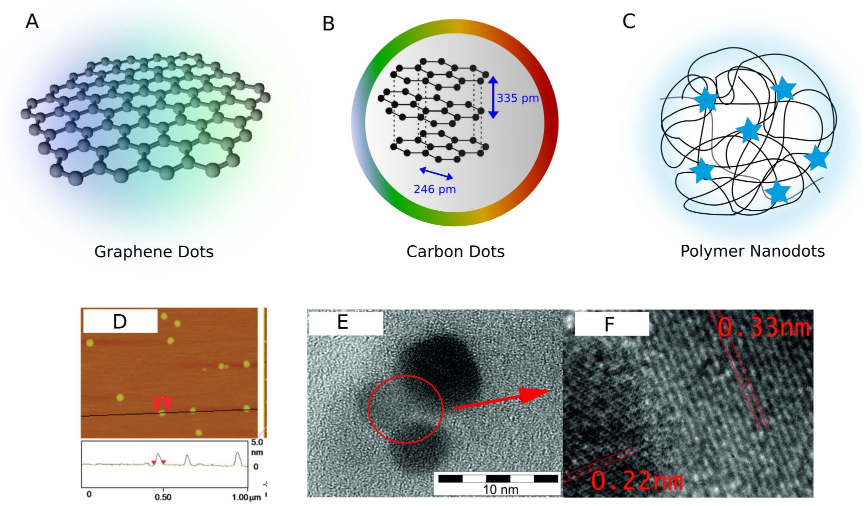

Figure 5. Schematic representation of carbon based nanostructures of graphene dots (A), carbon dots (B) and polymeric nanodots (C). AFM image of graphene dots: 3 nm high and 60 nm wide (D). TEM images of spherical carbon dots with the characteristic graphite lattice (E, F). Reprinted with permission from ref. 76,80. Copyright 2011 of American Chemical Society and Elsevier B.V.

certain conditions.[78,79] This organic agent has fluorescence emission typically at 450 nm and quantum yield over 70%. The particles with these properties were lately denoted as polymeric nanodots.[81,82] The crystallinity of this dead branch of CDs is very low. Therefore, this subcategory will not be discussed in further text.

The chemical composition of CDs is strongly dependent on the preparation route as it can be seen in Table 1. The amount of carbon in the structure can span from 40 to 80 %. Therefore, it is obvious that the high amount of oxygen (hydroxyl, carbonyl, carboxyl, epoxy groups etc.) cannot be located just on the oxidized surface of CDs but is also present inside the graphitic core similarly as in graphene oxide. Apart from the carbon and oxygen, CDs can contain also other various dopants,[71] e.g. nitrogen, boron,[83,84] sulfur[85] and chlorine.[86] These elements are usually incorporated inside/on the structure during the bottom-up synthetic strategies from various precursors and are the most important factors determining their optical properties.

Table 1. Chemical composition of graphene dots and carbon dots prepared by different synthetic routes (bottom-up strategies are highlighted by grey color; top-down strategies are not highlighted). The C/O/N composition is given in percentage according to XPS analysis. The hydrogen amount in the samples is not specified.

Synthetic strategy	**Size***	**C**	**O**	**N**	**Emission(QY)**	**Ref.**
Graphene dots						
Thermal treatment of GO in DMF	3nm/~1 nm	83.1	15.0	1.9	520 nm (35%)	87
Thermal treatment of GO in NH_3	8 nm/~2 nm	79.4	18.3	2.3	520 nm (n.r.)	88
Hydrothermal treatment of GO	3nm/~2 nm	56.5	43.5	-	510 nm (1.2%)	89
Pyrolysis of CA	15 nm/~1 nm	48.1	51.9	-	460 nm (9%)	90
Carbon dots						
Reflux of candle soot in nitric acid	2–6 nm	59	37	4	520 nm (3%)	91
Dehydrogenation of glucose in conc. acid	4–10 nm	74	25	1	600 nm (7%)	92
Asp+glucose microwave decomposition	4.5 nm	57.1	39.4	3.5	560 nm (35%)	93
Microwave decomposition of CA and urea	1–5 nm	41.5	34.7	21.8	515 nm (40%)	94

* The first size value was determined by TEM, the second value is the graphene dots thickness obtained by AFM.

QY – quantum yield, n.r. – not reported, GO – graphene oxide, CA – citric acid, Asp – aspartic acid.

2.2 Synthetic Strategies for CD Preparation

Analogously to all nanomaterials, CDs can be also prepared by top-down or bottom-up synthetic strategies. The top-down pathways typically start from graphite,[72] graphene oxide, graphite rods,[95] carbon soot (arc-discharge or candle soot),[96] or also from carbon nanotubes[97] or fullerenes.[98] The cutting processes employed to achieve the desired size can be based on heating (reflux) of oxidized precursor in nitric or other strong acid,[96] or on thermal treatment of graphene oxide in presence of hydrazine,[99] DMF,[87] ammonia[88] or just water[89] (typically performed in autoclave). Electrochemical cutting of graphite rods in presence of $K_2S_2O_8$ is also very often used.[100–102] It should be also noted that several of these synthetic strategies do not directly produce fluorescent CDs.[72] Therefore, the prepared material has to be subsequently passivated with a polymer shell (e.g. PEI, PEG-NH_2) to induce bright photoluminescence.

Up to date, many bottom-up synthetic pathways have been developed to prepare highly luminescent CDs. Most importantly, the first bottom-up synthetic strategy was developed by our colleague Athanasios Bourlinos in 2008.[103,104] His synthetic pathway was based on solid state pyrolysis (thermal oxidation) of citric acid and amino-undecanoate at 300 °C. Since that time, the bottom-up CD preparation has attracted enormous scientific attention because of easier preparation and also simple influence of surface properties by the chosen precursor. The general strategy is based on thermal decomposition or dehydration of proper organic precursors able to form carbonized material with aromatic graphene-like domains. The synthetic strategies differ mainly in the organic precursors. Still, there are just a few synthetic approaches: (*i*) thermal decomposition/pyrolysis of organic precursors in the solid state (220–300 °C, crucible in the oven);[105] (*ii*) hydrothermal or solvothermal decomposition (160–220 °C; heating of a solution in the autoclave);[85] (*iii*) dehydration of precursors by reaction with P_2O_5[106] or by heating in strong acids[92] and (*iv*) decomposition in a microwave reactor or just by heating in a microwave oven.[107]

The most typical precursor for the preparation of CDs by bottom-up approach is citric acid. This compound easily forms graphene-like aromatic domains during dehydration thanks to its structure presenting 6 carbon atoms.[108] However, glucose or other monosaccharides,[107] amino acids[93] and aromatic compounds (e.g. derivatives of gallic acid, phenylendiamines or pyrene)[109–111] are also very often used. These “core-forming” precursors are very often combined with various amines (ethanolamine, ethylenediamine, urea etc.), which dramatically improve the fluorescent properties of the isolated particles.

Of great importance is also the post-preparative purification of the obtained particles to remove low molecular weight impurities/byproducts. However, the typical size of CDs (2–3 nm) is the most important limiting factor of the purification. This size is approx. 2–3 kDa in protein terminology (the molecular weight of CDs is not consistent with the protein molecular weight because of different material density).[112,113] Therefore, it is not possible to purify them by centrifugation, unless ultracentrifugation is used. However, they can be purified by dialysis with cut-off 1–2 kDa. Even though dialysis is the most commonly used technique for CDs purification, the dialysis tubing at this value of cut-off can very easily burst because of osmotic pressure. Therefore, the purification of CDs is not performed at all in many studies, apart from the removal of larger agglomerates.[85,114] However, further techniques such as ultracentrifugation (Amicon® Ultracel: 3 kDa), size-exclusion separation on Sephadex® or separation in silica column can be used.[115]

2.3 Physical Properties and the Role of Functional Groups

The most important physical property of CDs is their photostability. The comparison study between fluorescein isothiocyanate, nanoprobe CdTe and CDs showed that CDs exhibit very low photobleaching.[93] Fluorescein isothiocyanate was completely quenched within ten minutes excitation, while CdTe retained only 30% of the original intensity within twenty minutes and CDs still exhibited more than 90% of the original intensity after one hour excitation under the same conditions. This behavior was also observed for graphene dots[111] and is a very favorable property for cell labelling. Apart from the high photostability, CDs also exhibits good dispersibility in various solvents up to 40 mg.mL^{-1} (e.g. DMF, DMSO, methanol, water etc.) and chemical inertness.[96] In previous studies, we also reported that CDs shows nonlinear optical response.[109,116] Together with the properties of CDs mentioned above, their up-conversion fluorescence (two-photon excitation) has been often reported in the literature.[87,117–120] However, the readers have to be very careful because this property can be caused by “normal” excitation coming from leaking of the second diffraction in the monochromator.[121] Therefore, the up-conversion fluorescence is not necessary an attribute of CDs.

CDs exhibit strong absorption in the UV range of the electromagnetic spectrum with a tail extending to the visible range.[69] Until now, the π–π^* transition at 280 nm and n–π^* transition around 350 nm were identified.[122] More importantly, the particles with red-shifted emission also exhibit more significant absorption in the visible part of the spectrum as it can be seen in a study by Bhunia *et al.*[92] This lower energy absorption can be attributed to the narrowing of the CD bandgap.

The most interesting feature of CDs is their fluorescent property, a property which is strongly influenced by functional groups and chemical composition.

The functional groups can determine the main fluorescent emission, the quantum yield and also whether the emission is dependent on the excitation wavelength or not (see Figure 4 above). The main functionalities determining the fluorescence properties of CDs are depicted in Figure 6.

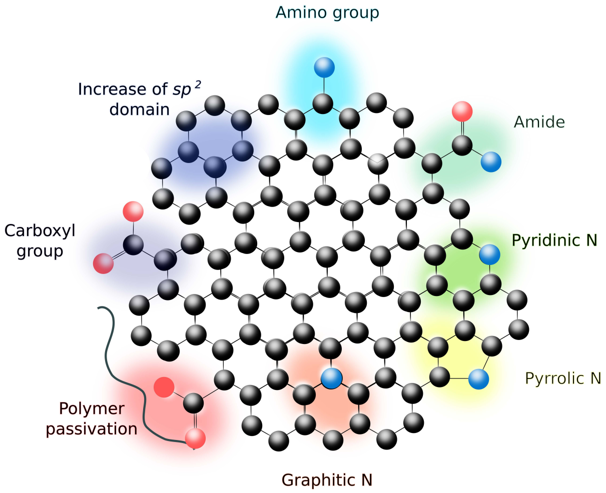

Figure 6. Schematic representation of the most important functionalities of CDs that can impact their photoluminescence.

2.3.1 Red-shift of CD Fluorescence

Many types of CDs with blue, green and more rarely yellow fluorescence have been prepared. Still, there are just few synthetic strategies that can lead to red fluorescent CDs. These particles are particularly suitable for biomedical applications because red light has the best tissue penetration. In addition, red CDs can provide the missing building block for a full-color emitting spectrum, e.g. for white light emitting diodes. Up to date, there are two known general features that can induce red fluorescence in CDs (see Figure 7). The first one is an increase in the size of sp^2 domain of CDs. The second one is a higher degree of surface oxidation. Both of these cases can be illustrated with the following examples.

The red fluorescence was often observed in graphene oxide.[123–127] Still, a higher/longer oxidation of the material induced a reduction of the sp^2 domains of graphene connected with the blue-shift of the fluorescence. For example, Hens *et al.* reported oxidation of HOPG in a mixture of sulfuric and nitric acid (3:1) at 128 °C.[127] The obtained graphene oxide exhibited red fluorescence after 20 minutes of treatment, orange fluorescence after 100 minutes and yellow after 2 hours.[127] Further size reduction of this material always resulted into graphene dots with blue emission.[128,129]

The size of the isolated sp^2 domains is also the dominant factor for red fluorescence in CDs in analogy to traditional semiconductor quantum dots.[130] Up to date, there are only two studies reporting the successful preparation of carbon dots or graphene dots with sufficient size of sp^2 domains exhibiting red fluorescence. Bhunia *et al.* reported the preparation of blue, green, yellow and red fluorescent CDs obtained by heating of glucose in concentrated acids (sulfuric and phosphoric acid).[92] The increase in size of CDs was significantly reflected in the increase of the emission wavelength. Tan *et al.* reported electrochemical exfoliation of graphene; the graphene dots prepared in this way emitted at 610 nm, with a size of 3 nm and sp^2 domain without any defects. The increase in time of the electrochemical oxidation process resulted in graphene dots with yellow, green and blue emission due to more defects in the sp^2 domains caused by oxidation.[131]

A higher surface oxidation of CDs surface can be also connected with red-shifted fluorescence. This fact was clearly shown in the studies of Wei *et al.*[132] and Ding *et al.*[133] In both studies, a mixture of CDs exhibiting almost full-color emission was fractionalized on a column according to the charge or the hydrophilicity. As the result, the fraction with the most negative charge in the study by Wei *et al.* exhibited orange fluorescence. Similarly, the most hydrophilic fraction with the highest degree of surface oxidation in the study of Ding *et al.* emitted in the red region at 625 nm. The observed effects are probably based on the fact that the surface functional groups (carboxyl) induce significant local distortions (emissive traps) resulting in a lowering of the emitted energy.[126] Therefore, tuning of the surface oxidation seems to be one of the suitable strategies to reach the fluorescence of CDs in the red region of the spectrum.

Very recently, we revealed a third strategy how to induce red fluorescence in CDs. This strategy is based on doping of CDs with graphitic nitrogen. The details are given in section 6 and appendix C (yes, this is an advertisement for these sections).

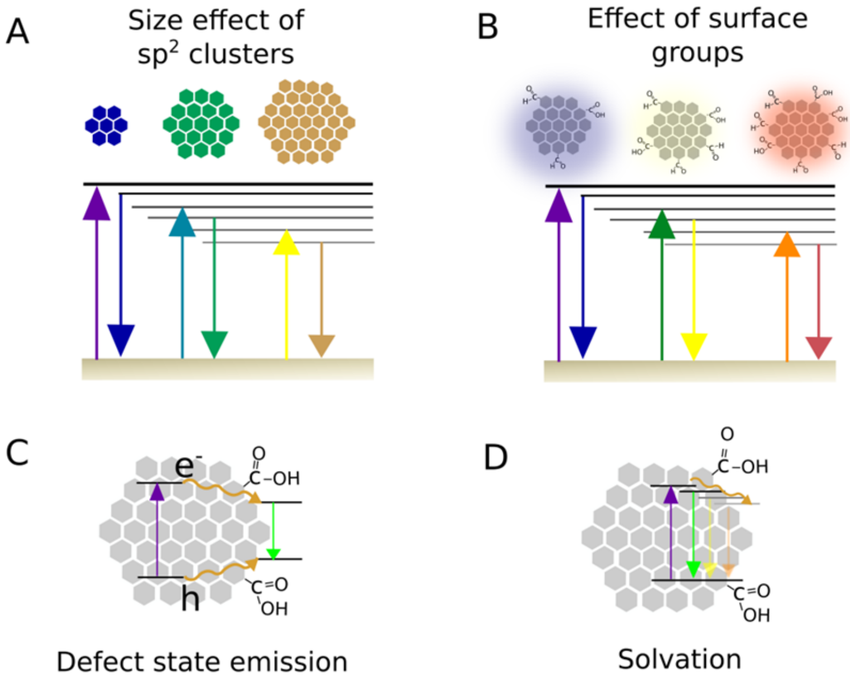

Figure 7. Schematic illustration of physicochemical phenomena inducing the red-shifted emission and excitation-dependent emission in CDs.

2.3.2 Excitation-dependent Emission

The excitation-dependent emission is probably the most studied phenomenon of CDs. It can be an intrinsic property of single CDs or it can be also caused by the fact that the material obtained from the synthesis is a mixture of various carbon dots as was demonstrated in the previous examples of CD fractionalization by Wei *et al.* and Ding *et al.*[132,133] Up to date, various explanations have been proposed in the literature and not a single one came with clear statement. Fu *et al.* reported the embedment of several polycyclic hydrocarbons (pyrene, antracene, perylene) in polymer particles.[134] This strategy mimics the composition of small graphene layers of CDs and also a possible reabsorption of light between the layers. The model system replicated the properties of typical CDs and the authors concluded that the excitation-dependent emission can be caused by self-trapping and by the Stokes shift of stacked polycyclic hydrocarbons (graphene layers in CDs). In other words, according this study the excitation-dependent emission is an intrinsic property of the CD core.

Moreover, more studies reported that the excitation-dependent emission is caused by the presence of various CDs in one sample,[135] in particular of CDs with various size (size of sp^2 domains)[68] or with different degree of surface oxidation.[100] Because both of these parameters can red-shift the fluorescence emission as was explain in the previous section.

2.3.3 The Role of Surface Groups in CD Photoluminescence

The role of carboxyl groups or other electron-rich surface groups in the fluorescent properties of CDs is very complex and fundamental. They can be (*i*) the origin of photoluminescence in CDs,[136] (*ii*) induce the excitation-dependent emission by the action of surface oxidation or by solvation[137] and/or act as (*iii*) surface emissive traps which can red-shift the fluorescence emission.

(*i*)

Nguen *et al*. have reported the preparation of CDs by laser ablation of graphite in water.[136] The particles the lateral size of approx. 2 nm, were not fluorescent and the amount of C–O groups was of only 3.6% (C=C bond amounted to 96.4%), according to high resolution C 1s XPS spectrum. These particles were afterwards oxidized by UV light under oxygen bubbling. The particles obtained after 2 hours of oxidation had hydroxyl and carbonyl groups on the surface and emitted at 430 nm and 335 nm. The longer oxidation time (4 hours) resulted in higher amount of hydroxyl groups and more intense emission at 430 nm. The authors concluded that the fluorescence of CDs is induced by surface functional groups. This phenomenon can be also confirmed by the fact that one of the first prepared CDs exhibited fluorescence properties just after surface passivation with PEG or PEI probably due to a higher amount of electron-rich elements on the surface.[96]

(*ii*) + (*iii*)

Our previous study reported the effect of surface groups on CD photoluminescence (section 4, appendix A). We prepared CDs functionalized with lauryl groups on the surface, that exhibited non-shifting properties and with fluorescence in the blue region of the spectrum. The surface lauryl chains were cut down by de-esterification and the particles afterwards exhibited the typical excitation-dependent emission and 40 nm red-shift in the main emission wavelength compared to the particles before de-esterification (for details see section 4 or appendix A). The red-shift can be explained by energy-losing electron-hole pair radiative recombination on the carboxyl rich surface (for better understanding see Figure 7C). The excitation-dependent emission can be then an effect of different surface oxidation but it can be also due to solvation of the surface groups (Figure 7D).

The correlation between the excitation-dependent emission and solvation was described for fluorescent graphene oxide (Figure 7D).[138–140] The modified graphene oxide exhibited fluorescence independent from the excitation wavelength in a non-polar solvent (pentane). However, very strong excitation-dependent emission was observed when the material was dispersed in water because of a slowdown of the solvation dynamics.

(*iii*)

As was previously shown, the surface functional groups can red shift the florescence emission. In our previous study discussed above, the reason was the surface carboxyl groups generating a 40 nm red shift (section 4; appendix A). Similarly, oxidized graphene dots in the study by Zhu *et al.*[137] emitted at 516 nm, while after reduction the particles emitted at 430 nm. However, this fluorescence shift was also observed for amino groups on graphene dots (28 nm in a study by Jin *et al.*[99] and 115 nm in a study by Tetsuka *et al.*[141]). In all these studies, the observed effect was attributed to the fact that the red-shifted emission to green originates from the surface defects (defect state emission) while the blue emission is the intrinsic state emission from the carbon core. Still, all of these observed effects can be mechanically explained by schematic Figure 7C, as we also concluded in our previous work (section 4; appendix A).

From the given examples, it is clear that the role of surface groups in CD photoluminescence is not trivial. The examples supplied here, chosen from hundreds of mechanistic studies, can maybe contribute to shed a light on this complex topic. We also hope that the reader is not tired from really detailed analysis of CD photoluminescence because we go further.

2.3.4 Increase of Quantum Yield

The increase in the CD quantum yield can be also often attributed to the surface functional groups. This increase can be caused by the fact that some of these groups can induce CD photoluminescence as shown in section 2.3.3 (*i*). However, the reader should be very careful because some super high quantum yields can be induced by organic molecules like citrazinic acid coming from the precursors embedded on the surface.[78] Therefore, some studies reporting quantum yields over 90% in materials obtained from pyrolysis of citric acid and e.g. ethanolamine can be possibly misleading.[108]

2.4 Applications of CDs

The applications portfolio of CDs includes biomedical applications, light emitting diodes, photocatalysis, water splitting and many others. More details can be found in our review paper (section 5, Appendix B). We would like to highlight just two of our recent papers in which the influence of functional groups in the biomedical applications is discussed.

It was previously reported that CDs exhibit high biocompatibility and are very often used for cell labelling.[142] In several studies, it was demonstrated that they enter the cell via an endosome-mediated pathway.[143,144] However, we also showed that strongly positive surface charge can induce penetration of CDs in to the cell nucleus. We have prepared CDs with quaternary ammonium on the surface with +53 mV surface charge.[145] These particles were observed in cell nucleus of mouse fibroblast NIH/3T3 after 4 hours of labelling. We also reported a similar observation for CDs with amino groups on the surface while the particles with negative or neutral surface charge were observed only in cytoplasm.[80] The penetration of CDs into the cell nucleus can have a fundamental effect for further application of CDs (e.g. in photodynamic therapy). These cases can demonstrate that the surface functional groups are most certainly highly influent, especially for biological systems.

3

Fluorographene

The first isolation of fluorographene came in 2010 when, nearly simultaneously, several groups reported the preparation of this material. The synthetic pathway by Nair *et al.*, Robinson *et al.* and Cheng *et al.* was based on fluorination of graphene sheets.[146–148] Vice versa, Zbořil *et al.* and Withers *et al.* reported the exfoliation of florinated graphite as alternative preparation method.[149,150] A broad attention has been paid to the electronic properties of fluorographene. Fully fluorinated graphene is a wide bandgap semiconductor, almost insulator.[148] Hence, the bandgap can be tuned by the degree of fluorination. This material also exhibits high thermal stability, even higher than its 1D polymeric analogue: teflon (fluorographene starts to decompose above 400 °C, teflon already at 260 °C).[146] The 2D structure and physical properties make fluorographene a promising material for various electronic devices.

Generally, there are two more commonly used synthetic strategies for fluorographene preparation.[151] The first one is based on fluorination of graphene by strong fluorination agents, e.g. atomic fluorine created from decomposition of XeF_2.[147] In this type of synthetic pathways, the degree of fluorination can be driven by the reaction time.[146] The second route is based on the exfoliation of fluorinated graphite by ultrasonication in various solvents (sonochemical exfoliation).[152] Fluorinated graphite is commercially available and the exfoliation procedure is easy to handle. The most suitable solvents are DMF, NMP and chloroform.[152] However, the yields are very low and the solvent can cause partial defluorination.

The structural properties of fluorographene (C_1F_1) are very similar to those of graphene, but with a substantial difference ascribed to the covalent attachment of fluorine atoms changing the sp^2 carbon hybridization into sp^3.[153] This preserves the hexagonal symmetry but completely affects the local structure.[154] It also induces complete loss of π-conjugated electrons with consequent loss in conductivity. Full fluorination also results in a total change in color of this material; florographite/fluorographene is white/grey. A further consequence is that fluorographene is non-active in Raman spectroscopy , and the typical G- and D-band of graphene are no longer visible.[146] The C-F bond has a semi-ionic character with dissociation energy of fluorinated organic molecules.[155] Noticeable are also the magnetic properties of fluorographene. Nair *et al.* reported that the point defects (fluorine adatoms) can carry magnetic moments with ½ spin.[156] Up to date, fluorographene was mainly studied for its physical phenomena and the potential applications are still in the state of development.

The most frequently used derivative of graphene for chemical modification and tailoring of properties is graphene oxide. However, the exact chemical composition of this derivative can be very variable and non-specific (hydroxy, epoxy, carbonyl, carboxyl groups). On the other hand, fluorographene is a better defined material, with only one type of bond: C–F. Therefore, it seems to be a suitable precursor for chemical functionalization and tailoring of graphene properties. We have recently developed the first synthetic strategy how to utilize the C–F bond for nucleophilic substitution in fluorographene. We used this strategy for attachment of sulfhydryl and hydroxyl groups to fluorographene lattice. Both of these new derivatives had advantageous properties compared to graphene or to the fluorographene precursor induced by the functional groups: for example the thiofluorographene was suitable for genosensing and the hydroxofluorographene exhibited antiferromagnetism at room temperature. Both of these examples are discussed in more detail in the sections 7 and 8 (appendix D and E). More importantly, the covalent functionalization of fluorographene can shift this theoretically studied material towards its future applications.

Author´s Comment

The following sections (4-8) briefly summarize the most significant publications of the author in the discussed field. The results reported are mostly dealing with the understanding of CD photoluminescence and the preparation of new graphene derivatives starting from fluorographene. In all the cases, it is shown that the functional groups can determine the physical properties and thus also the applications of these materials.

Section 4 discusses the excitation-dependent emission and the effect of the graphitic core and the surface carboxyl groups on the photoluminiscence of CDs. Section 5 briefly summarizes the applications of CDs. The role of graphitic nitrogen on the photoluminescence red-shift is described in section 6. Thiofluorographene, a new material derived from flurographene, is described in section 7 together with its application in genosensing via impedance spectroscopy. Section 8 is devoted to hydroxofluorographene which exhibits as the first non-metallic graphene derivative antiferromagnetic behavior at the room temperature.

4 Photoluminescence Effects of Graphitic Core Size and Surface Functional Groups in Carbon Dots: COO^- Induced Red-shifted Emission[A]

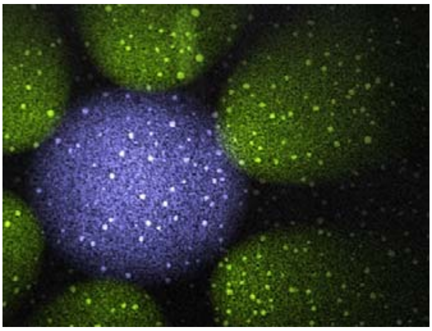

Control of the size of carbon dots (CDs) in bottom-up synthetic procedures is a very challenging issue. We approached the problem from a molecular point of view in order to be able to tune the size of CDs by the selection of a precursor. Depending on the gallic acid derivative used, CDs with different alkyl groups (methyl, propyl, lauryl) on the surface were obtained by isothermal heating at 270 °C. This precursor-derived approach enables the control over both the size and the CD lipophilicity. The prepared CDs were also used for demonstrating the role of their surface carboxylic groups on the photoluminescence properties. The alkyl chains on the CDs surface were converted to carboxylate groups via a mild base hydrolysis. The photoluminescence differences in CDs with alkyl and carboxyl groups were discussed in detail. This study clearly demonstrated the impact of carboxylic groups on the most discussed property of CDs, on the excitation wavelength-dependent emission.

The recent discovery of carbon dots has drawn enormous scientific attention. This material possess similar advantages to traditional semiconductor quantum dots (e.g. CdSe), they are resistant to photobleaching.[157] Moreover, they are

---

[A] Published as: **Hola, K.**; Bourlinos, A. B.; Kozak, O.; Berka, K.; Siskova, K. M.; Havrdova, M.; Tucek, J.; Safarova, K.; Otyepka, M.; Giannelis, E. P.; Zboril, R. *Carbon* **2014**, *70*, 279–286. **Appendix A.**

also highly biocompatible and non-toxic oppositely to quantum dots based on heavy metals.[158] The most discussed attribute of CDs is the origin of their photoluminescence. It is well accepted that their fluorescence is dependent on the excitation wavelength. Still, the origin of this feature is not clear. It can be caused by presence of CDs with different size and surface functionalities in the sample or it can be an intrinsic property of a single particle. The better understanding of this phenomenon can help to tune the desired fluorescent properties of CDs for their future applications.

Up to date, many synthetic pathways for the preparation of CDs have been reported as was shown in section 2.2. In this study, we developed a "molecular pathway" for the control of the size of CDs operated by the precursor. The CD size in the reported thermal decomposition was driven by the length of the alkyl chain of the gallic acid esters employed. The size of CDs derived from methyl gallate (MG27) was 3.5 nm, from propyl gallate (PG27) 3.2 nm and from lauryl gallate (LG27) 2 nm as shown in Figure 8. The observed trend can be explained by the steric hindrance of the alkyl chains that prevents them from entering the carbon source (benzene ring) to the center of CD formation. The largest hindrance of lauryl chains resulted in the formation of the smallest particles. Hence, according expectations the most dominant fluorescent emission of the prepared samples was consistent with the trend in the size. It is in agreement with the typical band-gap tuning by size of CD sp^2-domains.[159]

The obtained samples did not exhibit the typical excitation-dependent fluorescent emission (see Figure 9A). For this reason, the surface alkyl chains on CDs were converted to carboxylic surface groups by mild de-esterification (samples LG27O, PG270, MG27O). The aim was to see how the fluorescent can be influenced by the surface carboxylic groups. The most significant change was observed between the samples LG27 and LG27O (Figure 8F, 9 and 10). There was almost 40 nm red-shift of the emission maxima. This phenomenon was probably caused by surface carboxylic groups acting as charge carrier traps

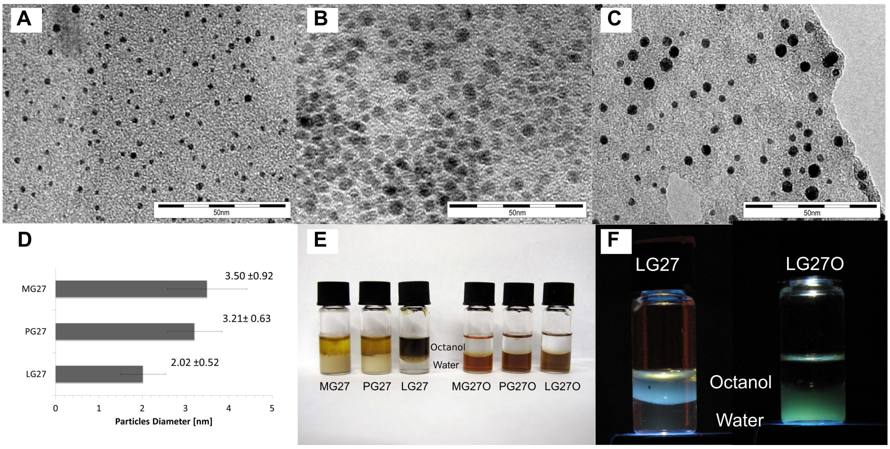

Figure 8. TEM images of CDs derived from lauryl gallate (A), propyl gallate (B) and methyl gallate (C), the scale bar is 50 nm; corresponding size distribution (D); octanol:water distribution of the CDs and their de-esterificated versions (E); the corresponding image of LG27 and its de-esterificated version in octanol:water under UV light.

prior to the radiative recombination. This type of emission is always red-shifted when compared to the intrinsic core emission (Figure 10).[160] Hence, the de-esterification also switches on the excitation wavelength-dependent emission (Figure 9B). This could be a consequence of density states broadening caused by the carboxylic groups or also by solvation. As a result, it is obvious that the excitation wavelength-dependent emission cannot be solely related to the presence of CDs with different sizes within one sample.

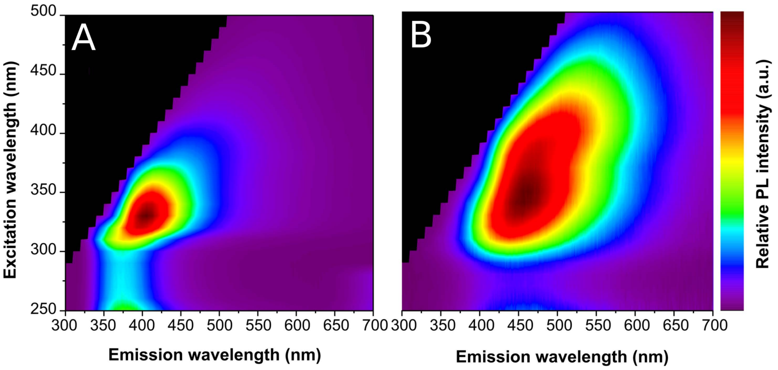

Figure 9. The excitation-emission photoluminescence map of CDs derived from lauryl gallate (A) and its de-esterificated version (B).

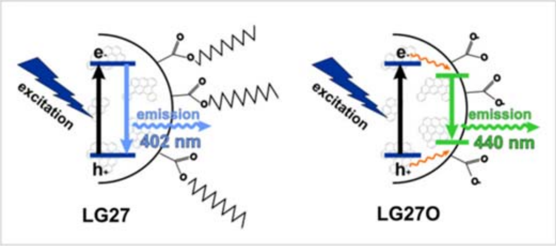

Figure 10. Schematic representation of the different emission from the samples LG27 and LG27O connected with 40 nm red-shift.

In conclusion, we developed a simple synthetic strategy to tune the size of CDs upon the choice of precursor. Analysis of the samples showed the role of the CD size in their fluorescence emission maxima. Similarly, it was clearly shown that the most discussed feature of CDs (excitation-dependent emission) can be caused by surface carboxylic groups.

5

Carbon dots – Emerging Light Emitters for Bioimaging, Cancer Therapy and Optoelectronics[B]

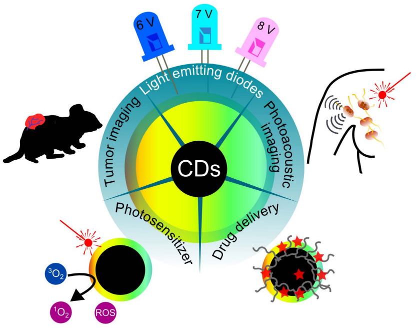

Carbon dots are promising materials for numerous applications. Thanks to their high biocompatibility they have been widely used in the biomedical field including cell labelling, *in vivo* optical and photoacoustic imaging and also in photothermal and photodynamic therapy. Moreover, they have been tested in the technical field as components of light emitting diodes (material for electroluminescence or for optical down-conversion). In this review, we summarized the main application potential of this unique material with focus to future utilization.

CDs are witnessing impressive growth since their first preparation. The main focus until now has been devoted to improve their light-emitting properties.[161] At the same time, the application portfolio of these materials has grown also enormously fast. This fact is caused by their favorable properties, like high resistance to photobleaching,[93] cheap and simple preparation, chemical inertness, and great water/solvent solubility.[68,69] Furthermore, CDs are highly biocompatible, thus overcoming the main drawback of the traditional semiconductor quantum dots.[162] Therefore, CDs have been tested in numerous applications in which they successfully replace their more toxic foregoers like CdSe or CdTe. The main drawback of CDs is low fluorescent efficiency,

---

[B] Published as: **Hola, K.**; Zhang, Y.; Wang, Y.; Giannelis, E. P.; Zboril, R.; Rogach, A. L. *Nano Today* **2014**, *9*, 590–603. **Appendix B.**

in particular in the red region of the spectrum. However, this was partly overcome by the appropriate synthetic strategies (see table 1 in appendix B). So far, the highest quantum yield (QY) for oil-soluble blue fluorescent CDs was 53%, and 94% for water-soluble ones.[108,163] CDs emitting in the red region of the spectrum were successfully prepared by Bhunia *et al*. (emission at 600 nm; QY 7%).[92] Still, the red emitting CDs are of a great importance for *in vivo* optical imaging, the red light has the best tissue penetration,[164] and are the last missing part in the quest for white LED.[165]

CDs have been many times used in cell labelling. In general, all of these *in vitro* studies show that CDs exhibit very low cytotoxicity (typically, the viability is over 50% even at concentration as high as 1 mg.ml^{-1}).[158,166,167] CDs enter the cells via an endosome-mediated pathway.[143,144] They can be also located in mitochondria or endoplasmic reticulum.[143] However, CDs with strong positive surface charge can also enter the cell nucleus as demonstrated in our recent studies.[80,145] Systematic safety evaluation of this material showed that CDs do not exhibit any acute or subacute toxicity and are safe for *in vivo* utilization.[168] Pegylated CDs exhibit a very favorable biodistribution in mice (see Figure 11). The particles can be very fast excreted from the body by renal clearance with almost no accumulation in the liver and spleen.[169] This property is very favorable in nanomedicine because the low accumulation of the nanoparticles in the body is connected with lower toxic risk.[170] Moreover, CDs with good renal clearance can be successfully accumulated in the tumor regions by passive targeting as demonstrated in study by Huang *et al*.[169] Both of these characteristics are typical for particles with size 4-8 nm and neutral surface charge.[170] These particles cannot be detected by plasma proteins and phagocytic cells and have therefore a convenient life-time in the blood for tumor accumulation. Still, they can be excreted from the body via glomerular filtration thanks to their size.[113] All these characteristics make CDs excellent candidates for biomedical applications.

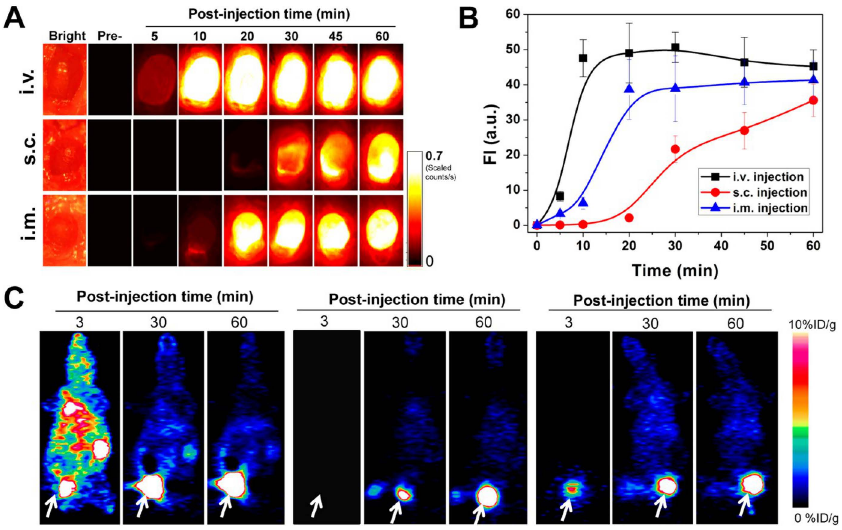

Figure 11. Renal excretion of pegylated CDs from mice injected in various ways (i.v. – intravenous; s.c. – subcutaneous; i.m. – intramuscular). Images of mice bladder at various times after CD injection obtained by optical imaging (A). Intensity of the signal from optical imaging as a function of time (B). The whole body biodistribution of CDs as function of time for i.v., s.c. and i.m. CD injection (C). Reprinted with permission from ref. 169. Copyright 2013 American Chemical Society.

CDs can be also utilized in more advantageous biomedical applications. For example, they have been successfully tested in photoacoustic imaging, a very useful technique for the localization of lymph vessels and axillary lymph nodes (typically used for determination of cancer cells spreading).[171] CDs have also been used for several types of therapeutic strategies e.g. as a nanocarrier for doxorubicin delivery,[172] as an agent active in photothermal therapy[173] and as an agent generating reactive oxygen species for cancer cells damage due to the oxidative stress (photodynamic therapy).[174,175] As the result, CDs can act as a flexible multi-theranostic agent combining therapy with diagnostics.

In the technical field, the most typical application of fluorescent materials is in the light emitting diodes (LED). The most relevant light emitting diodes (LED) including the inorganic quantum dots (QD) are typically based on cadmium or lead chalcogenides.[176,177] The main drawback for the commercialization of these efficient QD-LED is the expected environmental regulation of heavy metals. Therefore, there is an urgent search for metal-free LED and thanks to their non-toxicity, CDs have started to appear as a valuable alternative. The electroluminescence (EL) of CDs was tested for the first time in 2011 by Wang *et al.*[178] However, the quantum efficiency reported in that early example was only of 0.083%. Two years later, Zhang *et al.* reported multi-color EL from one type of CDs in which the color (blue, cyan, magenta and white, Figure 12) could be tuned by an applied electric potential. However, the quantum efficiency was still low.[165] Since that time, the proper ligands and conducting layers to CDs in LED are under intense investigation to harvest the physical potential of CDs.

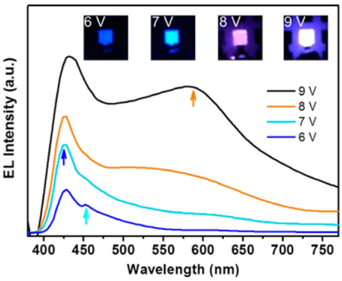

Figure 12. Multi-color LED based on CDs with color determined by applied the voltage. Reprinted with permission from ref. 165. Copyright 2013 of American Chemical Society.

In conclusion, CDs represent an attractive fluorescent alternative to the heavy metal-based quantum dots. Their biocompatibility and good photostability provide them a unique position in the biomedical field. So far, they have been successfully applied in optical or photoacoustic imaging and also in several therapeutic protocols. Still, their low quantum yield and missing red emission need to be dramatically improved to fulfil their promising position as a bio-alternative for the most common CdSe quantum dots. Improvement in these properties has to be based on better understanding of the physical mechanism of their fluorescence. It can dramatically increase their applicability in other fields and also to boost their light-harvesting efficiency in optoelectronic devices.

6

Graphitic Nitrogen Triggers Red Fluorescence in Carbon Dots[C]

The following pages (37 – 42) are available only in the printed version of the thesis. The discussed topic was under revision at the time of thesis submission.

The original text can be sent on the email request: katkahola@gmail.com;
or lately find under given title.

[C] Currently submitted to ACS Nano as: **Hola, K.**; Sudolska, M.; Kalytchuk, S.; Rogach, A. L.; Otyepka, M.; Zboril, R.; **Appendix C.** The text to this manuscript is given only in the printed version of the thesis.

7

Thiofluorographene-Hydrophilic Graphene Derivative with Semiconducting and Genosensing Properties[D]

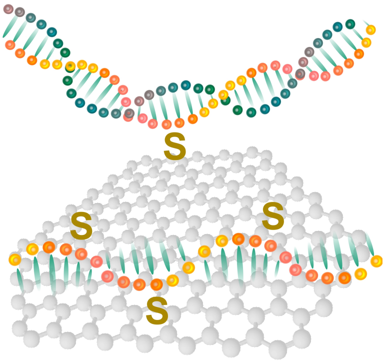

Covalent modification of graphene and graphene derivatives represents one of the most significant trends in current materials science. This type of modification can heavily influence the intrinsic properties of this unique material and also the surface properties for example enhancing the communication with the surrounding environment. In this study, we presented the first example of covalent chemistry on fluorographene (GF). We used nucleophilic substitution in a polar solvent to attach –SH groups to GF sheets. The prepared material can exhibit semiconducting properties with a bandgap in the range of 1–2 eV depending on the degree of substitution. Hence, the surface –SH groups increased the hydrophilicity of the system and were utilized in DNA sensing by electrochemical impedance spectroscopy.

The discovery of graphene in 2004 started a revolution in the world of nanomaterials. Its exceptional physical properties such as extremely large surface area, mechanical stability and exceptional electronic properties make graphene the most significant material in electrochemical sensing.[182] On the other hand, pristine graphene suffers from zero band-gap and bad water

---

[D] Published as: Urbanová, V.; **Holá, K.**; Bourlinos, A. B.; Čépe, K.; Ambrosi, A.; Loo, A. H.; Pumera, M.; Karlický, F.; Otyepka, M.; Zbořil, R. Adv. Mater. 2015, 27, 2305–2310. **Appendix D.**

dispersability. However, covalent functionalization can dramatically influence both of these properties. So far, the most common graphene derivatives are graphene oxide,[183] graphane[184] and fluorographene.[146,150] Fluorographene represents the thinnest insulator and is very well chemically defined in comparison to graphene oxide. The degree of fluorination of GF dramatically determines its electronic properties.[150] The C-F bond can be also utilized for covalent modification towards advantageous applications.

In this study, we prepared a new derivative of fluorographene by covalent functionalization. Thiofluorographene, G(SH)F, was obtained by exfoliation of fluorinated graphite in dimethylformamide followed by reaction with sodium hydrosulfide (see Figure 15). After purification, the prepared material was redispersed in water and further characterized. The composition of the sample was studied by XPS and revealed presence of carbon, fluorine, sulfur and oxygen. The atomic ratios were 11.8 for C/F, 16.4 for C/S and 11.8 for C/O. The surface sulfhydryl groups were also partly oxidized according high resolution S 2*p* XPS spectrum. The distribution of sulfur and fluorine on the sheets was very homogenous, as confirmed by HR-TEM in the mode of STEM-EDS mapping (see appendix D). The Raman spectrum showed the presence of typical D-band and G-band, indicating the partial defluorination of the fluorographene sheets during substitution and formation of aromatic rings. The typical band for C-S-H bonding in plane at 830 cm^{-1} was also detected, thus confirming successful covalent functionalization.[185]

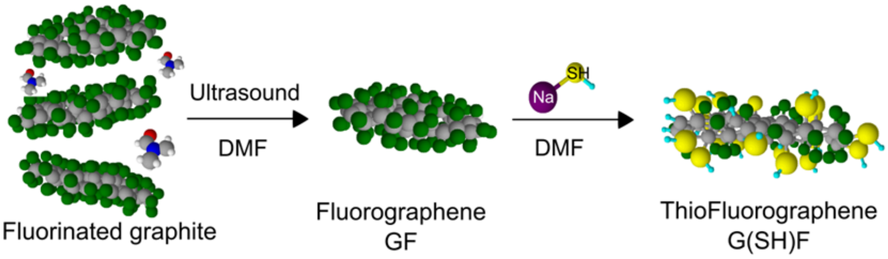

Figure 15. The reaction scheme for the preparation of thiofluorographene by exfoliation and nucleophilic substitution.

Density functional theory (DFT) calculations were performed to explain the partial defluorination of the prepared material during reaction and the presence of the fluorine atoms residues. The structural optimization showed that the sulfhydryl groups are spontaneously desorbed from pristine graphene and the presence of fluorine can stabilize them. The electronic properties of the newly prepared G(SH)F were also calculated taking in consideration the determined structural motive and experimental composition. The bandgaps spanned 1 to 2 eV (the typical range for semiconductors) depending on the arrangement of sulfhydryl and fluorine groups. The bandgap affects the absorption properties of this new material but it can also be an advantageous feature for potential electronic applications.

The G(SH)F was tested as a biosensor for impedimetric detection of DNA (as a genosensor). This technique is based on the measurement of the changes in charge transfer resistance. It reflects the conformation changes of the DNA on the surface of a chip. A DEP (disposable electrochemical printed) chip was modified by G(SH)F and single-stranded DNA (ssDNA) was immobilized on the surface. The charge resistance transfer was afterwards measured in presence of fully complementary ssDNA (wild-type), single-base mismatch ssDNA (mutant) and non-complementary ssDNA (see Figure 16). The same experiment was also performed on non-modified DEP chip and on a chip modified by fluorographene. From the comparison of the data obtained, it was apparent that the sulfhydryl groups were crucial in order to get reliable results. The sulfhydryl groups enhanced the impedimentric DNA sensing probably thanks to the better orientation of ssDNA and better accessibility to the complementary base.

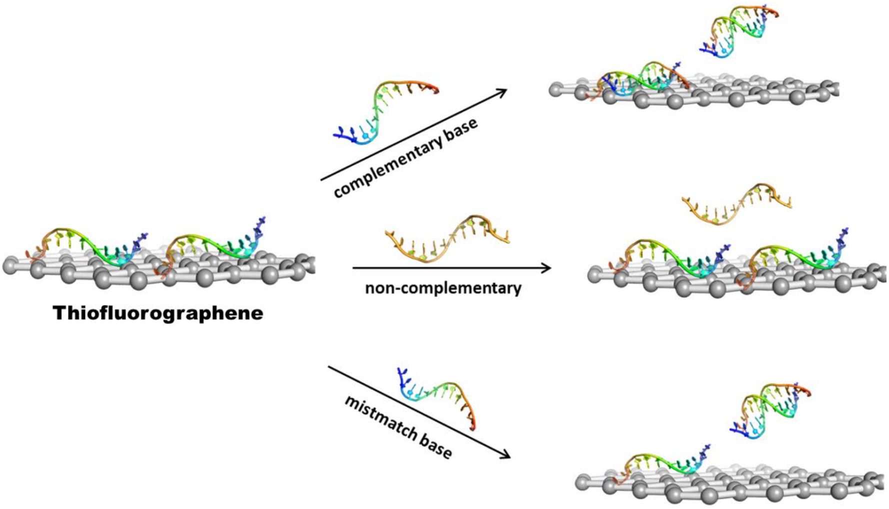

Figure 16. Schematic representation of the testing of G(SH)F as genosenosor in electrochemical impedance spectroscopy with principle of DNA sensing.

In summary, we prepared a new material by covalent functionalization of fluorographene. The C-F bonds of fluorographene were used for substitution reaction for the first time. The newly attached sulfhydryl groups were homogenously distributed all over the fluorographene sheet. This new derivative can be potentially used as a semiconductor but also as suitable material for genosensing applications. Moreover, the nucleophilic substitution protocol on fluorographene opens the doors for many other derivatives with advantageous properties as shown in the following section.

8

Room Temperature Organic Magnets Derived from sp^3 Functionalized Graphene[E]

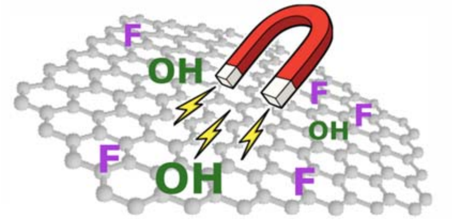

The preparation of organic magnets is an important challenge across various technological fields. The exclusive *s* and *p* orbitals in the graphene framework and its magnetic behavior represent a curious physical phenomenon that is not properly understood. This study reported the preparation of hydroxofluorographene showing room temperature antiferromagnetic ordering with transition to ferromagnetic regime at low temperatures. This behavior was never observed in 2D organic material. The consequent theoretical investigation shed a light on the origin of the room temperature magnetism: sp^2-conjugated diradical motif embedded in a sp^3 framework. Moreover, the material characterization (EPR and ICP-MS) confirmed that the magnetic behavior is not caused by metallic impurities.

Graphene and its honeycomb lattice have attracted enormous research interest thanks to its exceptional optical, electronic and transport properties.[39,186] This material offers the possibility to study a number of exceptional physical phenomena (e.g. nonlinear Kerr effect or Casimir effect).[40,187] Still, the preparation of graphene derivatives with room temperature magnetism represents an unaddressed challenge. There are several suggested strategies in order to imprint magnetic centers into graphitic structures: formation of defect

---

[E] Published as: Tuček, J.; **Holá, K.**; Bourlinos, A. B.; Błoński, P.; Bakandritsos, A.; Ugolotti, J.; Dubecký, M.; Karlický, F.; Ranc, V.; Čépe, K.; Otyepka, M.; Zbořil, R. *Nat. Commun.* **2017**, 8, 14525. **Appendix E.**

and vacancies,[188] formation of edge with specific geometry,[189] incorporation of different atoms as nitrogen, sulfur or others.[52,53] It must be noted that Nair *et al*. reported that imprinting of paramagnetic centers into graphene can be achieved by partial fluorination (incorporation of *sp*^{3} centers).[156] In this study, we used our previous strategy for nucleophilic substitution of fluorine atoms by hydroxyl groups in fluorographene (see section 7). The resulting hydroxofluorographene (G(OH)F) with newly formed *sp*^{2} domains and hydroxofluoro *sp*^{3} regions exhibited room temperature antiferromagnetism. The presented findings were supported by a theoretical model.

The G(OH)F was prepared by exfoliation of fully fluorinated graphite in dimethylformamide followed by reaction with tetramethylammonium hydroxide. After purification, the material obtained was redispersed in water and characterized. The analysis revealed the presence of *sp*^{2} domains ($I_G/I_D = 1.1$ according to Raman spectroscopy) with total composition of $C_{18}(OH)_{1.8}F_{7.2}$ according to XPS analysis. The high resolution C 1s spectrum also revealed that the oxygen is present only in the form of hydroxyl groups. This was confirmed by thermogravimetric analysis combined with mass detection of released gasses (no carbon monoxide or dioxide was released during the analysis). Moreover, the HR-TEM images combined with STEM-EDS mapping showed a homogenous distribution of oxygen and fluorine atoms across the whole hydroxofluorographene sheets (Figure 17).

Magnetic properties of G(OH)F were characterized by measuring the temperature evolution of the mass magnetic susceptibility (χ_{mass}) under external magnetic field (10 kOe). The temperature dependence was not described by Curie-Weiss law from 5 to 300 K (see Appendix E). There was a significant decrease in magnetic susceptibility with lowering of the temperature. At room temperature the sample exhibited antiferromagnetic ordering, a property never observed in any 2D “organic” material so far.

Upon the decrease in temperature a transition to a ferromagnetic state at 62 K was observed. This can be explained as the ground state of G(OH)F while the antiferromagnetic state is the thermally excited state. These antiferromagnetic/ferromagnetic transitions are typical for molecular radical-based systems.[190] The magnetization at 5 K saturated above a value of 1 emu.g^{-1} making G(OH)F one of the strongest magnetic graphene-based systems. It must be stressed that, this magnetization was not induced by any metallic impurities, as verified by ICP-MS. EPR had the *g* factor of around 2, a value typical for organic magnets.

A DFT theoretical screening of models of general composition of $C_{18}(OH)_yF_x$ (x, y = 0-8) was conducted to assess the role of fluorine and hydroxyl groups on the magnetic behavior of the system and the nature of the imprinted magnetic motif. The magnetic properties as a function of the stoichiometry determined by DFT are given in Figure 18. The theoretical model suggested that the magnetism originated from stable biradical motifs on sp^2-conjugated islands (typically m-xylene motif) stabilized by a surrounding sp^3-matrix.

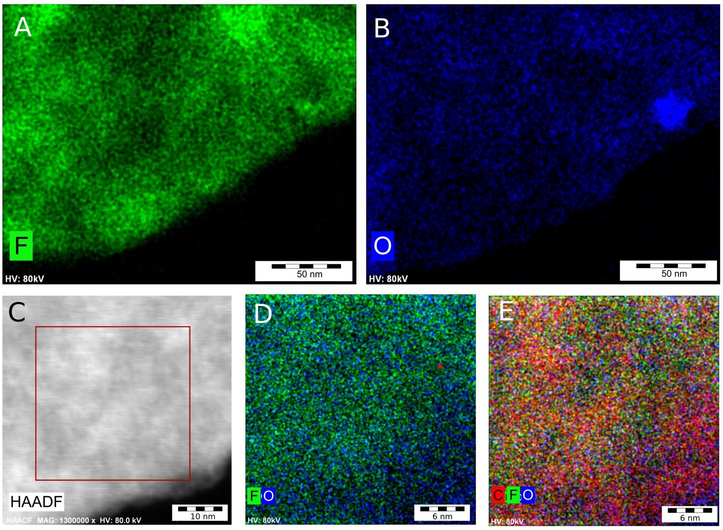

Figure 17. HR-TEM images in the mode of STEM-EDS mapping of hydroxofluorographene (green – fluorine, blue – oxygen, red – carbon).

The diradical motif was also confirmed by EPR characterization. Also, the role of hydroxyl group was revealed by DFT. The hydroxyl group located between the biradical motifs stabilized the ferromagnetic regime through coupling. This was confirmed by calculations performed on other configurations. If the magnetic motif was embed by a fully fluorinated *sp*^{3}-network the system was paramagnetic. An increasing amount of hydroxyl groups around this magnetic motif caused stabilization of magnetism and also restriction of "travelling" of fluorine to non-magnetic ordering by orbitals overlap.

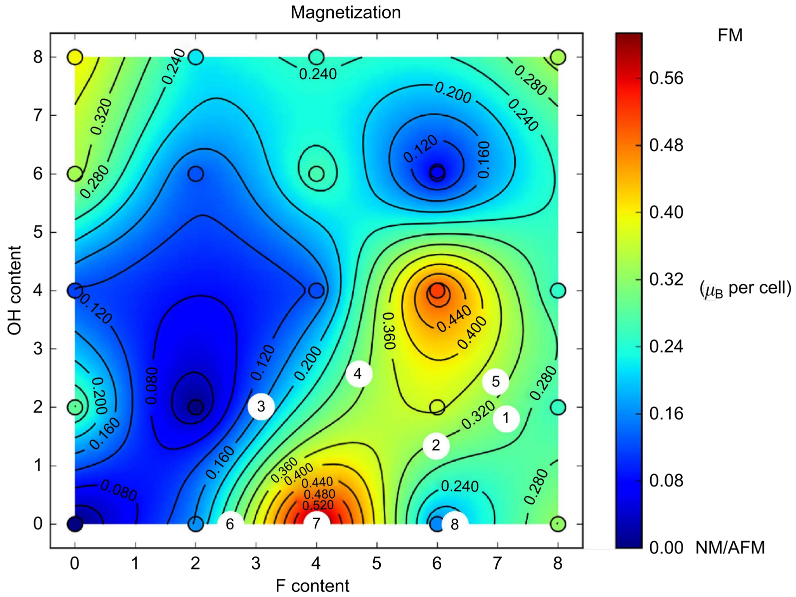

Figure 18. The magnetic properties of hydroxofluorographene across the stoichiometry $C_{18}(OH)_yF_x$ (x, y = 0-8) determined by DFT. The sample described in details in the main text is denoted as 1. Still, the other prepared samples 2-8 experimentally agreed with the given mean magnetization map.

In conclusion, we prepared the first graphene-based room temperature antiferromagnet, hydroxofluorographene. The hydroxyl groups were incorporated into the *sp*^{3}-matrix of fluorographene by nucleophilic substitution. The magnetic motif and the impact of hydroxyl and fluorine on the magnetic behavior of material were explained by DFT calculations in detail. We believe that this discovery can open the door for a wider family of 2D-magnets.

Summary

The previous pages and chapters are bringing a very short “microview” on the carbon nanoworld. This thesis is focused mainly on carbon dots and their photoluminiscence and on new derivatives of fluorographene with extraordinary properties. In particular, the given results are interpreted from the perspective of the functional groups embedded in the graphene lattice of the prepared materials. It is also given in the relevance with the other members of carbon nanofamily as fullerenes, carbon nanotubes, graphene and nanodiamonds. Their functional groups also determine their physicochemical properties and applications.

In the field of carbon dots, there was described how their surface **carboxyl groups** can red-shift their fluorescence emission (from blue to green). Consequently, these groups also induced excitation-dependent emission in the material. The **graphitic nitrogen** in carbon dots was also shown to be relevant to red-shift in carbon dots. In particular, this functionality was able to shift the CD emission above 600 nm. In the field of fluorographene, there were discussed mainly the **hydroxyl and sulfhydryl groups** newly introduced into the fluorographene lattice. It was shown that sulfhydryl groups can be very useful for interaction with DNA and genosening by impedance spectroscopy. More importantly, the hydroxyl and fluorine groups in graphene showed ability to sustain the radical motive in the newly prepared hydroxofluorographene. In general, the insight into the behavior of carbon nanomaterials provided here showed the importance of their functional groups.

Shrnutí

Předešlé stránky odhalují malý kousek uhlíkového nanosvěta. Tato práce se zabývá především uhlíkovými tečkami a jejich fotoluminiscencí, zároveň také fluorografenem a jeho nově odhalenými vlastnostmi. Dosažené výsledky jsou podávány z hlediska funkčních skupin kovalentně vázaných ke grafenové matrici. Ostatní uhlíkové materiály jako fullereny, uhlíkové nanotrubičky, grafen či nanodiamanty jsou také krátce zmíněny z hlediska významu jejich funkčních skupin.

U uhlíkových teček byla vysvětlena spojitost mezi povrchovými **karboxylovými skupinami** a posunutím jejich fluorescence z modré do zelené oblasti. Bylo také prokázáno, že tyto skupiny zapříčiňují i typickou vlastnost uhlíkových teček a to barvu emise závislou na excitační vlnové délce. Další studie uhlíkových teček ukázala, že posun emise může být způsoben i **grafitickým dusíkem**, ten je však schopen emisi posunout až do červené oblasti. Jako další byly diskutovány **hydroxylové a sulfhydrylové funkční skupiny**. V tomto případě se však jednalo o skupiny přichycené ke fluorografenu. Sulfhydrylové skupiny na fluorografenu byly využity pro detekci DNA pomocí impedanční spektroskopie. Hydroxylové skupiny byly pak důvodem vzniku pokojového magnetismu v nově připraveném hydroxofluorografenu. Ve stručnosti, funkční skupiny ve velké míře ovlivňují fyzikálně-chemické vlastnosti uhlíkových materiálů, a tím i zvyšují šance na jejich uplatnění.

List of Publications

---

(1) Bourlinos, A. B.; Bakandritsos, A.; Kouloumpis, A.; Gournis, D.; Krysmann, M.; Giannelis, E. P.; Polakova, K.; Safarova, K.; **Hola, K.**; Zboril, R. Gd(iii)-Doped Carbon Dots as a Dual Fluorescent-MRI Probe. *J. Mater. Chem.* **2012**, *22*, 23327–23330.

(2) Bourlinos, A. B.; Karakassides, M. a.; Kouloumpis, A.; Gournis, D.; Bakandritsos, A.; Papagiannouli, I.; Aloukos, P.; Couris, S.; **Hola, K.**; Zboril, R.; *et al.* Synthesis, Characterization and Non-Linear Optical Response of Organophilic Carbon Dots. *Carbon* **2013**, *61*, 640–649.

(3) **Hola, K.**; Bourlinos, A. B.; Kozak, O.; Berka, K.; Siskova, K. M.; Havrdova, M.; Tucek, J.; Safarova, K.; Otyepka, M.; Giannelis, E. P.; *et al.* Photoluminescence Effects of Graphitic Core Size and Surface Functional Groups in Carbon Dots: COO− Induced Red-Shift Emission. *Carbon* **2014**, *70*, 279–286. **Appendix A.**

(4) **Hola, K.**; Zhang, Y.; Wang, Y.; Giannelis, E. P.; Zboril, R.; Rogach, A. L. Carbon dots—Emerging Light Emitters for Bioimaging, Cancer Therapy and Optoelectronics. *Nano Today* **2014**, *9*, 590–603. **Appendix B.**

(5) Datta, K. K. R.; Kozak, O.; Ranc, V.; Havrdova, M.; Bourlinos, A. B.; Safarova, K.; **Hola, K.**; Tomankova, K.; Zoppellaro, G.; Otyepka, M.; *et al.* Quaternized Carbon Dots Modified Graphene Oxide for Selective Cell Labelling – Controlled Nucleus and Cytoplasm Imaging. *Chem. Commun.* **2014**, *50*, 10782–10785.

(6) Magro, M.; Campos, R.; Baratella, D.; Lima, G.; **Holà, K.**; Divoky, C.; Stollberger, R.; Malina, O.; Aparicio, C.; Zoppellaro, G.; *et al.* A Magnetically Drivable Nanovehicle for Curcumin with Antioxidant Capacity and MRI Relaxation Properties. *Chem. A Eur. J.* **2014**, *20*, 11913–11920.

(7) Bourlinos, A. B.; Trivizas, G.; Karakassides, M. A.; Baikousi, M.; Kouloumpis, A.; Gournis, D.; Bakandritsos, A.; **Hola, K.**; Kozak, O.; Zboril, R.; *et al.* Green and Simple Route toward Boron Doped Carbon Dots with Significantly Enhanced Non-Linear Optical Properties. *Carbon* **2015**, *83*, 173–179.

(8) **Hola, K.**; Markova, Z.; Zoppellaro, G.; Tucek, J.; Zboril, R. Tailored Functionalization of Iron Oxide Nanoparticles for MRI, Drug Delivery, Magnetic Separation and Immobilization of Biosubstances. *Biotechnol. Adv.* **2015**, *33*, 1162–1176.

(9) Lim, C. S.; **Hola, K.**; Ambrosi, A.; Zboril, R.; Pumera, M. Graphene and Carbon Quantum Dots Electrochemistry. *Electrochem. Commun.* **2015**, *52*, 75–70.

(10) Urbanová, V.; **Holá, K.**; Bourlinos, A. B.; Čépe, K.; Ambrosi, A.; Loo, A. H.; Pumera, M.; Karlický, F.; Otyepka, M.; Zbořil, R. Thiofluorographene-Hydrophilic Graphene Derivative with Semiconducting and Genosensing Properties. *Adv. Mater.* **2015**, *27*, 2305–2310. **Appendix D**

(11) Lazar, P.; Chua, C. K.; **Holá, K.**; Zbořil, R.; Otyepka, M.; Pumera, M. Dichlorocarbene-Functionalized Fluorographene: Synthesis and Reaction Mechanism. *Small* **2015**, *11*, 3790–3796.

(12) Havrdova, M.; **Hola, K.**; Skopalik, J.; Tomankova, K.; Petr, M.; Cepe, K.; Polakova, K.; Tucek, J.; Bourlinos, A. B.; Zboril, R. Toxicity of Carbon Dots – Effect of Surface Functionalization on the Cell Viability, Reactive Oxygen Species Generation and Cell Cycle. *Carbon* **2016**, *99*, 238–248.

(13) Ulbrich, K.; **Holá, K.**; Šubr, V.; Bakandritsos, A.; Tuček, J.; Zbořil, R. Targeted Drug Delivery with Polymers and Magnetic Nanoparticles: Covalent and Noncovalent Approaches, Release Control, and Clinical Studies. *Chem. Rev.* **2016**, *116*, 5338–5431.

(14) Tuček, J.; Sofer, Z.; Bouša, D.; Pumera, M.; **Holá, K**.; Malá, A.; Poláková, K.; Havrdová, M.; Čépe, K.; Tomanec, O.; *et al.* Air-Stable Superparamagnetic Metal Nanoparticles Entrapped in Graphene Oxide Matrix. *Nat. Commun.* **2016**, *7*, 12879.

(15) Tuček, J.; **Holá, K.**; Bourlinos, A. B.; Błoński, P.; Bakandritsos, A.; Ugolotti, J.; Dubecký, M.; Karlický, F.; Ranc, V.; Čépe, K.; *et al.* Room Temperature Organic Magnets Derived from sp3 Functionalized Graphene. *Nat. Commun.* **2017**, *8*, 14525. **Appendix E.**

(16) **Hola, K.;** Sudolska, M.; Kalytchuk, S.; Rogach, A. L.; Otyepka, M.; Zboril, R.; Graphitic Nitrogen Triggers Red Fluorescence in Carbon Dots. *Currently submitted*. **Nonpublic Appendix C.**

(17) Bourlinos, A. B.; Rathi, A.K.; Gawande, M.B.; **Hola, K.**; Kalytchuk, S.; Karakassides, M. A.; Kouloupis, A.; Gournis, D.; Deligiannakis, Y.; Gianellis, E.P.; Zboril, R. Fe(III)-Functionalized Carbon Dots – Bottom-up Synthesis and Advanced Catalytic Applications. *Appl. Matter. Today* **2017**, *7*, 179-184.

List of Abbreviations

0D	Zero-dimensional
1D	One-dimensional
2D	Two-dimensional
AFM	Atomic force microscopy
Asp	Aspartic acid
bCDs	Carbon dots with blue luminescence
CA	Citric acid
CDs	Carbon dots
DEP	Disposable electrochemical printed chip
DFT	Density functional theory
DMF	Dimethylformamide
DMSO	Dimethylsulfoxide
EL	Electroluminescence
EPR	Electron paramagnetic resonance
G(OH)F	Hyroxofluorographene
G(SH)F	Thiofluorographene
gCDs	Carbon dots with green luminescence
GF	Fluorographene
GO	Graphene oxide
HOMO	Highest occupied molecular orbital
HOPG	Highly oriented pyrolytic graphite
HR-TEM	High resolution transmission microscopy
i.m.	Intramuscular application
i.v.	Intravenous application

ICP-MS	Inductively coupled plasma mass spectrometry
LED	Light emitting diodes
LG27	Carbon dots prepared from lauryl gallate
LF27O	Carbon dots prepared from lauryl gallate after de-esterification
LUMO	Lowest unoccupied molecular orbital
MG27	Carbon dots prepared from methyl gallate
MG27O	Carbon dots prepared from methyl gallate after de-esterification
MRI	Magnetic resonance imaging
NMP	N-methylpyrrolidone
n.r.	Not reported
PEG	Polyethylene glycol
PEG-NH2	Polyethylene glycol with terminal amino group
PEI PEG	Polyethyleneimine
PG27	Carbon dots prepared from propyl gallate
PG27O	Carbon dots prepared from propyl gallate after de-esterification
Ppm	Part(s) per million
QY	Quantum yield
QY-LED	Light emitting diodes base on quantum dots
rCDs	Carbon dots with red luminescence
s.c.	Subcutaneous application
ssDNA	Single stranded DNA
STEM-EDS	Scanning transmission electron microscopy combined with energy-dispersive X-ray spectroscopy
TEM	Transmission electron microscopy
XPS	X-Ray photoelectron spectroscopy
yCDs	Carbon dots with yellow luminescence

References

(1) Baptista, F. R.; Belhout, S. a.; Giordani, S.; Quinn, S. J. Recent Developments in Carbon Nanomaterial Sensors. *Chem. Soc. Rev.* **2015**, *44*, 4433–4453.

(2) Jariwala, D.; Sangwan, V. K.; Lauhon, L. J.; Marks, T. J.; Hersam, M. C. Carbon Nanomaterials for Electronics, Optoelectronics, Photovoltaics, and Sensing. *Chem. Soc. Rev.* **2013**, *42*, 2824–2860.

(3) Mauter, M. S.; Elimelech, M. Environmental Applications of Carbon-Based Nanomaterials. *Environ. Sci. Technol.* **2008**, *42*, 5843–5859.

(4) Iijima, S. Direct Observation of the Tetrahedral Bonding in Graphitized Carbon Black by High Resolution Electron Microscopy. *J. Cryst. Growth* **1980**, *50*, 675–683.

(5) Kroto, H. W.; Heath, J. R.; O'Brien, S. C.; Curl, R. F.; Smalley, R. E. C60: Buckminsterfullerene. *Nature* **1985**, *318*, 162–163.

(6) Georgakilas, V.; Perman, J. A.; Tucek, J.; Zboril, R. Broad Family of Carbon Nanoallotropes: Classification, Chemistry, and Applications of Fullerenes, Carbon Dots, Nanotubes, Graphene, Nanodiamonds, and Combined Superstructures. *Chem. Rev.* **2015**, *115*, 4744–4822.

(7) Goldshleger, N. F. Fullerenes and Fullerene-Based Materials in Catalysis. *Fuller. Sci. Technol.* **2001**, *9*, 255–280.

(8) Li, G.; Shrotriya, V.; Huang, J.; Yao, Y.; Moriarty, T.; Emery, K.; Yang, Y. High-Efficiency Solution Processable Polymer Photovoltaic Cells by Self-Organization of Polymer Blends. *Nat. Mater.* **2005**, *4*, 864–868.

(9) Markovic, Z.; Trajkovic, V. Biomedical Potential of the Reactive Oxygen Species Generation and Quenching by Fullerenes (C60). *Biomaterials* **2008**, *29*, 3561–3573.

(10) http://www.nanotechproject.org/cpi/products/zelens-r-fullerene-c-60-night-cream/ Accessed: 2017-01-24.

(11) Benn, T. M.; Westerhoff, P.; Herckes, P. Detection of Fullerenes (C60 and C70) in Commercial Cosmetics. *Enivron. Pollut.* **2011**, *159*, 1334–1342.

(12) Djordjević, A.; Bogdanović, G.; Dobrić, S. Fullerenes in Biomedicine. *J. B.U.ON.* **2006**, *11*, 391–404.

(13) Schinazi, R. F.; Sijbesma, R.; Srdanov, G.; Hill, C. L.; Wudl, F. Synthesis and Virucidal Activity of a Water-Soluble, Configurationally Stable, Derivatized C60 Fullerene. *Antimicrob. Agents Chemother.* **1993**, *37*, 1707–1710.

(14) Tsao, N.; Luh, T. Y.; Chou, C. K.; Wu, J. J.; Lin, Y. S.; Lei, H. Y. Inhibition of Group A Streptococcus Infection by Carboxyfullerene. *Antimicrob. Agents Chemother.* **2001**, *45*, 1788–1793.

(15) Tsao, N.; Kanakamma, P. P.; Luh, T. Y.; Chou, C. K.; Lei, H. Y. Inhibition of Escherichia Coli-Induced Meningitis by Carboxyfullerence. *Antimicrob. Agents Chemother.* **1999**, *43*, 2273–2277.

(16) Xie, L.; Luo, Y.; Lin, D.; Xi, W.; Yang, X.; Wei, G. The Molecular Mechanism of Fullerene-Inhibited Aggregation of Alzheimer's Β-Amyloid Peptide Fragment. *Nanoscale* **2014**, *6*, 9752–9762.

(17) Trajkovic, S.; Dobric, S.; Djordjevic, a; Dragojevic-Simic, V.; Milovanovic, Z. Radioprotective Efficiency of Fullerenol in Irradiated Mice. *Curr. Res. Adv. Mater. Process.* **2005**, *494*, 549–554.

(18) Hirsch, A. The Era of Carbon Allotropes. *Nat. Mater.* **2010**, *9*, 868.

(19) Stevenson, S.; Rice, G.; Glass, T.; Harich, K.; Cromer, F.; Jordan, M. R.; Craft, J.; Dorn, H. C. Metallofullerenes in High Yield and Purity. *Nature* **1999**, *80*, 80–82.

(20) Tyryshkin, S. C Benjamin, A. Ardavan, G Andrew, D Briggs, D. A Britz, D. Gunlycke, J. Jefferson, M. Jones, D. F. Leigh, B. W. Lovett, A. N. Khlobystov, S A Lyon, J. Morton and K. Porfyrakis, M. R. S. and a. M. T. Towards a Fullerene-Based Quantum Computer. *J. Phys. Condens. Matter* **2006**, *18*, 867–868.

(21) Sitharaman, B.; Bolskar, R. D.; Rusakova, I.; Wilson, L. J. Gd@C60[C(COOH)2]10 and Gd@C60(OH)x : Nanoscale Aggregation Studies of Two Metallofullerene MRI Contrast Agents in Aqueous Solution. *Nano Lett.* **2004**, *4*, 2373–2378.

(22) Boltalina, O. V.; Popov, A. a.; Kuvychko, I. V.; Shustova, N. B.; Strauss, S. H. Perfluoroalkylfullerenes. *Chem. Rev.* **2015**, *115*, 1051–1105.

(23) Lebedeva, M. a.; Chamberlain, T. W.; Khlobystov, A. N. Harnessing the Synergistic and Complementary Properties of Fullerene and Transition-Metal Compounds for Nanomaterial Applications. *Chem. Rev.* **2015**, *115*, 11301–11351.

(24) Iijima, S. Helical Microtubules of Graphitic Carbon. *Nature* **1991**, *350*, 627–628.

(25) Kratschmer, W.; Lamb, L. D.; Fostiropoulos, K.; Huffman, D. R. Solid C60: A New Form of Carbon. *Nature* **1990**, *374*, 354–358.

(26) Ding, F.; Jiao, K.; Lin, Y.; Yakobson, B. I. How Evaporating Carbon Nanotubes Retain Their Perfection? *Nano Lett.* **2007**, *7*, 681–684.

(27) Huang, J. Y.; Chen, S.; Wang, Z. Q.; Kempa, K.; Wang, Y. M.; Jo, S. H.; Chen, G.; Dresselhaus, M. S.; Ren, Z. F. Superplastic Carbon Nanotubes. *Nature* **2006**, *439*, 281.

(28) Baughman, R.; Zakhidov, A.; Heer, W. De. Carbon NanotubesOThe Route Toward Applications. *Science* **2002**, *297*, 787–792.

(29) De Volder,Michael F. L. Sameh H. Tawfick, R. H. B. and; Hart, a. J.; De Volder, M. F. L.; Tawfick, S. H.; Baughman, R. H.; Hart, a. J. Carbon Nanotubes : Present and Future Commercial Applications. *Science* **2013**, *339*, 535–539.

(30) Peng, H.; Alemany, L. B.; Margrave, J. L.; Khabashesku, V. N. Sidewall Carboxylic Acid Functionalization of Single-Walled Carbon Nanotubes. *J. Am. Chem. Soc.* **2003**, *125*, 15174–15182.

(31) Panchakarla, L. S.; Govindaraj, a.; Rao, C. N. R. Boron- and Nitrogen-Doped Carbon Nanotubes and Graphene. *Inorganica Chim. Acta* **2010**, *363*, 4163–4174.

(32) Shin, W. H.; Jeong, H. M.; Kim, B. G.; Kang, J. K.; Choi, J. W. Nitrogen-Doped Multiwall Carbon Nanotubes for Lithium Storage with Extremely High Capacity. *Nano Lett.* **2012**, *12*, 2283–2288.

(33) Nxumalo, E. N.; Coville, N. J. Nitrogen Doped Carbon Nanotubes from Organometallic Compounds: A Review. *Materials (Basel).* **2010**, *3*, 2141–2171.

(34) Yang, Q. H.; Hou, P. X.; Unno, M.; Yamauchi, S.; Saito, R.; Kyotani, T. Dual Raman Features of Double Coaxial Carbon Nanotubes with N-Doped and B-Doped Multiwalls. *Nano Lett.* **2005**, *5*, 2465–2469.

(35) Chen, P.; Wu, X.; Lin, J.; Tan, K. L. High H2 Uptake by Alkali-Doped Carbon Nanotubes Under Ambient Pressure and Moderate Temperatures. *Science* **1999**, *285*, 91–93.

(36) Land, T. a.; Michely, T.; Behm, R. J.; Hemminger, J. C.; Comsa, G. STM Investigation of Single Layer Graphite Structures Produced on Pt(111) by Hydrocarbon Decomposition. *Surf. Sci.* **1992**, *264*, 261–270.

(37) Affoune, A. M.; Prasad, B. L. V; Sato, H.; Enoki, T.; Kaburagi, Y.; Hishiyama, Y. Experimental Evidence of a Single Nano-Graphene. *Chem. Phys. Lett.* **2001**, *348*, 17–20.

(38) Novoselov, K. S.; Geim, a. K.; Morozov, S. V.; Jiang, D.; Zhang, Y.; Dubonos, S. V.; Grigorieva, I. V.; Firsov, a. a. Electric Field Effect in Atomically Thin Carbon Films. *Science* **2004**, *306*, 666–669.

(39) Balandin, A. a.; Ghosh, S.; Bao, W.; Calizo, I.; Teweldebrhan, D.; Miao, F.; Lau, C. N. Superior Thermal Conductivity of Single-Layer Graphene. *Nano Lett.* **2008**, *8*, 902–907.

(40) Tse, W. K.; MacDonald, a. H. Giant Magneto-Optical Kerr Effect and Universal Faraday Effect in Thin-Film Topological Insulators. *Phys. Rev. Lett.* **2010**, *105*, 1–5.

(41) Dreyer, D. R.; Park, S.; Bielawski, C. W.; Ruoff, R. S. The Chemistry of Graphene Oxide. *Chem. Soc. Rev.* **2015**, *39*, 228–240.

(42) Becerril, H. a H. a.; Mao, J.; Liu, Z.; Stoltenberg, R. M.; Bao, Z.; Chen, Y. Evaluation of Solution-Processed Reduced Graphene Oxide Films as Transparent Conductors. *ACS Nano* **2008**, *2*, 463–470.

(43) Elias, D. C.; Nair, R. R.; Mohiuddin, T. M. G.; Morozov, S. V.; Blake, P.; Halsall, M. P.; Ferrari, A. C.; Boukhvalov, D. W.; Katsnelson, M. I.; Geim, A. K.; *et al.* Control of Graphene´s Properties by Reversible Hydrogenation: Evidence for Graphane. *Science* **2009**, *323*, 610–613.

(44) Georgakilas, V.; Otyepka, M.; Bourlinos, A. B.; Chandra, V.; Kim, N.; Kemp, K. C.; Hobza, P.; Zboril, R.; Kim, K. S. Functionalization of Graphene: Covalent and Non-Covalent Approaches, Derivatives and Applications. *Chem. Rev.* **2012**, *112*, 6156–6214.

(45) Wang, X.; Sun, G.; Routh, P.; Kim, D. H.; Huang, W.; Chen, P. Heteroatom-Doped Graphene Materials: Syntheses, Properties and Applications. *Chem Soc Rev* **2014**, *43*, 7067–7098.

(46) Pumera, M. Heteroatom Modified Graphenes: Electronic and Electrochemical Applications. *J. Mater. Chem. C* **2014**, *2*, 6454–6461.

(47) David, L.; Singh, G. Reduced Graphene Oxide Paper Electrode: Opposing Effect of Thermal Annealing on Li and Na Cyclability. *J. Phys. Chem. C* **2014**, *118*, 28401–28408.

(48) Parades, J. I.; Villar-Rodil, S.; Martínez-Alonso, a.; Tascón, J. M. D. Graphene Oxide Dispersions in Organic Solvents. *Langmuir* **2008**, *24*, 10560–10564.

(49) Chung, C.; Kim, Y. K.; Shin, D.; Ryoo, S. R.; Hong, B. H.; Min, D. H. Biomedical Applications of Graphene and Graphene Oxide. *Acc. Chem. Res.* **2013**, *46*, 2211–2224.

(50) Sahin, H.; Leenaerts, O.; Singh, S. K.; Peeters, F. M. GraphAne: From Synthesis to Applications. *Wiley Interdiscip. Rev. Comput. Mol. Sci.* **2015**, *5*, 255–272.

(51) Eng, A. Y. S.; Poh, H. L.; Šaněk, F.; Maryško, M.; Matějková, S.; Sofer, Z.; Pumera, M. Searching for Magnetism in Hydrogenated Graphene: Using Highly Hydrogenated Graphene Prepared via Birch Reduction of Graphite Oxides. *ACS Nano* **2013**, *7*, 5930–5939.

(52) Błoński, P.; Tuček, J.; Sofer, Z.; Mazánek, V.; Petr, M.; Pumera, M.; Otyepka, M.; Zbořil, R. Doping with Graphitic Nitrogen Triggers Ferromagnetism in Graphene. *J. Am. Chem. Soc.* **2017**, jacs.6b12934.

(53) Tucek, J.; Blonski, P.; Sofer, Z.; Simek, P.; Petr, M.; Pumera, M.; Otyepka, M.; Zboril, R. Sulfur Doping Induces Strong Ferromagnetic Ordering in Graphene: Effect of Concentration and Substitution Mechanism. *Adv. Mater.* **2016**, *28*, 5045–5053.

(54) Kozak, O.; Sudolská, M.; Pramanik, G.; Cigler, P.; Otyepka, M.; Zbořil, R. Photoluminescent Carbon Nanostructures. *Chem. Mater.* **2016**, *28*, 4085–4128.

(55) Greiner, N. R.; Phillips, D. S.; Johnson, J. D.; Volk, F. Diamonds in Detonation Soot. *Nature* **1988**, *333*, 440–442.

(56) Volkov, K. V.; Danilenko, V. V.; Elin, V. I. Synthesis of Diamond from the Carbon in the Detonation Products of Explosives. *Combust. Explos. Shock Waves* **1990**, *26*, 366–368.

(57) Danilenko, V. V. On the History of the Discovery of Nanodiamond Synthesis. *Phys. Solid State* **2004**, *46*, 595–599.

(58) Ozawa, M.; Inaguma, M.; Takahashi, M.; Kataoka, F.; Krüger, A.; Osawa, E. Preparation and Behavior of Brownish, Clear Nanodiamond Colloids. *Adv. Mater.* **2007**, *19*, 1201–1206.

(59) Chang, Y.-R.; Lee, H.-Y.; Chen, K.; Chang, C.-C.; Tsai, D.-S.; Fu, C.-C.; Lim, T.-S.; Tzeng, Y.-K.; Fang, C.-Y.; Han, C.-C.; *et al.* Mass Production and Dynamic Imaging of Fluorescent Nanodiamonds. *Nat. Nanotechnol.* **2008**, *3*, 284–288.

(60) Yu, S.; Kang, M.; Chang, H.; Chen, K.; Yu, Y. Bright Fluorescent Nanodiamonds : No Photobleaching and Low Cytotoxicity. *J. Am. Chem. Soc.* **2005**, *127*, 17604–17605.

(61) Kazi, S. A Review Article on Nanodiamonds Discussing Their Properties and Applications. *Int. J. Pharm. Sci. Invent.* **2014**, *3*, 40–45.

(62) Mochalin, V. N.; Shenderova, O.; Ho, D.; Gogotsi, Y. The Properties and Applications of Nanodiamonds. *Nat. Nanotechnol.* **2012**, *7*, 11–23.

(63) Havlik, J.; Petrakova, V.; Rehor, I.; Petrak, V.; Gulka, M.; Stursa, J.; Kucka, J.; Ralis, J.; Rendler, T.; Lee, S.-Y.; *et al.* Boosting Nanodiamond Fluorescence: Towards Development of Brighter Probes. *Nanoscale* **2013**, *5*, 3208–3211.

(64) Zhang, X. Q.; Lam, R.; Xu, X.; Chow, E. K.; Kim, H. J.; Ho, D. Multimodal Nanodiamond Drug Delivery Carriers for Selective Targeting, Imaging, and Enhanced Chemotherapeutic Efficacy. *Adv. Mater.* **2011**, *23*, 4770–4775.

(65) Ziem, F. C.; Götz, N. S.; Zappe, A.; Steinert, S.; Wrachtrup, J. Highly Sensitive Detection of Physiological Spins in a Microfluidic Device. *Nano Lett.* **2013**, *13*, 4093–4098.

(66) Petrakova, V.; Rehor, I.; Stursa, J.; Ledvina, M.; Nesladek, M.; Cigler, P. Charge-Sensitive Fluorescent Nanosensors Created from Nanodiamonds. *Nanoscale* **2015**, *7*, 12307–12311.

(67) Havlik, J.; Raabova, H.; Gulka, M.; Petrakova, V.; Krecmarova, M.; Masek, V.; Lousa, P.; Stursa, J.; Boyen, H. G.; Nesladek, M.; *et al.* Benchtop Fluorination of Fluorescent Nanodiamonds on a Preparative Scale: Toward Unusually Hydrophilic Bright Particles. *Adv. Funct. Mater.* **2016**, *26*, 4134–4142.

(68) X. Xu, R. Ray, Y. Gu, H.J. Ploehn, L. Gearheart, K. Raker, W. A. Scrivens. Electrophoretic Analysis and Purification of Fluorescent Single-Walled Carbon Nanotube Fragments. *J. Am. Chem. Soc.* **2004**, *126*, 12736–12737.

(69) Baker, S. N.; Baker, G. A. Luminescent Carbon Nanodots: Emergent Nanolights. *Angew. Chem. Int. Ed.* **2010**, *49*, 6726–6744.

(70) Kershaw, S. V; Susha, A. S.; Rogach, A. L. Narrow Bandgap Colloidal Metal Chalcogenide Quantum Dots: Synthetic Methods, Heterostructures, Assemblies, Electronic and Infrared Optical Properties. *Chem. Soc. REv.* **2013**, *42*, 3033–3087.

(71) Reckmeier, C. J.; Schneider, J.; Susha, a. S.; Rogach, a. L. Luminescent Colloidal Carbon Dots: Optical Properties and Effects of Doping. *Opt. Express* **2016**, *24*, A312.

(72) Sun, Y.-P.; Zhou, B.; Lin, Y.; Wang, W.; Fernando, K. A. S.; Pathak, P.; Meziani, M. J.; Harruff, B. a; Wang, X.; Wang, H.; *et al.* Quantum-Sized Carbon Dots for Bright and Colorful Photoluminescence. *J. Am. Chem. Soc.* **2006**, *128*, 7756–7757.

(73) Zhu, S.; Song, Y.; Zhao, X.; Shao, J.; Zhang, J.; Yang, B. The Photoluminescence Mechanism in Carbon Dots (graphene Quantum

Dots, Carbon Nanodots, and Polymer Dots): Current State and Future Perspective. *Nano Res.* **2015**, *8*, 355–381.

(74) Li, L.; Wu, G.; Yang, G.; Peng, J.; Zhao, J.; Zhu, J.-J. Focusing on Luminescent Graphene Quantum Dots: Current Status and Future Perspectives. *Nanoscale* **2013**, *5*, 4015–4039.

(75) Lu, J.; Yang, J.; Wang, J.; Lim, A.; Wang, S.; Loh, K. P. One-Pot Synthesis of Fluorescent Carbon Graphene by the Exfoliation of Graphite in Ionic Liquids. *ACS Nano* **2009**, *3*, 2367–2375.

(76) Liu, R.; Wu, D.; Feng, X.; Müllen, K. Bottom-Up Fabrication of Photoluminescent Graphene Quantum Dots with Uniform Morphology. *J. Am. Chem. Soc.* **2011**, *133*, 15221–15223.

(77) Shen, J.; Zhu, Y.; Yang, X.; Li, C. Graphene Quantum Dots: Emergent Nanolights for Bioimaging, Sensors, Catalysis and Photovoltaic Devices. *Chem. Commun.* **2012**, *48*, 3686–3699.

(78) Krysmann, M. J.; Kelarakis, A.; Dallas, P.; Giannelis, E. P. Formation Mechanism of Carbogenic Nanoparticles with Dual Photoluminescence Emission. *J. Am. Chem. Soc.* **2012**, *134*, 747–750.

(79) Schneider, J.; Reckmeier, C. J.; Xiong, Y.; von Seckendorff, M.; Susha, A. S.; Kasák, P.; Rogach, A. L. Molecular Fluorescence in Citric Acid-Based Carbon Dots. *J. Phys. Chem. C* **2017**, *121*, 2014–2022.

(80) Havrdova, M.; Hola, K.; Skopalik, J.; Tomankova, K.; Petr, M.; Cepe, K.; Polakova, K.; Tucek, J.; Bourlinos, A. B.; Zboril, R. Toxicity of Carbon Dots – Effect of Surface Functionalization on the Cell Viability, Reactive Oxygen Species Generation and Cell Cycle. *Carbon* **2016**, *99*, 238–248.

(81) Zhu, S.; Wang, L.; Zhou, N.; Zhao, X.; Song, Y.; Maharjan, S.; Zhang, J.; Lu, L.; Wang, H.; Yang, B. The Crosslink Enhanced Emission (CEE) in Non-Conjugated Polymer Dots: From the Photoluminescence Mechanism to the Cellular Uptake Mechanism and Internalization. *Chem. Commun.* **2014**, *50*, 13845–13848.

(82) Zhu, S.; Zhao, X.; Song, Y.; Lu, S.; Yang, B. Beyond Bottom-up Carbon Nanodots: Citric-Acid Derived Organic Molecules. *Nano Today* **2015**, *11*, 128–132.

(83) Fan, Z.; Li, Y.; Li, X.; Fan, L.; Zhou, S.; Fang, D.; Yang, S. Surrounding Media Sensitive Photoluminescence of Boron-Doped Graphene Quantum Dots for Highly Fluorescent Dyed Crystals, Chemical Sensing and Bioimaging. *Carbon* **2014**, *70*, 149–156.

(84) Dey, S.; Govindaraj, a.; Biswas, K.; Rao, C. N. R. Luminescence Properties of Boron and Nitrogen Doped Graphene Quantum Dots Prepared from Arc-Discharge-Generated Doped Graphene Samples. *Chem. Phys. Lett.* **2014**, *595-596*, 203–208.

(85) Dong, Y.; Pang, H.; Yang, H. Bin; Guo, C.; Shao, J.; Chi, Y.; Li, C. M.; Yu, T. Carbon-Based Dots Co-Doped with Nitrogen and Sulfur for High Quantum Yield and Excitation-Independent Emission. *Angew. Chem. Int. Ed.* **2013**, *52*, 7800–7804.

(86) Hu, S.; Tian, R.; Dong, Y.; Yang, J.; Liu, J.; Chang, Q. Modulation and Effects of Surface Groups on Photoluminescence and Photocatalytic Activity of Carbon Dots. *Nanoscale* **2013**, *5*, 11665–11671.

(87) Liu, Q.; Guo, B.; Rao, Z.; Zhang, B.; Gong, J. R. Strong Two-Photon-Induced Fluorescence from Photostable, Biocompatible Nitrogen-Doped Graphene Quantum Dots for Cellular and Deep-Tissue Imaging. *Nano Lett.* **2013**, *13*, 2436–2441.

(88) Yeh, T.-F.; Teng, C.-Y.; Chen, S.-J.; Teng, H. Nitrogen-Doped Graphene Oxide Quantum Dots as Photocatalysts for Overall Water-Splitting under Visible Light Illumination. *Adv. Mater.* **2014**, *26*, 3297–3303.

(89) Sun, Y.; Wang, S.; Li, C.; Luo, P.; Tao, L.; Wei, Y.; Shi, G. Large Scale Preparation of Graphene Quantum Dots from Graphite with Tunable Fluorescence Properties. *Phys. Chem. Chem. Phys.* **2013**, *15*, 9907–9913.

(90) Dong, Y.; Shao, J.; Chen, C.; Li, H.; Wang, R.; Chi, Y.; Lin, X.; Chen, G. Blue Luminescent Graphene Quantum Dots and Graphene Oxide Prepared by Tuning the Carbonization Degree of Citric Acid. *Carbon* **2012**, *50*, 4738–4743.

(91) Ray, S. C.; Saha, A.; Jana, N. R.; Sarkar, R. Fluorescent Carbon Nanoparticles: Synthesis, Characterization, and Bioimaging Application. *J. Phys. Chem. C* **2009**, *113*, 18546–18551.

(92) Bhunia, S. K.; Saha, A.; Maity, A. R.; Ray, S. C.; Jana, N. R. Carbon Nanoparticle-Based Fluorescent Bioimaging Probes. *Sci. Rep.* **2013**, *3*, 1473.

(93) Wei, W.; Xu, C.; Wu, L.; Wang, J.; Ren, J.; Qu, X. Non-Enzymatic-Browning-Reaction: A Versatile Route for Production of Nitrogen-Doped Carbon Dots with Tunable Multicolor Luminescent Display. *Sci. Rep.* **2014**, *4*, 3564.

(94) Qu, S.; Wang, X.; Lu, Q.; Liu, X.; Wang, L. A Biocompatible Fluorescent Ink Based on Water-Soluble Luminescent Carbon Nanodots. *Angew. Chem. Int. Ed.* **2012**, *51*, 12215–12218.

(95) Zhang, M.; Bai, L.; Shang, W.; Xie, W.; Ma, H.; Fu, Y.; Fang, D.; Sun, H.; Fan, L.; Han, M.; *et al.* Facile Synthesis of Water-Soluble, Highly Fluorescent Graphene Quantum Dots as a Robust Biological Label for Stem Cells. *J. Mater. Chem.* **2012**, *22*, 7461–7467.

(96) Liu, H.; Ye, T.; Mao, C. Fluorescent Carbon Nanoparticles Derived from Candle Soot. *Angew. Chemie Int. Ed.* **2007**, *46*, 6473–6475.

(97) Kosynkin, D. V; Higginbotham, A. L.; Sinitskii, A.; Lomeda, J. R.; Dimiev, A.; Price, B. K.; Tour, J. M. Longitudinal Unzipping of Carbon Nanotubes to Form Graphene Nanoribbons. *Nature* **2009**, *458*, 872–876.

(98) Lu, J.; Yeo, P. S. E.; Gan, C. K.; Wu, P.; Loh, K. P. Transforming C60 Molecules into Graphene Quantum Dots. *Nat. Nanotechnol.* **2011**, *6*, 247–252.

(99) Jin, S. H.; Kim, D. H.; Jun, G. H.; Hong, S. H.; Jeon, S. Tuning the Photoluminescence of Graphene Quantum Dots through the Charge Transfer Effect of Functional Groups. *ACS Nano* **2013**, *7*, 1239–1245.

(100) Long, Y.-M.; Zhou, C.-H.; Zhang, Z.-L.; Tian, Z.-Q.; Bao, L.; Lin, Y.; Pang, D.-W. Shifting and Non-Shifting Fluorescence Emitted by Carbon Nanodots. *J. Mater. Chem.* **2012**, *22*, 5917–5920.

(101) Zhou, J.; Booker, C.; Li, R.; Zhou, X.; Sham, T. An Electrochemical Avenue to Blue Luminescent Nanocrystals from Multiwalled Carbon Nanotubes (MWCNTs). *J. Am. Chem. Soc.* **2007**, *8*, 744–745.

(102) Zheng, L.; Chi, Y.; Dong, Y.; Lin, J.; Wang, B. Electrochemiluminescence of Water-Soluble Carbon Nanocrystals

Released Electrochemically from Graphite. *J. Am. Chem. Soc.* **2009**, *131*, 4564–4565.

(103) Bourlinos, A. B.; Stassinopoulos, A.; Anglos, D.; Zboril, R.; Georgakilas, V.; Giannelis, E. P. Photoluminescent Carbogenic Dots. *Chem. Mater* **2008**, *20*, 4539–4541.

(104) Bourlinos, A. B.; Stassinopoulos, A.; Anglos, D.; Zboril, R.; Karakassides, M.; Giannelis, E. P. Surface Functionalized Carbogenic Quantum Dots. *Small* **2008**, *4*, 455–458.

(105) Bourlinos, A. B.; Zboril, R.; Petr, J.; Bakandritsos, A.; Krysmann, M.; Giannelis, E. P. Luminescent Surface Quaternized Carbon Dots. *Chem. Mater* **2012**, *24*, 6–8.

(106) Babar, D. G.; Sonkar, S. K.; Tripathi, K. M.; Sarkar, S. P2O5 Assisted Green Synthesis of Multicolor Fluorescent Water Soluble Carbon Dots. *J. Nanosci. Nanotechnol.* **2014**, *14*, 2334–2342.

(107) Zhu, H.; Wang, X.; Li, Y.; Wang, Z.; Yang, F.; Yang, X. Microwave Synthesis of Fluorescent Carbon Nanoparticles with Electrochemiluminescence Properties. *Chem. Commun* **2009**, *34*, 5118–5120.

(108) Qu, D.; Zheng, M.; Zhang, L.; Zhao, H.; Xie, Z.; Jing, X.; Haddad, R. E.; Fan, H.; Sun, Z. Formation Mechanism and Optimization of Highly Luminescent N-Doped Graphene Quantum Dots. *Sci. Rep.* **2014**, *4*, 5294.

(109) Bourlinos, A. B.; Karakassides, M. a.; Kouloumpis, A.; Gournis, D.; Bakandritsos, A.; Papagiannouli, I.; Aloukos, P.; Couris, S.; Hola, K.; Zboril, R.; *et al.* Synthesis, Characterization and Non-Linear Optical Response of Organophilic Carbon Dots. *Carbon* **2013**, *61*, 640–649.

(110) Wang, C.; Jiang, K.; Wu, Q.; Wu, J.; Zhang, C. Green Synthesis of Red-Emitting Carbon Nanodots as a Novel “Turn-On” Nanothermometer in Living Cells. *Chem. - A Eur. J.* **2016**, *22*, 14475–14479.

(111) Wang, L.; Wang, Y.; Xu, T.; Liao, H.; Yao, C.; Liu, Y.; Li, Z.; Chen, Z.; Pan, D.; Sun, L.; *et al.* Gram-Scale Synthesis of Single-Crystalline Graphene Quantum Dots with Superior Optical Properties. *Nat. Commun.* **2014**, *5*, 5357.

(112) Erickson, H. P. Size and Shape of Protein Molecules at the Nanometer Level Determined by Sedimentation, Gel Filtration, and Electron Microscopy. *Biol. Proced. Online* **2009**, *11*, 32–51.

(113) Choi, H. S.; Liu, W.; Misra, P.; Tanaka, E.; Zimmer, J. P.; Itty Ipe, B.; Bawendi, M. G.; Frangioni, J. V. Renal Clearance of Quantum Dots. *Nat. Biotechnol.* **2007**, *25*, 1165–1170.

(114) Sahu, S.; Behera, B.; Maiti, T. K.; Mohapatra, S. Simple One-Step Synthesis of Highly Luminescent Carbon Dots from Orange Juice: Application as Excellent Bio-Imaging Agents. *Chem. Commun.* **2012**, *48*, 8835–8837.

(115) Jiang, K.; Sun, S.; Zhang, L.; Lu, Y.; Wu, A.; Cai, C.; Lin, H. Red, Green, and Blue Luminescence by Carbon Dots: Full-Color Emission Tuning and Multicolor Cellular Imaging. *Angew. Chemie - Int. Ed.* **2015**, *54*, 5360–5363.

(116) Bourlinos, A. B.; Trivizas, G.; Karakassides, M. a.; Baikousi, M.; Kouloumpis, A.; Gournis, D.; Bakandritsos, A.; Hola, K.; Kozak, O.; Zboril, R.; *et al.* Green and Simple Route toward Boron Doped Carbon Dots with Significantly Enhanced Non-Linear Optical Properties. *Carbon* **2015**, *83*, 173–179.

(117) Ding, C.; Zhu, A.; Tian, Y. Functional Surface Engineering of C-Dots for Fluorescent Biosensing and in Vivo Bioimaging. *Acc. Chem. Res.* **2014**, *47*, 20–30.

(118) Cao, L.; Wang, X.; Meziani, M. J.; Lu, F.; Wang, H.; Luo, P. G.; Lin, Y.; Harruff, B. a; Veca, L. M.; Murray, D.; *et al.* Carbon Dots for Multiphoton Bioimaging. *J. Am. Chem. Soc.* **2007**, *129*, 11318–11319.

(119) Pan, L.; Sun, S.; Zhang, L.; Jiang, K.; Lin, H. Near-Infrared Emissive Carbon Dots for Two-Photon Fluorescence Bioimaging. *Nanoscale* **2016**, *8*, 17350–17356.

(120) Luk, C. M.; Tsang, M. K.; Chan, C. F.; Lau, S. P. Two-Photon Fluorescence in N-Doped Graphene Quantum Dots. *Int. Sch. Sci. Res. Innov.* **2014**, *8*, 1310–1313.

(121) Wen, X.; Yu, P.; Toh, Y.-R.; Ma, X.; Tang, J. On the Upconversion Fluorescence in Carbon Nanodots and Graphene Quantum Dots. *Chem. Commun.* **2014**, *50*, 4703–4706.

(122) Wang, Y.; Kalytchuk, S.; Zhang, Y.; Shi, H.; Kershaw, S. V; Rogach, A. L. Thickness-Dependent Full-Color Emission Tunability in a Flexible Carbon Dot Ionogel. *J. Phys. Chem. Lett.* **2014**, *5*, 1412–1420.

(123) Mueller, M. L.; Yan, X.; McGuire, J. a; Li, L. Triplet States and Electronic Relaxation in Photoexcited Graphene Quantum Dots. *Nano Lett.* **2010**, *10*, 2679–2682.

(124) Sun, X.; Liu, Z.; Welsher, K.; Robinson, J. T.; Goodwin, A.; Zaric, S.; Dai, H. Nano-Graphene Oxide for Cellular Imaging and Drug Delivery. *Nano Res* **2008**, *1*, 203–212.

(125) Shang, J.; Ma, L.; Li, J.; Ai, W.; Yu, T.; Gurzadyan, G. G. The Origin of Fluorescence from Graphene Oxide. *Sci. Rep.* **2012**, *2*, 792.

(126) Chien, C. T.; Li, S. S.; Lai, W. J.; Yeh, Y. C.; Chen, H. A.; Chen, I. S.; Chen, L. C.; Chen, K. H.; Nemoto, T.; Isoda, S.; *et al.* Tunable Photoluminescence from Graphene Oxide. *Angew. Chemie - Int. Ed.* **2012**, *51*, 6662–6666.

(127) Hens, S. C.; Lawrence, W. G.; Kumbhar, A. S.; Shenderova, O. Photoluminescent Nanostructures from Graphite Oxidation. *J. Phys. Chem. C* **2012**, *116*, 20015–20022.

(128) Ma, M.; Hu, X.; Zhang, C.; Deng, C.; Wang, X. The Optimum Parameters to Synthesize Bright and Stable Graphene Quantum Dots by Hydrothermal Method. *J. Mater. Sci. Mater. Electron.* **2017**, 10.1007/s10854–017 – 6337–4.

(129) Thomas, H. R.; Vallés, C.; Young, R. J.; Kinloch, I. a.; Wilson, N. R.; Rourke, J. P. Identifying the Fluorescence of Graphene Oxide. *J. Mater. Chem. C* **2013**, *1*, 338–342.

(130) Pu, S.-C.; Yang, M.-J.; Hsu, C.-C.; Lai, C.-W.; Hsieh, C.-C.; Lin, S. H.; Cheng, Y.-M.; Chou, P.-T. The Empirical Correlation between Size and Two-Photon Absorption Cross Section of CdSe and CdTe Quantum Dots. *Small* **2006**, *2*, 1308–1313.

(131) Tan, X.; Li, Y.; Li, X.; Zhou, S.; Fan, L.; Yang, S. Electrochemical Synthesis of Small-Sized Red Fluorescent Graphene Quantum Dots as a Bioimaging Platform. *Chem. Commun. (Camb).* **2015**, *51*, 2544–2546.

(132) Wei, J.; Qiu, J. Unveil the Fluorescence of Carbon Quantum Dots. *Adv. Eng. Mater.* **2015**, *17*, 138–142.

(133) Ding, H.; Yu, S.-B.; Wei, J.-S.; Xiong, H.-M. Full-Color Light-Emitting Carbon Dots with a Surface-State-Controlled Luminescence Mechanism. *ACS Nano* **2016**, *10*, 484–491.

(134) Fu, M.; Ehrat, F.; Wang, Y.; Milowska, K. Z.; Reckmeier, C.; Rogach, A. L.; Stolarczyk, J. K.; Urban, A. S.; Feldmann, J. Carbon Dots: A Unique Fluorescent Cocktail of Polycyclic Aromatic Hydrocarbons. *Nano Lett.* **2015**, *15*, 6030–6035.

(135) Vinci, J. C.; Ferrer, I. M.; Seedhouse, S. J.; Bourdon, A. K.; Reynard, J. M.; Foster, B. A.; Bright, F. V; Colon, L. A. Hidden Properties of Carbon Dots Revealed After HPLC Fractionation. *J. Phys. Chem. Lett.* **2013**, *4*, 239–243.

(136) Nquyen, V.; Si, J.; Yan, L.; Hou, X. Direct Demonstration of Photoluminescence Originated from Surface Functional Groups in Carbon Nanodots. *Carbon* **2016**, *108*, 268–273.

(137) Zhu, S.; Zhang, J.; Tang, S.; Qiao, C.; Wang, L.; Wang, H.; Liu, X.; Li, B.; Li, Y.; Yu, W.; *et al.* Surface Chemistry Routes to Modulate the Photoluminescence of Graphene Quantum Dots: From Fluorescence Mechanism to Up-Conversion Bioimaging Applications. *Adv. Funct. Mater.* **2012**, *22*, 4732–4740.

(138) Cushing, S. K.; Li, M.; Huang, F.; Wu, N. Origin of Strong Excitation Wavelength Dependent Fluorescence of Graphene Oxide. *ACS Nano* **2014**, *8*, 1002–1013.

(139) Gan, Z.; Xu, H.; Hao, Y. Mechanism for Excitation-Dependent Photoluminescence from Graphene Quantum Dots and Other Graphene Oxide Derivates: Consensus, Debates and Challenges. *Nanoscale* **2016**, *8*, 7794–7807.

(140) Cushing, S. K.; Ding, W.; Chen, G.; Wang, C.; Yang, F.; Huang, F.; Wu, N. Excitation Wavelength Dependent Fluorescence of Graphene Oxide Controlled by Strain. *Nanoscale* **2017**, *9*, 2240–2245.

(141) Tetsuka, H.; Asahi, R.; Nagoya, A.; Okamoto, K.; Tajima, I.; Ohta, R.; Okamoto, A. Optically Tunable Amino-Functionalized Graphene Quantum Dots. *Adv. Mater.* **2012**, *24*, 5333–5338.

(142) Biju, V. Chemical Modifications and Bioconjugate Reactions of Nanomaterials for Sensing, Imaging, Drug Delivery and Therapy. *Chem. Soc. Rev.* **2014**, *43*, 744–764.

(143) Li, N.; Liang, X.; Wang, L.; Li, Z.; Li, P.; Zhu, Y.; Song, J. Biodistribution Study of Carbogenic Dots in Cells and in Vivo for Optical Imaging. *J. Nanoparticle Res.* **2012**, *14*, 1177.

(144) Ruan, S.; Zhu, B.; Zhang, H.; Chen, J.; Shen, S.; Qian, J.; He, Q.; Gao, H. A Simple One-Step Method for Preparation of Fluorescent Carbon Nanospheres and the Potential Application in Cell Organelles Imaging. *J. Colloid Interface Sci.* **2014**, *422*, 25–29.

(145) Datta, K. K. R.; Kozak, O.; Ranc, V.; Havrdova, M.; Bourlinos, A. B.; Safarova, K.; Hola, K.; Tomankova, K.; Zoppellaro, G.; Otyepka, M.; *et al.* Quaternized Carbon Dots Modified Graphene Oxide for Selective Cell Labelling – Controlled Nucleus and Cytoplasm Imaging. *Chem. Commun.* **2014**, *50*, 10782–10785.

(146) Nair, R. R.; Ren, W.; Jalil, R.; Riaz, I.; Kravets, V. G.; Britnell, L.; Blake, P.; Schedin, F.; Mayorov, A. S.; Yuan, S.; *et al.* Fluorographene: A Two-Dimensional Counterpart of Teflon. *Small* **2010**, *6*, 2877–2884.

(147) Robinson, J. T.; Burgess, J. S.; Junkermeier, C. E.; Badescu, S. C.; Reinecke, T. L.; Perkins, F. K.; Zalalutdniov, M. K.; Baldwin, J. W.; Culbertson, J. C.; Sheehan, P. E.; *et al.* Properties of Fluorinated Graphene Films. *Nano Lett.* **2010**, *10*, 3001–3005.

(148) Cheng, S. H.; Zou, K.; Okino, F.; Gutierrez, H. R.; Gupta, a.; Shen, N.; Eklund, P. C.; Sofo, J. O.; Zhu, J. Reversible Fluorination of Graphene: Evidence of a Two-Dimensional Wide Bandgap Semiconductor. *Phys. Rev. B - Condens. Matter Mater. Phys.* **2010**, *81*, 1–5.

(149) Withers, F.; Dubois, M.; Savchenko, a. K. Electron Properties of Fluorinated Single-Layer Graphene Transistors. *Phys. Rev. B - Condens. Matter Mater. Phys.* **2010**, *82*, 1–4.

(150) Zboril, R.; Karlicky, F.; Bourlinos, A. B.; Steriotis, T. a.; Stubos, A. K.; Georgakilas, V.; Safarova, K.; Jancik, D.; Trapalis, C.; Otyepka, M. Graphene Fluoride: A Stable Stoichiometric Graphene Derivative and Its Chemical Conversion to Graphene. *Small* **2010**, *6*, 2885–2891.

(151) Pykal, M.; Zboril, R.; Otyepka, M. Fluorografen – Benjaminek v Rodine Grafenovych Derivatu. *Chem. List.* **2016**, *110*, 335–343.

(152) Zhu, M.; Xie, X.; Guo, Y.; Chen, P.; Ou, X.; Yu, G.; Liu, M. Fluorographene Nanosheets with Broad Solvent Dispersibility and Their Applications as a Modified Layer in Organic Field-Effect Transistors. *Phys. Chem. Chem. Phys.* **2013**, *15*, 20992–21000.

(153) Samarakoon, D. K.; Chen, Z.; Nicolas, C.; Wang, X. Q. Structural and Electronic Properties of Fluorographene. *Small* **2011**, *7*, 965–969.

(154) Karlický, F.; Kumara Ramanatha Datta, K.; Otyepka, M.; Zbořil, R. Halogenated Graphenes: Rapidly Growing Family of Graphene Derivatives. *ACS Nano* **2013**, *7*, 6434–6464.

(155) Karlický, F.; Otyepka, M. Band Gaps of Chlorographene , Fluorographene and Graphane from G0W0, GW0 and GW Calculations on Top Od PBE and HSE06 Orbitals. *J. Chem. Theory Comput.* **2013**, *9*, 4155–4164.

(156) Nair, R. R.; Sepioni, M.; Tsai, I.-L.; Lehtinen, O.; Keinonen, J.; Krasheninnikov, a. V.; Thomson, T.; Geim, a. K.; Grigorieva, I. V. Spin-Half Paramagnetism in Graphene Induced by Point Defects. *Nat. Phys.* **2012**, *8*, 199–202.

(157) Tao, H.; Yang, K.; Ma, Z.; Wan, J.; Zhang, Y.; Kang, Z.; Liu, Z. In Vivo NIR Fluorescence Imaging, Biodistribution, and Toxicology of Photoluminescent Carbon Dots Produced from Carbon Nanotubes and Graphite. *Small* **2012**, *8*, 281–290.

(158) Yang, S.-T.; Wang, X.; Wang, H.; Lu, F.; Luo, P. G.; Cao, L.; Meziani, M. J.; Liu, J.-H.; Liu, Y.; Chen, M.; *et al.* Carbon Dots as Nontoxic and High-Performance Fluorescence Imaging Agents. *J. Phys. Chem. C* **2009**, *113*, 18110–18114.

(159) Zhu, S.; Tang, S.; Zhang, J.; Yang, B. Control the Size and Surface Chemistry of Graphene for the Rising Fluorescent Materials. *Chem. Commun.* **2012**, *48*, 4527–4539.

(160) Yu, P.; Wen, X.; Toh, Y.-R.; Tang, J. Temperature-Dependent Fluorescence in Carbon Dots. *J. Phys. Chem. C* **2012**, *116*, 25552–25557.

(161) Li, H.; Kang, Z.; Liu, Y.; Lee, S.-T. Carbon Nanodots: Synthesis, Properties and Applications. *J. Mater. Chem.* **2012**, *22*, 24230–24353.

(162) Yang, S.-T.; Cao, L.; Luo, P. G.; Lu, F.; Wang, X.; Wang, H.; Meziani, M. J.; Liu, Y.; Qi, G.; Sun, Y.-P. Carbon Dots for Optical Imaging in Vivo. *J. Am. Chem. Soc.* **2009**, *131*, 11308–11309.

(163) Wang, F.; Pang, S.; Wang, L.; Li, Q.; Kreiter, M.; Liu, C. One-Step Synthesis of Highly Luminescent Carbon Dots in Noncoordinating Solvents. *Chem. Mater.* **2010**, *22*, 4528–4530.

(164) Agostinis, P.; Berg, K.; Cengel, K. A.; Foster, T. H.; Girotti, A. W.; Gollnick, S. O.; Hahn, S. M.; Hamblin, M. R.; Juzeniene, A.; Kessel, D.; *et al.* Photodynamic Therapy of Cancer : An Update. *CA Cancer J. Clin.* **2011**, *61*, 250.

(165) Zhang, X.; Zhang, Y.; Wang, Y.; Kalytchuk, S.; Kershaw, S. V; Wang, Y.; Wang, P.; Zhang, T.; Zhao, Y.; Zhang, H.; *et al.* Color-Switchable Electroluminescence of Carbon Dot Light-Emitting Diodes. *ACS Nano* **2013**, *7*, 11234–11241.

(166) Liu, J.-H.; Anilkumar, P.; Cao, L.; Wang, X.; Yang, S.-T.; Luo, P. G.; Wang, H.; Lu, F.; Meziani, M. J.; Liu, Y.; *et al.* Cytotoxicity Evaluations of Fluorescent Carbon Nanoparticles. *Nano Life* **2010**, *01*, 153–161.

(167) Wang, Y.; Anilkumar, P.; Cao, L.; Liu, J.-H.; Luo, P. G.; Tackett, K. N.; Sahu, S.; Wang, P.; Wang, X.; Sun, Y.-P. Carbon Dots of Different Composition and Surface Functionalization: Cytotoxicity Issues Relevant to Fluorescence Cell Imaging. *Exp. Biol. Med.* **2011**, *236*, 1231–1238.

(168) Wang, K.; Gao, Z.; Gao, G.; Wo, Y.; Wang, Y.; Shen, G.; Cui, D. Systematic Safety Evaluation on Photoluminescent Carbon Dots. *Nanoscale Res. Lett.* **2013**, *8*, 122.

(169) Huang, X.; Zhang, F.; Zhu, L.; Choi, K. Y.; Guo, N.; Guo, J.; Tackett, K.; Anilkumar, P.; Liu, G.; Quan, Q.; *et al.* Effect of Injection Routes on the Tumor Uptake of Carbon Dots. *ACS Nano* **2013**, *7*, 5684–5693.

(170) Nie, S. Understanding and Overcoming Major Barriers in Cancer Nanomedicine. *Nanomedicine* **2010**, *5*, 523–528.

(171) Dai, Q.; Duty, C. E.; Hu, M. Z. Semiconductor-Nanocrystals-Based White Light-Emitting Diodes. *Small* **2010**, *6*, 1577–1588.

(172) Tang, J.; Kong, B.; Wu, H.; Xu, M.; Wang, Y.; Wang, Y.; Zhao, D.; Zheng, G. Carbon Nanodots Featuring Efficient FRET for Real-Time Monitoring of Drug Delivery and Two-Photon Imaging. *Adv. Mater.* **2013**, *25*, 6569–6574.

(173) Wang, H.; Shen, J.; Li, Y.; Wei, Z.; Cao, G.; Gai, Z.; Hong, K.; Banerjee, P.; Zhou, S. Magnetic Iron Oxide–fluorescent Carbon Dots Integrated Nanoparticles for Dual-Modal Imaging, near-Infrared Light-Responsive Drug Carrier and Photothermal Therapy. *Biomater. Sci.* **2014**, *2*, 915–923.

(174) Markovic, Z. M.; Ristic, B. Z.; Arsikin, K. M.; Klisic, D. G.; Harhaji-Trajkovic, L. M.; Todorovic-Markovic, B. M.; Kepic, D. P.; Kravic-Stevovic, T. K.; Jovanovic, S. P.; Milenkovic, M. M.; *et al.* Graphene Quantum Dots as Autophagy-Inducing Photodynamic Agents. *Biomaterials* **2012**, *33*, 7084–7092.

(175) Christensen, I. L.; Sun, Y.-P.; Juzenas, P. Carbon Dots as Antioxidants and Prooxidants. *J. Biomed. Nanotechnol.* **2011**, *7*, 667–676.

(176) Chung, W.; Jung, H.; Lee, C. H.; Kim, S. H. Fabrication of High Color Rendering Index White LED Using Cd-Free Wavelength Tunable Zn Doped CuInS2 Nanocrystals. *Opt. Express* **2012**, *20*, 25071–25076.

(177) Zhang, Y.; Xie, C.; Su, H.; Liu, J.; Pickering, S.; Wang, Y.; Yu, W. W.; Wang, J.; Wang, Y.; Hahm, J.; *et al.* Employing Heavy Metal-Free Colloidal Quantum Dots in Solution-Processed White Light-Emitting Diodes. *Nano Lett.* **2011**, *11*, 329–332.

(178) Wang, F.; Chen, Y.; Liu, C.; Ma, D. White Light-Emitting Devices Based on Carbon Dots' Electroluminescence. *Chem. Commun.* **2011**, *47*, 3502–3504.

(179) Hui Nie, Minjie Li, Quanshun Li, Shaojun Liang, Yingying Tan, Lan Sheng, W. S. and S. X.-A. Z. Carbon Dots with Continuously Tunable Full-Colour Emission and Their Application in Ratiometric pH Sensing. *Chem. Mater.* **2014**, *26*, 3104–3112.

(180) Khan, S.; Gupta, A.; Verma, N. C.; Nandi, C. K. Time-Resolved Emission Reveals Ensemble of Emissive States as the Origin of Multicolor Fluorescence in Carbon Dots. *Nano Lett.* **2015**, *15*, 8300–8305.

(181) Bao, L.; Liu, C.; Zhang, Z. L.; Pang, D. W. Photoluminescence-Tunable Carbon Nanodots: Surface-State Energy-Gap Tuning. *Adv. Mater.* **2015**, *27*, 1663–1667.

(182) Pumera, M. Electrochemistry of Graphene, Graphene Oxide and Other Graphenoids: Review. *Electrochem. commun.* **2013**, *36*, 14–18.

(183) Dreyer, D. R.; Park, S.; Bielawski, C. W.; Ruoff, R. S. The Chemistry of Graphene Oxide. *Chem. Soc. Rev.* **2010**, *39*, 228–240.

(184) Pumera, M.; Wong, C. H. A. Graphene and Hydrogenated Graphene. *Chem. Soc. Rev.* **2013**, *42*, 5987–5995.

(185) Lin-Vien, D.; Colthup, N. B.; Fateley, W. G.; Grasselli, J. G. *The Handbook of Infrared and Raman Characteristic Frequencies of Organic Molecules*; 1991; pp. 225–250.

(186) Castro-Neto, a. H.; Peres, N. M. R.; Novoselov, K. S.; Geim, a. K. The Electronic Properties of Graphene. *Rev. Mod. Phys.* **2009**, *81*, 109–162.

(187) Fialkovsky, I. V; Marachevsky, V. N.; Vassilevich, D. V. Finite Temperature Casimir Effect for Graphene. *Phys. Rev. B* **2011**, *84*, 035446.

(188) Palacios, J. J.; Fernández-Rossier, J.; Brey, L. Vacancy-Induced Magnetism in Graphene and Graphene Ribbons. *Phys. Rev. B - Condens. Matter Mater. Phys.* **2008**, *77*, 195428.

(189) Magda, G. Z.; Jin, X.; Hagymasi, I.; Vancso, P.; Osvath, Z.; Nemes-Incze, P.; Hwang, C.; Biro, L. P.; Tapaszto, L. Room-Temperature Magnetic Order on Zigzag Edges of Narrow Graphene Nanoribbons. *Nature* **2014**, *514*, 608–611.

(190) Cho, D.; Ko, K. C.; Lee, J. Y. Organic Magnetic Diradicals (radical-Coupler-Radical): Standardization of Couplers for Strong Ferromagnetism. *J. Phys. Chem. A* **2014**, *118*, 5112–5121.

A

Photoluminescence Effects of Graphitic Core Size and Surface Functional Groups in Carbon Dots: COO^- Induced Red-shift Emission

carbon 70 (2014) 279–286

Available at www.sciencedirect.com

ScienceDirect

journal homepage: www.elsevier.com/locate/carbon

Photoluminescence effects of graphitic core size and surface functional groups in carbon dots: COO⁻ induced red-shift emission

Katerina Hola [a], *Athanasios B. Bourlinos* [a,b], *Ondrej Kozak* [a], *Karel Berka* [a], *Karolina M. Siskova* [a], *Marketa Havrdova* [a], *Jiri Tucek* [a], *Klara Safarova* [a], *Michal Otyepka* [a], *Emmanuel P. Giannelis* [c,d,*], *Radek Zboril* [a,*]

[a] *Regional Centre of Advanced Technologies and Materials, Faculty of Science, Department of Physical Chemistry, Palacky University, Olomouc 77146, Czech Republic*
[b] *Physics Department, University of Ioannina, Ioannina 45110, Greece*
[c] *Materials Science and Engineering, Cornell University, Ithaca, 14853 NY, USA*
[d] *Center for Refining & Petrochemicals, KFUPM, Dhahran 31261, Saudi Arabia*

A R T I C L E   I N F O

Article history:
Received 9 November 2013
Accepted 6 January 2014
Available online 11 January 2014

A B S T R A C T

We present a simple molecular approach to control the lipophilic/hydrophilic nature of photoluminescent carbon dots (CDs) based on pyrolysis of alkyl gallate precursors. Depending on the gallic acid derivative used, CDs with different alkyl groups (methyl, propyl, lauryl) on the surface can be obtained by isothermal heating at 270 °C. This precursor-derived approach allows not only the control of lipophilicity but also the length of the particular alkyl chain enables the control over both the size and photoluminescence (PL) of the prepared CDs. Moreover, the alkyl chains on the CDs surface can be readily converted to carboxylate groups via a mild base hydrolysis to obtain water dispersible CDs with a record biocompatibility. The observed differences in PL properties of CDs and time-resolved PL data, including contributions from carbogenic cores and surface functional group, are rationalized and discussed in detail using time-dependent density functional theory (TD-DFT) calculations.

© 2014 Elsevier Ltd. All rights reserved.

1. Introduction

Fluorescent carbon dots (CDs) have received considerable attention since their first serendipitous discovery mainly due to their easy and inexpensive preparation, fluorescent emission and low toxicity [1–4]. Many studies have been recently devoted to understanding the fluorescence mechanism of CDs [2,5–10]. It is well-accepted that the fluorescence of CDs is excitation dependent. In some cases, size seems also to have an effect on fluorescence similar to quantum dots. Recently, Vinci et al. [11] have separated CDs by HPLC. They confirmed the complexity of CDs as an ensemble of particles with different sizes and photoluminescence (PL) properties resulting in the wavelength-dependent/multicolour emission [11]. In another study, Zhu et al. reported a blue-shifted emission from graphene dots (GDs, consisting of 5 layers of graphene in maximum [12–16]) after surface modification by alkyl chains [17]. This

---

[*] *Corresponding authors at:* Materials Science and Engineering, Cornell University, Ithaca, 14853 NY, USA. Fax: +420 585634761 (R. Zboril), +1 6072552365 (E.P. Giannelis).
E-mail addresses: epg2@cornell.edu (E.P. Giannelis), radek.zboril@upol.cz (R. Zboril).

0008-6223/$ - see front matter © 2014 Elsevier Ltd. All rights reserved.
http://dx.doi.org/10.1016/j.carbon.2014.01.008

effect was explained by a competition between the defect-state green-related emission from the surface and the intrinsic blue emission [17]. The functionalization by alkyl chains decreases the emission from defect states and makes the intrinsic emission dominant [17]. Similarly, Jin et al. [6] reported an almost 30 nm red shift after the functionalization of GDs by amine groups. This shift was explained by the contribution of unpaired electrons from nitrogen to the conjugated graphene layers [6]. In another study, Hu et al. [18] reported the effect of nitrogen and chlorine surface groups on photoluminescence and photocatalytic activity. The differently charged surface groups led to separation of electron–hole pairs causing better photocatalytic activity of CDs with chlorine and better photoluminescence of CDs with nitrogen on the surface [18]. From the above mentioned it can be seen that understanding of the mechanism of CDs photoluminescence is critical for tuning their fluorescence properties and plays a crucial role for their various applications.

Many different approaches for the synthesis of CDs/GDs have been reported including laser ablation [19], hydrothermal oxidation of graphite [20,21], pyrolysis of molecular precursors [22–26] or extreme dehydration of a carbon source [27,28]. However, controlling their size and surface chemistry still remains a challenge. Up to now, three approaches for size control have been developed. In the first method, based on electrochemical synthesis, the size is controlled by the applied potential [29]. The second utilizes polymeric nanoparticles as a precursors usually prepared under demanding syntheses [9]. The third method is based on preparation of CDs in mesoporous silica [30]. The surface chemistry of CDs can be generally controlled during their formation mainly by the choice of the precursor [22–24]. This so-called "molecular synthesis" proceeds in a single step providing surface-functionalized nanoparticles dispersible in aqueous or organic solvents depending on their surface chemistry.

Gallic acid derivatives provide a general platform for molecular synthesis of CDs. They contain both a carbon source (benzene ring) for thermal oxidation and a surface modifier in the form of an alkyl group. Furthermore, gallate derivatives are natural non-toxic compounds and powerful antioxidants [31]. Additionally, they offer the possibility of obtaining biocompatible CDs. Moreover, the broad range of gallic acid esters can provide CDs with various lipophilic properties.

Herein, we report the synthesis of CDs with controlled size and surface chemistry from simple gallate molecular precursors. Organo-dispersible derivatives are obtained by mild thermal treatment (270 °C) of three gallate esters (lauryl, propyl, and methyl). The length of alkyl chain of the ester strongly determines the lipophilicity as well as the size of CDs (see Fig. 1). Converting the ester groups on the surface to carboxylate groups by hydrolysis allows the formation of water-dispersible particles with different photoluminescent properties and record biocompatibility. The effect of the surface functional groups and the carbogenic cores on the properties are discussed in detail and rationalized for the first time using time-resolved fluorescence measurements and density functional theory (DFT) calculations.

2. Experimental

2.1. Materials

Lauryl gallate, propyl gallate, methyl gallate and Dowex® 50WX4 hydrogen form (20–50 mesh) were purchased from Sigma Aldrich. The organic solvents and sodium hydroxide were obtained from Penta, Czech Republic.

2.2. Synthesis of CDs with alkyl chains on the surface

The preparation of organophilic dots was performed by thermal treatment of the esters of gallic acid similarly as we had previously reported [32]. The precursors were homogenized using a mortar and pestle prior to use. Afterwards, 1 g of particular alkyl gallate was put into a porcelain crucible and heated in the oven at 270 °C for 2 h in air. After cooling the porcelain crucible down, the obtained solid was extracted by ethanol and the insoluble carbon residues were filtered off. The ethanol was evaporated and the dried material was washed several times with hexane to remove possible organophilic impurities. The obtained CDs were denoted according to the used gallate ester and according to the used temperature during preparation as LG27 (lauryl gallate), PG27 (propyl gallate), and MG27 (methyl gallate), respectively. Finally, the prepared CDs were resuspended in ethanol to obtain brown colloids.

2.3. De-esterification of CDs

10 mg of LG27, PG27, and MG27, respectively, were dissolved in 5 mL of acetone. Subsequently, 5 mL of 0.5 M NaOH was added to these colloids. Resulting dispersions were stirred at laboratory temperature for 12 h. After this mild de-esterification process, the mixtures were placed into a beaker and 50 mL of acetone were added. The excess of acetone led to the formation of unmixable water phase at the bottom of the beaker. This phase (1–2 mL) contained the majority of CDs, approximately 85% (w/w). The aqueous solution of CDs was removed and placed in the oven at 40 °C for 5 h to evaporate the residual acetone from the solution. The residual NaOH was removed by mixing the solution of CDs with cation-exchange dowex (H^+). The obtained CDs were denoted respectively as LG27O, PG27O and MG27O and used in water suspensions for further characterization.

2.4. Characterization techniques

TEM images were obtained using a JEM2010 microscope operated at 160 kV with a point-to-point resolution of 1.9 Å. Size distribution of the prepared CDs was manually determined by collecting 1000 diameter counts in the ImageJ software. FT-IR spectra of the dried samples were recorded on an iS5 FTIR spectrometer (Thermo Nicolet) using a Smart Orbit ZnSe ATR technique (650–4000 cm^{-1}). Raman spectra were recorded on a DXR Raman microscope using the 780 nm excitation line

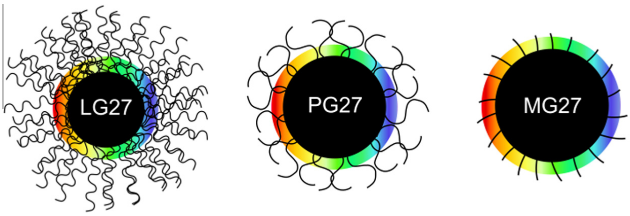

Fig. 1 – Schematic representation of the CDs size control by the length of alkyl chains of the precursors synthesized from lauryl (dodecyl) gallate (LG27), propyl gallate (PG27), and methyl gallate (MG27). (A color version of this figure can be viewed online.)

of a diode laser. The spectra were accumulated for 600 s (with 2 s exposition time) employing 50 μm slit, grating of 830 lines/mm and thermoelectrically cooled detector. Steady-state and time-resolved photoluminescence studies were performed using QuantaMaster 40 and LaserStrobe Spectrofluorometers (PTI, USA), respectively. A superconducting quantum interference device (SQUID, MPMS XL-7 type, Quantum Design, USA) was employed for magnetization measurements. The temperature dependence of mass susceptibility was measured in the settle mode in the temperature range from 5 to 300 K under an external magnetic field of 1 kOe. Elemental analyses were performed using an Elemental Analyzer Flash 2000. Thermal analysis was recorded on an STA449 C Jupiter-Netzsch with a heating rate of 2 °C per minute. Colorimetric MTT assays have been used for biocompatibility testing of CDs. Human lung fibroblasts (MRC-5) were incubated with the CDs dispersions varying in concentrations in 96 well plates for 24 h. Subsequently, the cells were washed with phosphate buffer solution, incubated with tetrazolium salt and solubilized with dimethyl sulfoxide. Absorbance was measured at 570 nm.

2.5. *DFT calculations*

The structures of coronene, hexabenzocoronene, and tricarboxycoronene were optimized using B3LYP/6–31 + G(d,p) method with Gaussian09 program package [33]. Emission spectra were calculated with TD-DFTB3LYP/6–31 + G(d,p) method, which was shown to provide good absorption and emission spectra [34,35], with optimization of the first out of 6 excited states in vacuum. Calculated ESP charge distribution was plotted on the total density.

3. Results and discussion

3.1. *Physicochemical characterization of QDs*

The prepared CDs from the gallate precursors with various length of the alkyl chain exhibited different size (Figs. 1 and 2, and Fig. S1, Supporting Information). Lauryl gallate with the longest ester chain produced CDs (coded as LG27) with a size of around 2 nm, as shown in the transmission electron microscopy (TEM) image in Fig. 2A. CDs derived from propyl gallate (coded as PG27) and methyl gallate (coded as MG27) had an average size around 3.0 and 3.5 nm, respectively (see Fig. 2B and C). The sizes can be explained by the steric hindrance caused by the alkyl chains. This steric blocking is responsible for different interactions between the carbon source (unreacted benzene rings) during the formation of CDs as depicted in Fig. 1. The longest chain (lauryl) has the largest steric effect, thus, the formed particles were the smallest ones and with narrow size distribution. On the other hand, methyl chains have minimal steric effect and the formed particles were bigger with a broader size distribution. The mean sizes and standard deviations of CDs with different alkyl chains are shown in Fig. 2D.

The difference in lipophilicity of CDs prepared from different gallate precursors were demonstrated by their distribution in the octanol:water (1:1) mixture (Fig. 2E and F). The distribution is strongly determined by the alkyl chains on their surface. MG27 was partly distributed in octanol but resided largely in water, where it formed an unstable and non-transparent white suspension. A similar effect was observed for PG27 but the particles were dispersed mostly in octanol. Finally, LG27 was dispersed only in octanol. This behavior can be attributed to the functionalization of the CDs surface by the corresponding alkyl chains. A set of water-soluble CDs was prepared by mild hydrolysis in 0.5 M NaOH. This de-esterification resulted in water dispersible CDs (coded as LG27O, PG27O, and MG27O) shown in Fig. 2E and F. These particles were no longer dispersible in octanol or any other lipophilic organic solvent. The size and the shape of the particles did not change after de-esterification as shown in Fig. S1, Supporting Information.

Fourier transform infrared (FT-IR) spectroscopy was used to further characterize the new CDs (Fig. S2, S3, and S4, Supporting Information). LG27, PG27, and MG27 all (RG27 – all CDs with alkyl chains) exhibit typical C–H asymmetric and symmetric stretching vibrations around 2930 and 2840 cm^{-1}, respectively. Furthermore, there is a peak around 1685–1710 cm^{-1} in all RG27 samples typical of carbonyl groups in esters. Both sets give clear evidence for the presence of alkyl chains attached on the surface of the dots *via* ester bonds. After de-esterification, two major peaks characteristic for carboxylates [36], at around 1560 and 1385 cm^{-1}, were found in the spectra of LG27O, PG27O, and MG27O. These peaks appear in the spectra probably due to the presence of carboxylate groups in Na$^+$ form (Na$^+$ stemming from sodium hydroxide used during hydrolysis). Furthermore, the collective rocking vibrations typical for long alkyl chains in the region of 720 cm^{-1} are absent in the LG27O sample [37]. Both

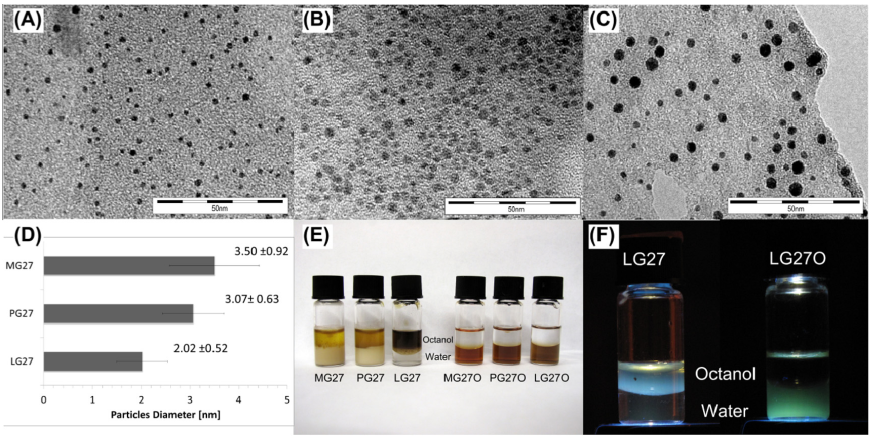

Fig. 2 – TEM images of (A) LG27, (B) PG27, (C) and MG27. (D) Mean size of CDs with standard deviation as determined from TEM images. (E) Demonstration of different distribution coefficients of the CDs in the mixture of octanol and water before (RG27) and after (RG27O) de-esterification in base. (F) CDs from lauryl gallate before (LG27) and after (LG27O) basic de-esterification in octanol/water under UV light. (A color version of this figure can be viewed online.)

observations confirm the de-esterification and subsequent removal of the surface groups from the dots. The negligible residual peaks in the spectra of LG27O and PG27O, observed in the region typical for C–H stretching vibrations (2930 and 2840 cm^{-1}), can be attributed to remaining sp^3 defects which are typical for CDs [38].

Raman spectra in the characteristic region of D and G bands are shown in Fig. S5, Supporting Information, for the RG27 series and LG27O samples. The ratio of spectral intensities of D and G bands (I_D/I_G) decreased: LG27 > PG27 > MG27. This trend is most likely induced by the presence of alkyl chains of a decreasing length (going from LG to MG) influencing graphitization of the carbogenic core. The differences in D band intensities and I_D/I_G ratios of the LG27 and LG27O samples confirm the successful de-esterification process. The residual D band in the LG27O sample can be attributed to sp^3 defects which are typical for CDs [38].

The temperature dependence of the mass susceptibility (χ) measured for the LG27 and MG27 sample is depicted in Fig. S6, Supporting Information. For both samples, a similar trend in χ is observed, *i.e.*, a gradual increase in χ on cooling and appearance of a local maximum at a certain temperature implying a magnetic transition of CDs. While CDs in the LG27 sample show a magnetic transition at ~55 K, CDs in the MG27 sample magnetically order at ~9 K. It is well know that in quantum dots, physical behavior and properties are governed by both finite-size and surface effects [39–41]. Moreover, it has been reported that magnetic ordering in CDs is induced by either an intrinsic disorder or by surface effects [42,43]. As the size of CDs decreases, more atoms are lying in the surface layers significantly enhancing the surface contribution that may dominate over the contribution from the finite-size effects. Hence, with the rise of the surface effects, the magnetic ordering of CDs is expected to occur at higher temperatures. This is consistent with the χ results; for the LG27 samples comprising of CDs with an average size smaller than that of CDs in the MG27 sample, lower magnetic transition temperature is observed (see Fig. S6, Supporting Information).

Additional measurements including thermal and elemental analysis of the materials studied can be found in the Supporting Information (see Fig. S7 and Table S1).

Cytotoxicity measurements were performed to evaluate the biocompatibility of the water-dispersible CDs (MG27O, PG27O, and LG27O). The measurements confirmed the high biocompatibility of the dots. Remarkably the samples denoted as PG27O and LG27O did not show any changes in viability. Even at 1 mg mL^{-1} concentration, the viability was around 100% (see Fig. S8, Supporting Information). This concentration is more than ten times higher than the concentration needed for cell labeling (see Fig. S9, Supporting Information) [2,38]. MG27O almost reached LD_{50} (the median lethal dose) at a concentration of 1 mg mL^{-1}. This different toxicity can be caused by the methanol produced during the de-esterification step. Nevertheless, the CDs LG27O and PG27O samples are highly biocompatible compared to other CDs systems (e.g., almost 60% viability loss for MCF-7 cells was observed for PEG-functionalized CDs at 200 μg mL^{-1} or 90% viability (NIH-3T3 cells) for CDs derived from nanodiamonds at 320 μg mL^{-1}) [44–47]. The record biocompatibility might be due to the antioxidant properties of the precursors used [48,49].

3.2. *Photoluminescent properties*

Steady-state photoluminescence (PL) spectra were measured at fixed excitation wavelength (λ_{ex} = 330 nm) and are shown in Fig. 3. The emission maxima are at 402.0, 427.5, and 428.0 nm for LG27, PG27, and MG27, respectively (Fig. 3A),

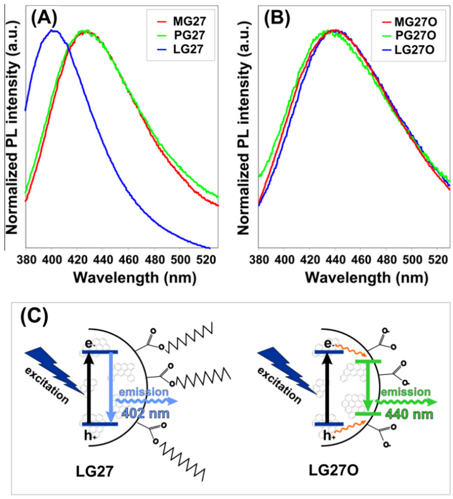

Fig. 3 – Steady-state PL spectra measured at fixed excitation wavelength (λ_{ex} = 330 nm) for (A) RG27 and (B) RG27O. Schematic representation of PL mechanism for LG27 and LG27O. (A color version of this figure can be viewed online.)

consistent with the observed size trend (LG27 < PG27 ⩽ MG27) and typical for semiconductor nanocrystals [50]. However, the emission spectra are virtually identical for the RG27 series despite their different sizes (recall that base hydrolysis had no effect on size as shown in Fig. 3B). It might be that in the LG27 samples, a direct ("excitonic") e-h recombination arising predominantly from the core of the CDs is the prevailing radiative pathway of recombination rather than emission from the surface states the energy of which is commonly referred to be virtually size-independent [51].

To shed more light on the origin of the fluorescence, a more detailed study of the LG27 and LG27O samples was carried out. First, the observed almost 40 nm red shift of the emission maxima after de-esterification (LG27 → LG27O) is not caused by the size change, since the size of the particles remained unchanged (see Fig. S1A, Supporting Information). Instead, we suggest that non-radiative relaxation of the photogenerated e-h pairs prior to the emission accounts for the lower energy of the emitted photon from LG27O. Surface states usually act as charge carrier traps. Emission from these states is always red shifted compared to those originating from the core [52]. We believe that the carboxyl groups on the RG27O (all CDs without alkyl chains) surface play a key role in photoluminescence of water dispersible CDs as emissive surface states. Their impact on the PL properties of RG27 was very likely diminished due to their passivation by the alkyl chains. This hypothesis was supported by the lifetime measurements using a pulsed excitation at 337 nm. The mean lifetimes (τ_m) of LG27 and LG27O detected at different emission wavelengths are summarized in Table 1.

The mean lifetime of LG27 and LG27O at their emission maxima is ~2.32 and ~3.95 ns, respectively. Obviously, the fast process of the prevailing direct e-h radiative recombination results in shorter τ_m in the case of LG27 while the longer τ_m for LG27O correlates with slower, energy-losing e-h pair localization at a surface state followed by a photon emission as depicted in Fig. 3C. Furthermore, while increasing the emission wavelength, the decreasing τ_m of PL from LG27 corresponds to the well described size-dependent radiative decay of excitons in semiconductors – the larger the crystal size the shorter the lifetime of the excitonic PL (also described as superradiant decay) [53]. In analogy with i-type semiconductors, larger CDs emit at longer wavelengths (quantum-size effect) with shorter lifetime (superradiant decay), which indicates the "intrinsic", core-related character of the PL from LG27. On the other hand, the opposite trend observed in the case of LG27O implies that a different PL mechanism governs its fluorescence. More specifically, the longer τ_m found for low-energy radiative recombination (the more red shifted emission the longer the corresponding τ_m) is in agreement with the prolonged charge carrier relaxation to lower-lying energy levels. Comparing Fig. 4A and B, considerable broadening of both the emission range and the excitation range within which the CDs emit (i.e. broadening of PL emission and PL excitation bands, respectively) is obvious. We find two reasons for the observed broadening: (i) the de-esterification led to a broader distribution of density of states which was confirmed by broader UV–VIS absorption spectrum of LG27O after de-esterification (see Fig. S10, Supporting Information) and (ii) the presence of exposed carboxyl groups on the surface enables the more intense electrostatic interaction of LG27O with the solvent resulting in lowering the surface state energies and their broader range as a consequence of the solvent relaxation [54].

The PL properties of RG27 and RG27O were measured in ethanol and water, respectively, to prevent CDs from aggregating. It is well known that the solvent polarity generally affects the fluorescence of polar fluorophores, which is manifested in the so-called solvatochromism [55]. Due to the immense complexity of this phenomenon, it is difficult to assess its effect on the PL properties of the present CDs. To the best of our knowledge, no study dealing with

Table 1 – Mean lifetimes for the LG27 and LG27O samples detected at a given emission wavelength.

Sample	Mean lifetime (ns)			
	370 nm	400 nm	440 nm	500 nm
LG27	2.35	2.32	2.15	–
LG27O	–	3.12	3.95	4.74

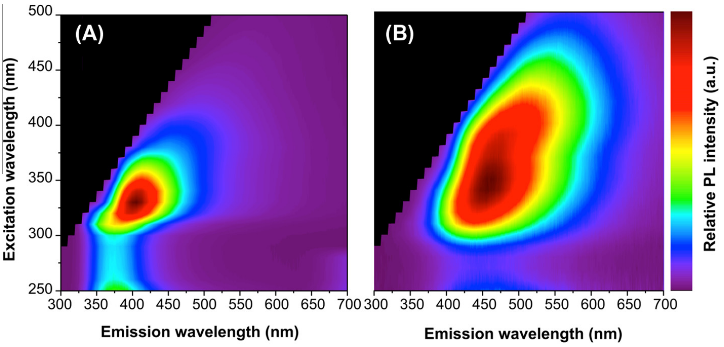

Fig. 4 – Excitation-emission maps for (A) LG27 and (B) LG27O samples. (A color version of this figure can be viewed online.)

solvatochromism of CDs has been published. However, we have made an attempt to get a notion of the CDs solvatochromism by measuring the PL of LG27O in ethanol–water mixture (20:1, v/v). Besides the expected lower PL intensity and increased scattering caused by a slight aggregation, the emission maxima were blue shifted only by 3 nm in ethanol probably due to smaller non-radiative energy loss in the less polar solvent [54]. Obviously, the use of a more polar solvent (water) cannot explain the considerably red shifted emission (38 nm) observed after LG27 de-esterification. Moreover, monitoring the lifetime at various wavelengths and considering different red shifts for CDs derived from different precursors, we find negligible impact of solvatochromism on the PL mechanism in RG27 and RG270 CDs.

3.3. *DFT calculations*

Time-dependent density functional theory (TD-DFT) computations on small model systems – coronene derivatives – were used to rationalize the effects of size of sp^2 parts of CDs core and surface substituent on the optical properties of CDs. The calculated emission maxima (λ_{max}) for these systems were 310 nm for the coronene, 360 nm for the tricarboxycoronene, and 377 nm for the hexabenzocoronene. Methyl ester and propyl ester of tricarboxycoronene show λ_{max} equal to 355 nm and 352 nm, respectively (Fig. 5A–E). The λ_{max} values show that both attachment of carboxyl groups to coronene (coronene *versus* tricarboxycoronene) and increase in size (from coronene to hexabenzocoronene) lead to red shifts of

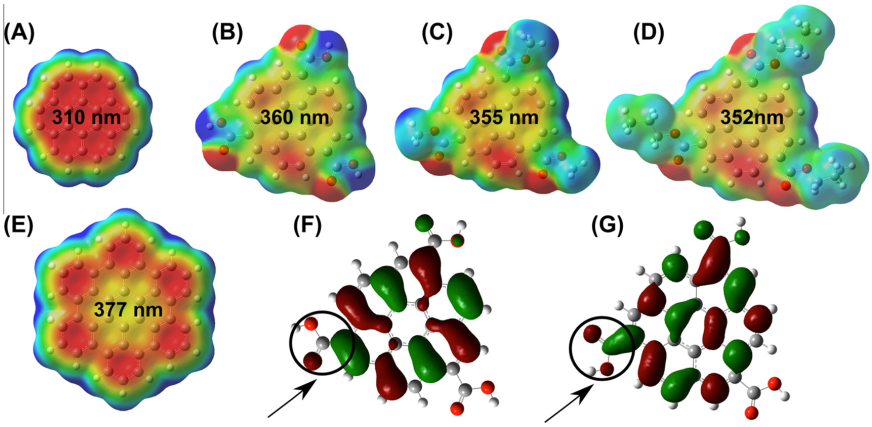

Fig. 5 – Electrostatic maps of (A) coronene, (B) tricarboxycoronene, (C) methyl ester of tricarboxycoronene, (D) propyl ester of tricarboxycoronene, and (E) hexabenzocoronene. Red color represents the most negative charge, green color shows places with neutral charge and blue color represents positive charge. The numbers in the electrostatic maps represent calculated emission maxima (λ_{max}) for these molecules; panels (F) and (G) show localization of HOMO orbitals (F) and LUMO orbitals (G) of tricarboxycoronene. In panels (F) and (G), the circles highlight the transfer of orbitals to carboxylic group after excitation. (A color version of this figure can be viewed online.)

the emission maxima. This is due to an extension of π-conjugated electrons system. In the case of tricarboxycoronene, the highest occupied molecular orbitals (HOMO) are mainly positioned on the coronene core and the lowest unoccupied molecular orbitals (LUMO) span also over the carboxyl groups, which are in conjugation with the coronene π-electrons (Fig. 5F and G). Also, electrostatic potential surfaces show a shift of charge towards the edge upon the addition of carboxyl groups, which can explain more significant electrostatic interactions contribution of the surface carboxyl groups in the PL mechanism. However, carboxyl groups are partially shielded from the edge and solvent in the case of methyl and propyl (and presumably lauryl) esters. Their electrostatic interactions with a solvent are thus weaker than in the case of tricarboxycoronene, which is in a good agreement with the PL measurements. Thus, the change in surface groups has a dramatic effect not only on the size and solubility of the CDs, but also on their optical properties.

4. Conclusions

We described a new synthetic route to control the size and surface chemistry of CDs by using appropriate molecular precursors based on gallate derivatives. CDs with a controllable size are prepared by controlling the alkyl chain on the precursor and can be converted to water-dispersible CDs with surface carboxylate groups exhibiting a record biocompatibility. The differences in PL properties of CDs were examined in detail to explore the roles of their carbogenic core and surface functional groups. Based on the results from steady-state and time-resolved PL measurements, the core-related emission predominates the PL properties of the alkyl chain-terminated CDs while the carboxyl groups influence greatly the PL of the de-esterified CDs acting as emissive surface traps. Supporting theoretical calculations shed some light and provided a basis to understand these effects.

Acknowledgements

The authors acknowledge the support by the Operational Program Research and Development for Innovations – European Regional Development Fund (CZ.1.05/2.1.00/03.0058 of the Ministry of Education, Youth and Sports of the Czech Republic) and Operational Program Education for Competitiveness – European Social Fund (CZ.1.07/2.3.00/20.0155 of the Ministry of Education, Youth and Sports of the Czech Republic). This work was also supported by the Grant Agency of the Czech Republic (P208/12/G016). Financial support from the Internal Student Grants (IGA) of Palacky University in Olomouc, Czech Republic, (PrF_2013_014 and PrF_2013_028) is also gratefully acknowledged. This publication is based on work supported in part by Award No. KUS-C1-018-02, made by King Abdullah University of Science and Technology (KAUST). We also thank A. Fargasova (Regional Centre of Advanced Technologies and Materials, Faculty of Science, Palacky University, Olomouc, Czech Republic) for Raman measurements and Z. Marusak (Regional Centre of Advanced Technologies and Materials, Faculty of Science, Palacky University, Olomouc, Czech Republic) for thermal analysis.

Appendix A. Supplementary data

Supplementary data associated with this article can be found, in the online version, at http://dx.doi.org/10.1016/j.carbon.2014.01.008.

REFERENCES

[1] Xu X, Ray R, Gu Y, Ploehn HJ, Gearheart L, Raker K, et al. Electrophoretic analysis and purification of fluorescent single-walled carbon nanotube fragments. J Am Chem Soc 2004;126:12736–7.

[2] Baker S, Baker G. Luminescent carbon nanodots: emergent nanolights. Angew Chem Int Ed 2010;49:6726–44.

[3] Shen J, Zhu Y, Yang X, Li C. Graphene quantum dots: emergent nanolights for bioimaging, sensors, catalysis and photovoltaic devices. Chem Commun 2012;48:3686–99.

[4] Wang K, Gao Z, Gao G, Wo Y, Wang Y, Shen G, et al. Systematic safety evaluation on photoluminescent carbon dots. Nanoscale Res Lett 2013;8:122–30.

[5] Long Y-M, Zhou C-H, Zhang Z-L, Tian Z-Q, Bao L, Lin Y, et al. Shifting and non-shifting fluorescence emitted by carbon nanodots. J Mater Chem 2012;22:5917–20.

[6] Jin SH, Kim DH, Jun GH, Hong SH, Jeon S. Tuning the photoluminescence of graphene quantum dots through the charge transfer effect of functional. ACS Nano 2013;7:1239–45.

[7] Zhu B, Sun S, Wang Y, Deng S, Qian G, Wang M, et al. Preparation of carbon nanodots from single chain polymeric nanoparticles and theoretical investigation of the photoluminescence mechanism. J Mater Chem C 2013;1:580–6.

[8] Krysmann MJ, Kelarakis A, Dallas P, Giannelis EP. Formation mechanism of carbogenic nanoparticles with dual photoluminescence emission. J Am Chem Soc 2012;134:747–50.

[9] Zhao L, Di F, Wang D, Guo L-H, Yang Y, Wan B, et al. Chemiluminescence of carbon dots under strong alkaline solutions: a novel insight into carbon dot optical properties. Nanoscale 2013;5:2655–8.

[10] Liu F, Jang M-H, Ha HD, Kim J-H, Cho Y-H, Seo TS. Facile synthetic method for pristine graphene quantum dots and graphene oxide quantum dots: origin of blue and green luminescence. Adv Mater 2013;25:3657–62.

[11] Vinci JC, Ferrer IM, Seedhouse SJ, Bourdon AK, Reynard JM, Foster BA, et al. Hidden properties of carbon dots revealed after HPLC fractionation. J Phys Chem Lett 2013;4:239–43.

[12] Liu R, Wu D, Feng X, Müllen K. Bottom-up fabrication of photoluminescent graphene quantum dots with uniform morphology. J Am Chem Soc 2011;133:15221–3.

[13] Lu J, Yang J, Wang J, Lim A, Wang S, Loh KP. One-pot synthesis of fluorescent carbon graphene by the exfoliation of graphite in ionic liquids. ACS Nano 2009;3:2367–75.

[14] Dong Y, Shao J, Chen C, Li H, Wang R, Chi Y, et al. Blue luminescent graphene quantum dots and graphene oxide prepared by tuning the carbonization degree of citric acid. Carbon 2012;50:4738–43.

[15] Gokus T, Nair RR, Bonetti A, Böhmler M, Lombardo A, Novoselov KS, et al. Making graphene luminescent by oxygen plasma treatment. ACS Nano 2009;3:3963–8.

[16] Shen J, Zhu Y, Chen C, Yang X, Li C. Facile preparation and upconversion luminescence of graphene quantum dots. Chem Commun 2011;47:2580–2.

[17] Zhu S, Zhang J, Tang S, Qiao C, Wang L, Wang H, et al. Surface chemistry routes to modulate the photoluminescence of

graphene quantum dots: from fluorescence mechanism to up-conversion bioimaging applications. Adv Funct Mater 2012;22:4732–40.

[18] Hu S, Tian R, Dong Y, Yang J, Liu J, Chang Q. Modulation and effects of surface groups on photoluminescence and photocatalytic activity of carbon dots. Nanoscale 2013. http://dx.doi.org/10.1039/c3nr03893a.

[19] Sun Y-P, Zhou B, Lin Y, Wang W, Fernando KAS, Pathak P, et al. Quantum-sized carbon dots for bright and colorful photoluminescence. J Am Chem Soc 2006;128:7756–7.

[20] Sun Y, Wang S, Li C, Luo P, Tao L, Wei Y, et al. Large scale preparation of graphene quantum dots from graphite with tunable fluorescence properties. Phys Chem Chem Phys 2013;15:9907–13.

[21] Pan D, Zhang J, Li Z, Wu M. Hydrothermal route for cutting graphene sheets into blue-luminescent graphene quantum dots. Adv Mater 2010;22:734–8.

[22] Bourlinos AB, Stassinopoulos A, Anglos D, Zboril R, Karakassides M, Giannelis EP. Surface functionalized carbogenic quantum dots. Small 2008;4:455–8.

[23] Bourlinos AB, Zboril R, Petr J, Bakandritsos A, Krysmann M, Giannelis EP. Luminescent surface quaternized carbon dots. Chem Mater 2012;24:6–8.

[24] Qu S, Wang X, Lu Q, Liu X, Wang L. A biocompatible fluorescent ink based on water-soluble luminescent carbon nanodots. Angew Chem Int Ed 2012;124:12381.

[25] Tang L, Ji R, Cao X, Lin J, Jiang H, Li X, et al. Deep ultraviolet photoluminescence graphene quantum dots. ACS Nano 2012;6:5102–10.

[26] Zhu S, Meng Q, Wang L, Zhang J, Song Y, Jin H, et al. Highly photoluminescent carbon dots for multicolor patterning, sensors, and bioimaging. Angew Chem Int Ed 2013;52:3953–7.

[27] Peng H, Travas-Sejdic J. Simple aqueous solution route to luminescent carbogenic dots from carbohydrates. Chem Mater 2009;21:5563–5.

[28] Fang Y, Guo S, Li D, Zhu C, Ren W, Dong S, et al. Easy synthesis and imaging applications of cross-linked green fluorescent hollow carbon nanoparticles. ACS Nano 2012;6:400–9.

[29] Bao L, Zhang Z-L, Tian Z-Q, Zhang L, Liu C, Lin Y, et al. Electrochemical tuning of luminescent carbon nanodots: from preparation to luminescence mechanism. Adv Mater 2011;23:5801–6.

[30] Yang Y, Wu D, Han S, Hu P, Liu R. Bottom-up fabrication of photoluminescent carbon dots with uniform morphology via a soft-hard template approach. Chem Commun 2013;49:4920–2.

[31] Kubo I, Masuoka N, Xiao P, Haraguchi H. Antioxidant activity of dodecyl gallate. J Agric Food Chem 2002;50:3533–9.

[32] Bourlinos AB, Karakassides Ma, Kouloumpis A, Gournis D, Bakandritsos A, Papagiannouli I, et al. Synthesis, characterization and non-linear optical response of organophilic carbon dots. Carbon 2013;61:640–3.

[33] Frisch MJ, Trucks GW, Schlegel HB, Scuseria GE, Robb MA, Cheeseman JR, et al. Gaussian 09, Revision A 02. Wallingford CT: Gaussian Inc.; 2010.

[34] Runge E, Gross EKU. Density-functional theory for time-dependent systems. Phys Rev Lett 1984;52:997–1000.

[35] Charaf-Eddin A, Planchat A, Mennucci B, Adamo C, Jacquemin D. Choosing a functional for computing absorption and fluorescence band shapes with TD-DFT. J Chem Theory Comput 2013;9:2749–60.

[36] Coates J. Interpretation of infrared spectra, a practical approach. Encyclopedia of analytical chemistry, Chichester: John Wiley & Sons Ltd; 2000. p. 10815–37.

[37] Lindon JC. Encyclopedia of spectroscopy and spectrometry. San Diego: Academic Press; 2000.

[38] Ray SC, Saha A, Jana NR, Sarkar R. Fluorescent carbon nanoparticles: synthesis, characterization, and bioimaging application. J Phys Chem C 2009;113:18546–51.

[39] Yoffe AD. Advances in physics of semiconductor quantum dots and related systems: electronic, optical, luminescence and related properties of low dimensional systems. Adv Phys 2001;50:1–208.

[40] Moriarty P. Nanostructured materials. Rep Prog Phys 2001;64:297–381.

[41] Reimann SM, Manninen M. Electronic structure of quantum dots. Rev Mod Phys 2002;74:1283–342.

[42] Volnianska O, Boguslawski P. Magnetism of solids resulting from spin polarization of p orbitals. J Phys Condens Matter 2010;22:073202.

[43] Lahderanta E, Lashkul AV, Lisunov KG, Zherebtsov DA, Galimov DM, Titkov AN. Magnetic properties of carbon nanoparticles. IOP Conf Ser Mater Sci Eng 2012;38:012010.

[44] Manach C, Williamson G, Morand C, Scalbert A, Rémésy C. Bioavailability and bioefficacy of polyphenols in humans. I. Review of 97 bioavailability studies. Am J Clin Nutr 2005;81:230S–42S.

[45] Orten JM, Kuyper AC, Smith AH. Studies on the toxicity of propyl gallate and of antioxidant mixtures containing propyl gallate. Food Technol 1948;2:308–16.

[46] Bourlinos AB, Bakandritsos A, Kouloumpis A, Gournis D, Krysmann M, Giannelis EP, et al. Gd(III)-doped carbon dots as a dual fluorescent-MRI probe. J Mater Chem 2012;22:23327–30.

[47] Yang S-T, Wang X, Wang H, Lu F, Luo PG, Cao L, et al. Carbon dots as nontoxic and high-performance fluorescence imaging agents. J Phys Chem C 2009;113:18110–4.

[48] Zhang X, Wang S, Zhu C, Liu M, Ji Y, Feng L, et al. Carbon-dots derived from nanodiamond: photoluminescence tunable nanoparticles for cell imaging. J Colloid Interface Sci 2013;397:39–44.

[49] Liu J-H, Anilkumar P, Cao L, Wang X, Yang S-T, Luo PG, et al. Cytotoxicity evaluations of fluorescent carbon nanoparticles. Nano LIFE 2010;01:153–61.

[50] Brus LE. Electron–electron and electron-hole interactions in small semiconductor crystallites: the size dependence of the lowest excited electronic state. J Chem Phys 1984;80:4403–9.

[51] Sykora M, Mangolini L, Schaller R, Kortshagen U, Jurbergs D, Klimov V. Size-dependent intrinsic radiative decay rates of silicon nanocrystals at large confinement energies. Phys Rev Lett 2008;100:067401.

[52] Yu P, Wen X, Toh Y-R, Tang J. Temperature-dependent fluorescence in carbon dots. J Phys Chem C 2012;116:25552–7.

[53] Gaponenko SV. Optical properties of semiconductor nanocrystals. 1st ed. Cambridge: Cambridge University Press; 1998.

[54] Lakowicz JR. Principles of fluorescence spectroscopy. 3rd ed. New York: Springer; 2006.

[55] Marini A, Munoz-Losa A, Biancardi A, Mennucci B. What is solvatochromism? J Phys Chem B 2010;114:17128–35.

B

Carbon dots—Emerging light emitters for bioimaging, cancer therapy and optoelectronics

Nano Today (2014) **9**, 590—603

Available online at www.sciencedirect.com

ScienceDirect

journal homepage: www.elsevier.com/locate/nanotoday

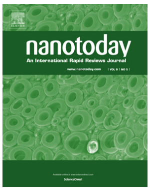

REVIEW

Carbon dots—Emerging light emitters for bioimaging, cancer therapy and optoelectronics

Katerina Hola[a], Yu Zhang[b], Yu Wang[a], Emmanuel P. Giannelis[c], Radek Zboril[a],*, Andrey L. Rogach[b],**

[a] *Regional Centre of Advanced Technologies and Materials, Faculty of Science, Department of Physical Chemistry, Palacky University, Olomouc, Czech Republic*
[b] *Department of Physics and Materials Science and Centre for Functional Photonics, City University of Hong Kong, SAR, Hong Kong*
[c] *Department of Materials Science and Engineering, Cornell University, Ithaca, NY, USA*

Received 27 May 2014; received in revised form 30 June 2014; accepted 1 September 2014
Available online 26 September 2014

KEYWORDS
Carbon dots;
Graphene dots;
Photoluminescence;
Bioimaging;
Light-emitting diodes

Abstract Carbon dots represent an emerging class of fluorescent materials and provide a broad application potential in various fields of biomedicine and optoelectronics. In this review, we introduce various synthetic strategies and basic photoluminescence properties of carbon dots, and then address their advanced *in vitro* and *in vivo* bioapplications including cell imaging, photoacoustic imaging, photodynamic therapy and targeted drug delivery. We further consider the applicability of carbon dots as components of light emitting diodes, which include carbon dot based electroluminescence, optical down-conversion, and hybrid plasmonic devices. The review concludes with an outlook towards future developments of these emerging light-emitting materials.

© 2014 Elsevier Ltd. All rights reserved.

It is already 10 years since a new family of nanomaterials, subsequently denoted as carbon dots (CDs), have been first synthesized and characterized [1]. Since that time, the field of CDs has witnessed an impressive development, in particular focused on the improvement of their light-emitting properties. Terminology-wise, we distinguish between two kinds of these materials, namely few-layer graphene dots (GDs) with lateral dimensions up to 100 nm, which are commonly fabricated from graphene-based precursors [2—4], and quasi-spherical CDs with the typical size under 10 nm in all three dimensions [2,5]. In terms of material composition, the general term ''carbon dot'' is commonly used for fluorescent carbogenic materials with an outer shell composed of carboxylic or other chemical

---

* Corresponding author.
** Corresponding author.
E-mail addresses: radek.zboril@upol.cz (R. Zboril), andrey.rogach@cityu.edu.hk (A.L. Rogach).

http://dx.doi.org/10.1016/j.nantod.2014.09.004
1748-0132/© 2014 Elsevier Ltd. All rights reserved.

functional groups and an inner graphitic core eventually containing covalently bound oxygen and nitrogen atoms. CDs can be easily functionalized to become soluble in water, exhibit robust chemical inertness, including high resistance to photobleaching, and possess better biocompability and lower toxicity as compared to traditional semiconductor quantum dots (QDs) [6,7]. They still suffer from the lower photoluminescence (PL) quantum yields (QY) in the red part of the spectrum; however, progress has been made and this handicap is dramatically being improved [8—10]. In recent years, many synthetic methods have been developed allowing tuning of the optical properties of CDs by controlling the core size and surface chemistry [11—13]. Both synthetic procedures and optical properties of CDs are covered in a number of excellent reviews [2,5,14—16]. This review focuses on the emerging application areas of the fluorescent CDs in biomedicine and optoelectronics. After a short critical survey of synthetic strategies and basic optical properties of CDs, we discuss their applicability in bioimaging, cancer therapy, combined therapy and diagnostics (theranostics), and light emitting diodes.

Synthetic strategies for CDs

CDs and GDs are fluorescent carbon nanomaterials with sp^2 character and a high oxygen content (up to 40%) due to the presence of carbonyl, carboxyl, or epoxy groups [5]. Synthetic procedures towards these materials have witnessed an explosive growth, since the first works reporting the acetic oxidation of a carbon soot that was either prepared by arc-discharge [1], laser ablation [17], or by collecting the soot of a burning candle [18]. They are usually prepared from graphene, other carbon nano-allotropes with sp^2 structures such as coronenes [3], carbon nanotubes [19], or fullerenes [20], or organic molecules that can form graphitic or graphene-like structures during various treatments [2,15]. In general, the synthetic strategies can be classified into top-down or bottom-up approaches. The synthetic strategy and the precursors chosen determine the physicochemical properties of the resulting nanoparticles such as the size, crystallinity, oxygen/nitrogen content, emission characteristics including QY, colloidal stability, and compatibility with a particular solvent.

The top-down synthetic approaches towards CDs and GDs rely on reducing the size of graphite/graphene like structures until the products display the characteristics of fluorescent nanoparticles [2] by oxygen plasma treatment [21], electrochemical oxidation [22], or chemical oxidative cutting/ablation [11]. The first reported synthesis of CDs was performed by a top-down method, namely oxidation of arch-discharge soot using 3.3 N nitric acid [1]. The chemical oxidative ablation is usually performed starting from graphene/graphene oxide, which are refluxed in a mixture of sulphuric and nitric acid, as reported by Pan et al. [23]. The size of the resulting CDs usually varies between 2 and 25 nm [11,24] and their PL QY reaches 28% after the surface passivation with polyethylenglycol [24].

Simply stated, in the bottom-up approaches everything of carbogenic nature that can ''burn'' can produce CDs under suitable conditions. For this reason, CDs have been found in caramel [25] or in Nescafe® coffee [26]. A more convenient synthetic route involves the thermal oxidation of different organic precursors and pioneered by Bourlinos et al., which can directly yield highly fluorescent CDs without any need for surface passivation [27,28], and allows control over the functional groups on the surface [29], the size [13] and the solubility in organic solvents [30]. Thermal oxidation of organic precursors can be also carried out in aqueous solution by heating in a microwave [31,32] or autoclave [33,34], and in the presence of acids [9] producing highly fluorescent CDs. Control over the carbonization conditions through the selection of precursors allows adjustment of the fluorescence color of the resulting CDs (Figure 1a and b) [9,35]. An important feature of the bottom-up syntheses is that they usually do not require surface passivation agents (e.g. polyethylene glycol, polyethylenimine) to obtain fluorescent materials as in the case of top-down synthetic strategies. A brief overview of the preparation routes of CDs and their PL properties is given in Table 1. Interested readers can find more detailed information on these methods in recent reviews [2,15,16]. In hindsight, the preparation routes towards CDs and GDs are simple, do not require expensive precursors, and can easily be up-scaled.

Important characteristic for the applications of CDs is their dominant emission wavelength. In the bottom-up syntheses, the emission wavelength largely depends on the particular synthetic approach, which determines the size, crystallinity, and surface chemistry of the resulting nanoparticles. Wei et al. reported preparation of CDs via Maillard reaction of different amino acids with glucose followed by microwave pyrolysis [35], whose size and the emission wavelength was determined by the type of amino acid used. CDs with an average size of 2.8 nm and with the main emission in the blue region were prepared from tryptophan, green CDs (3.6 nm) from leucin, and yellow (4.5 nm) from aspartic acid (Figure 1a and b). A similar trend was observed by Bhunia et al. who employed hydrothermal carbonization of carbohydrates in the presence of inorganic acids [9]. Blue and green fluorescent CDs were produced by carbonization in the presence of sulfuric acid while carbonization in concentrated phosphoric acid provided particles with bigger size and red-shifted emission maxima.

Within the top-down synthetic approach, the chemical oxidative cutting/ablation from bulk sp^2 materials can also produce CDs/GDs, which luminesce in the yellow-red region. The study by Hens et al. showed that the time of oxidation of various graphite structures in the mixture of H_2SO_4 and HNO_3 (3:1) determines the emission wavelength [36] (Figure 1c). A blue-shift of PL was induced by oxidative size-cutting of the π-electronic structure resulting in increasing quantum confinement. At the same time, the functional groups at the surface of CDs can induce a red-shift of PL [11—13,37]. Wei et al. showed that even the same-size CDs produced by oxidative cutting of graphene nanofibers can exhibit PL from blue to orange determined by different surface charge [38]: CDs were separated by ion exchange chromatography, and particles with the highest negative charge exhibited orange PL while those with the lowest negative charge emitted in the blue region (Figure 1d).

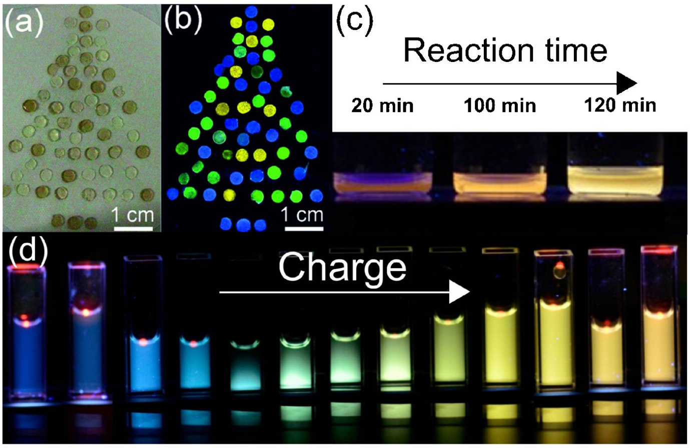

Figure 1 The images of CDs/GDs with red-shifted emission wavelength under UV light. CDs/GDs prepared by (a) microwave pyrolysis of glucose and amino acids immobilized in an agarose gel and positioned into a Christmas tree pattern; (b) the same picture under UV light; (c) oxidative cutting of highly oriented pyrolytic graphite, the time of the reaction determined the emission wavelength; (d) oxidative cutting of graphene nanofibers after ionic chromatography fractionation. Reprinted with permission from [35,36,38]; © 2014 Macmillan Publisher, © 2012 American Chemical Society and © 2014 John Wiley and Sons.

Light emission properties of CDs

CDs are very attractive light emitting materials with a potential to overcome the photobleaching limitations of not only organic dyes and polymer dots but even some semiconductor QDs, as demonstrated in Figure 2, which compares the photostability of those commonly used fluorescent nanomaterials [35]. Recently, the emission of individual GDs has been shown to be free of the blinking and bleaching effects commonly associated with traditional organic dyes and semiconductor QDs [39]. This feature would indeed make GDs very attractive as fluorescent labels, subject to follow-up studies. PL QY of CDs is an important parameter for their potential applications; initially reported values averaged at around 6% [8], but were dramatically improved using appropriate synthetic strategies (Table 1). As already mentioned above, the selection of synthetic methods and precursors play a central role in governing the optical properties of CDs. Thus far, the highest reported room-temperature PL QYs was 53% for oil-soluble CDs prepared by thermal pyrolysis of citric acid as the carbon precursor in hot non-coordinating solvents [8], and 88.6% for water-soluble CDs [40]. The majority of nowadays available CDs and GDs exhibit excitation wavelength-dependent emission with intense emission color in the blue-to-green spectral range (Figure 1). However, by choosing different precursors, excitation wavelength-independent PL of some CDs was also observed, for instance, L-cysteine as precursor providing nitrogen and sulfur as co-dopants has been used to produce deep blue-emitting doped CDs. It was speculated that S dopants strongly suppress excitation-dependent PL originating from O surface states, while N surface states facilitate a high yield of radiative recombination. Moreover, several recent studies reported some strategies and possible precursors on how to achieve stronger PL in yellow [35,37,41] or even in the red region [9,42] as outlined in the previous section. The availability of CDs emitting in the red is particularly important for bioimaging applications, since deep-red and near infra-red (NIR) light exhibit deeper tissue penetration (Figure 3). This is related to yet another useful optical property of CDs, namely up-conversion PL [43]. As such they were reported to undergo multi-photon excitation with large two-photon absorption cross-section for laser excitation at 800—900 nm [43,44]. The excitation in this so-called *biological window* is also connected with deeper tissue penetration (Figure 3) and is particularly important for bioimaging applications. The two-photon absorption cross-section of CDs at different excitation wavelengths was estimated by Cao et al. The typical average value at 800 nm was 39,000 ± 5000 GM (Goeppert—Mayer unit, with 1 GM = 10^{-50} cm^4 s/photon) [43], which is comparable to other two-photon luminescent nanomaterials, (e.g. 780—10,300 GM for CdSe QDs at 800 nm [45] and 47,000 GM for CdSe/ZnS core/shell QDs at 605 nm) [46].

As demonstrated in Figure 4a for organosilane-functionalized carbon dots (Si-CDs) [55], the absorption of CDs in the UV region has three typical features: two absorption bands at 280 nm and 356 nm, respectively, narrow full widths at half maximum at these bands (44 and 58 nm) and broad tail extending over the visible part of the spectrum starting at 470 nm. As was reported in previous studies [56—58], the peak located at 356 nm is ascribed to the presence of the C=O bonds and their n—π^* transition, while the other one at 280 nm is caused by π—π^* transition of the aromatic C=C bond. The broad tail likely originates from other functionalized surface groups of CDs. As already emphasized above, a very remarkable optical property of CDs, which has been intensively examined in recent years [12,13,17,59,60],

Table 1 Representative examples of fluorescent CDs from different preparation methods and their optical properties.

Preparation method	Precursors[a]	Reaction conditions	Constituting elements	Emission properties[b]	Emission color	PL QY (%)	Ref.
Arc-discharge	Carbon soot	HNO_3, boiled, 48 h	C, O, N, H	SDPL	Blue, yellow	1.6%	[1]
Laser ablation	Carbon soot	PEG_{1500N}, 120 °C, 72 h	C, O, N, H	EDPL	Full-color	4–10%	[17]
Combustion candle	Soot	HNO_3, refluxed, 12 h	C, O, N, H	Unclear	Full-color	0.8–1.9%	[18]
Electrooxidation	Graphite	NaH_2PO_4 electrolyte	C, O	EIDPL	Blue, yellow	1.2%	[22]
Thermal oxidation	CA, $H_2N(CH_2)_{10}COONa$	300 °C, air, 2 h	C, O, N, H, Na	EDPL	Full-color	3%	[27]
Supported synthesis	F127, Resol	900 °C, Ar, 2 h	C, O, N, H	EDPL	Violet to yellow	11–15%	[47]
Microwave pyrolysis	Saccharide, PEG	500 W, 2-10 min	C, O	EDPL	Blue to green	3.1–6.3%	[31]
	Glucose, amino acids	two steps: 125 °C, 30 min and 275 °C, 5 min	C, O, N,	EDPL, EIDPL	Blue, green yellow	30–69%	[35]
Ultrasonic synthesis	Glucose	HCl or NaOH, 4 h	C, O,H	EDPL, UC	Full-color	7%	[48]
Thermal pyrolysis	CA, ODE, HDA	300 °C, Ar, 3 h	C, O, N, H	EDPL	Full-color	53%	[8]
	CA, EA	180 °C, 230 °C, 300 °C	C, O, N, H	EDPL	Full-color	50%	[49]
	CA, DETA	170 °C, air, 30 min	C, O, N, H	EDPL	Blue to yellow	88.6%	[40]
Hydrothermal synthesis	CA, EDA	150 °C, 200 °C, 250 °C, 300 °C, 5 h	C, O, N, H	EDPL	Full-color	80.6%	[50]
	CA, L-cysteine	200 °C, 3 h	C, O, N, S, H	EIDPL	Deep blue	73%	[51]
	Sodium citrate, NH_4HCO_3	180 °C, 4 h	C, O, N, Na	EIDPL	Blue	68%	[33]
	CA, EDA	160 °C, 4 h	C, O, N	EIDPL	Blue	94%	[52]
Chemical method	Carbohydrate	80–300 °C, 5–60 min	C, O, N, H	EDPL	Full-color	6–30%	[9]

[a] CA = citric acid, PEG = poly(ethylene glycol), ODE = octadecene, HDA = 1-hexadecylamine, EA = ethanolamine, DETA = diethylenetriamine, EDA = ethylenediamine.

[b] SDPL = size-dependent PL, EDPL = excitation-dependent PL, EIDPL = excitation-independent PL, UC = upconversion.

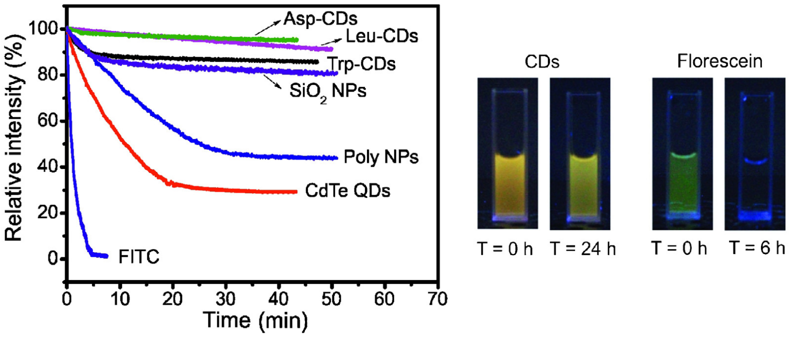

Figure 2 The photostability of emission of CDs derived from various precursors (Trp: tryptophan; Leu: leucin, Asp: aspartic acid) compared with fluorescein isothiocyanate (FITC) and other fluorescent nanoparticles including CdTe QDs, dye-doped SiO_2 nanoparticles (SiO_2 NPs) and dye-doped polymer nanoparticles (Poly NPs). The images on the right show solutions of CDs and fluorescein after UV-light irradiation for different times. Reprinted with permission from [35,53]; © 2011 John Wiley and Sons; © 2014 Macmillan Publishers Limited.

is their excitation wavelength-dependent emission, both in terms of the dominant emission maximum (Figure 4b) and the emission intensity profile, which peaks in the blue-green spectral range (Figure 4c). It is often assigned to the fact that the prepared material is a mixture of particles with different sizes as well as particles containing different edge defects/emissive traps on the surface [5]. Adding credence to this hypothesis, excitation wavelength-dependent emission was not observed when narrow size distribution CD materials [35] or samples with lower amount of oxygen surface states [59] were tested. It has been reported that the wavelength of the dominating emission peak is driven by the graphitic core size (whose good crystallinity is an important requirement) [61], and thus by its suitable quantum confinement similarly to traditional semiconductor QD systems. This was demonstrated by the recent synthetic routes enabling fabrication of CDs with PL color ranging from blue to yellow and red [9,35]. CDs with PL in the yellow or red region were significantly larger than the blue-emitting particles. The important role of the core size was also illustrated

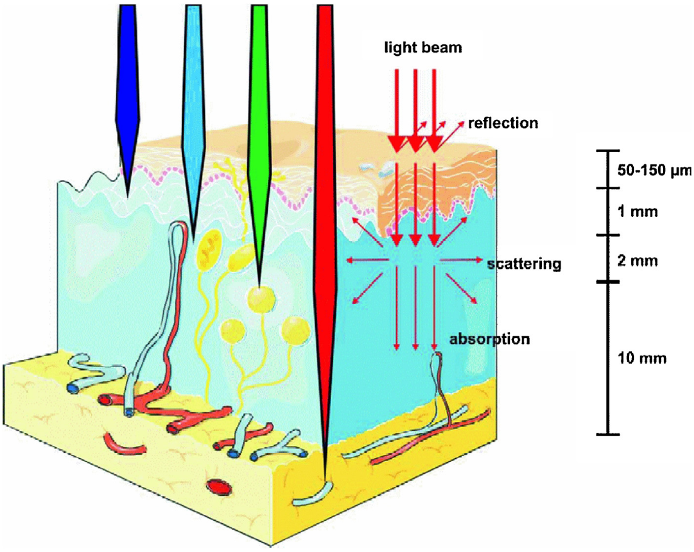

Figure 3 The visualization of light penetration through the tissues according to its wavelength. Reprinted with permission from [54]; © 2011 American Cancer Society.

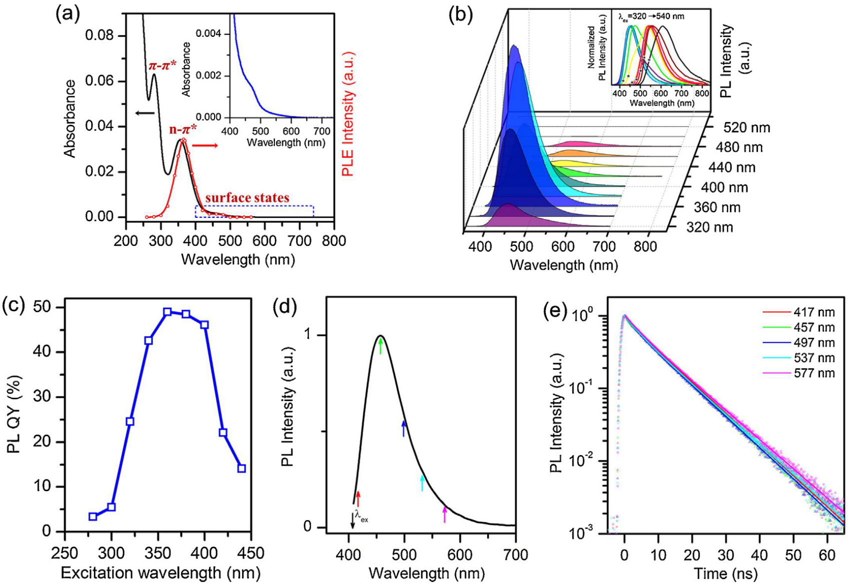

Figure 4 Optical properties of the CDs. (a) Typical absorption (black) and excitation spectra (red) of CDs; the inset shows an enlarged absorption spectrum. (b) PL spectra recorded at different excitations wavelengths in 20 nm increments; the inset represents normalized PL spectra at the corresponding excitation wavelengths. (c) Excitation wavelength dependent PL QY. (d) Photoluminescence spectrum of CDs (405 nm excitation wavelength). (e) PL decay curves of CDs at 405 nm excitation detected at different emission wavelengths shown in panel (d). Adapted with permission from [55] © 2014 American Chemical Society.

by DFT calculations [62]: an increase in the particle size and aromatic rings conjugation causes a decrease in the $\pi-\pi^*$ transition bandgap. At the same time, the surface functional groups of CDs, which are directly linked and conjugated to the graphitic core, can also dramatically affect their PL properties. According to DFT calculations, carboxylic groups or amino groups bound to the surface of CDs can decrease the bandgap of the resulting nanoparticles [11,13]. As a consequence, different surface functional groups can shift the PL emission [11,37], enlarge the excitation wavelength range [11] and cause the excitation wavelength-dependent emission. However, the role of surface groups is still debated with ongoing and systematic investigations to fully understand these phenomena. The representative PL decay curves of CDs, measured at a range of excitation wavelength as illustrated in Figure 4d are given in Figure 4e. The mean value of radiative lifetimes is in the range of 9.6—10.2 ns for all of the emission wavelengths, making it different to distinguish the surface state emission from the emission from levels associated with the $n-\pi^*$ transitions such as presented in Figure 4a. Femtosecond time-resolved spectroscopy and Fourier transform infrared spectroscopy were recently combined to explore the common PL origin in CDs and GDs and identify the functional surface groups responsible for the fluorescence mechanisms in these carbon nanomaterials [63]. The competition among different emission centers and traps were found to dominate their optical properties, which include carboxyl groups, carbonyl groups, and several edge carbon atoms of the carbon backbone.

Bioapplications of CDs

One of the most promising and very often emphasized applications of CDs is in biomedical imaging. These fluorescent materials offer a useful platform for exploring the challenges in the field of nanomedicine, in particular in diagnosis and in cancer therapy. It has been already shown that CDs fulfill the two critical criteria for clinical use [64]: they can be rapidly excreted from the body [65] and exhibit low toxicity while producing reliable optical signal. Furthermore, CDs have been used as photoacoustic contrast agents [66], as photosensitizers for photodynamic therapy [67] and for photothermal therapy [68]. The large surface area of CDs and the availability of carboxylic functional groups on the surface allow for preparation of multimodal probes and therapeutic conjugates. The broad portfolio of promising bioapplications of CDs and GDs is summarized in Figure 5.

In vitro studies—cell labeling with CDs

Similar to traditional semiconductor QDs, CDs offer unique properties favorable in cell imaging or long term cell tracking: contrary to fluorescent dyes they do not suffer from narrow excitation band and fast photobleaching [5,69]. Another crucial prerequisite for cell imaging, in addition to the suitable optical properties, is their low cytotoxicity. There have been many *in vitro* studies reporting biocompatibility of CDs, which exhibit very low or no cytotoxicity

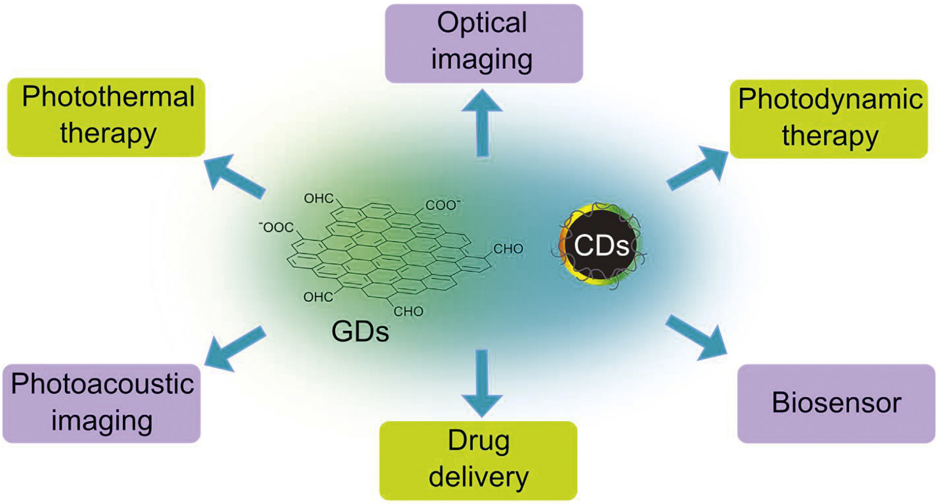

Figure 5 The major promising bioapplication areas of GDs and CDs.

even in much higher concentrations than needed for fluorescent cell imaging [5,70]. As an example, Ding et al. reported CDs which did not reach LC_{50} with a concentration of 5 mg mL^{-1} after 24 h labeling of HeLa cells [71], while the concentration necessary for cell imaging studies is more than a hundred times lower [72]. In comparison, semiconductor QDs exhibit cytotoxic effects in much lower concentrations varying from 62.5 μg mL^{-1} to 400 μg mL^{-1} depending on the type, size or biocompatible shell and the type of the tested cell lines [73].

Another parameter important for the optical cell tracking or monitoring of biological processes is cell uptake of the particular material. For nanoparticles in general, cell uptake depends on the size, surface charge, and surface chemistry all of which play a crucial role in biosensing, cell labeling, intracellular delivery as well as in *in vivo* imaging [69]. Recent studies demonstrated that CDs are mostly internalized in the cytoplasm, especially in endosomes/lysosomes, but also in mitochondria or endoplasmic reticulum (Figure 6) [74—78]. The sufficient incubation time for cell imaging was only 2 h or less and it seems that CDs enter the cells by non-endocytic pathways [78], which is probably caused by their very low size and hydrophilic nature. Very few studies reported the presence of CDs around the cell membrane [79], and there is only one study reporting the presence of CDs (strongly positively charged) in the cell nucleus [80]. In comparison, QDs are very often nonspecifically adsorbed onto the cell membrane due to the hydrophobic interactions, which had to be overcome by altering their surface coverage, by nano-injection or electroporation [69].

In vivo studies—biodistribution of CDs

The criteria for using nanomaterials for *in vivo* diagnostics and targeted therapy are more challenging than those for cell labeling. Important parameters, in addition to the low toxicity and sufficient cell uptake, are hemocompatibility, small hydrodynamic diameter, low nonspecific protein adsorption and rapid extraction from the body with sufficient delivery to the targeted (usually cancer) tissue [81]. The fastest and most preferred excretion from the body is renal filtration [82]; excretion through the liver into the bile is slow, inefficient and connected with toxic risks [82]. The way to decrease the uptake of CDs by the liver and spleen and to maximize their excretion into urine is to use particles with sizes ranging between 4 and 8 nm and possessing a neutral surface charge [81]. The size is important because only the nanoparticles with hydrodynamic diameter smaller than 5.5 nm (as was estimated for the case of QDs [82]) are able to pass through the glomerular filtration. The neutral surface charge prevents adsorption of plasma proteins, which would increase their hydrodynamic diameter [81]. Moreover, this unwanted adsorption can lead to enhanced uptake by phagocytic cells, decreasing availability of CDs for the targeted application and increasing their retention in the liver or spleen [81].

To date, several *in vivo* tests of the biodistribution of CDs have been performed [53,65,78,83—87]. These studies can be divided into two groups depending if the nanoparticles were decorated with polyethylene glycol (PEG) or not. In the first case, the CDs (<5 nm) were fast excreted into the urine and showed extremely low accumulation in the liver (Figure 7) [65,83]. Furthermore, Huang et al. reported significant accumulation of PEGylated CDs in tumor regions [65]. In the second case, GDs (<5 nm), which were used without surface coverage showed significant accumulation in liver, lung, or bones [53,86]. These studies provide strong evidence that the neutral surface coverage by PEG plays a crucial role in the body's ability to clear nanoparticles of a certain size, which has to be taken into account for further theranostic applications of CDs. We note that CdSe QDs can

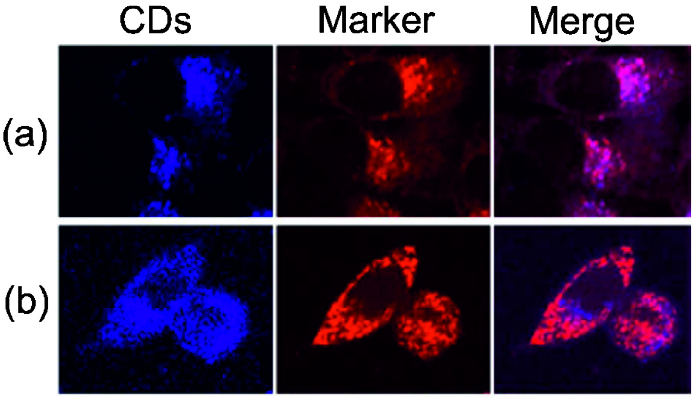

Figure 6 *In vitro* distribution of CDs in Hela cells after 1 h incubation. The cells were afterwards incubated with lysosomal/endosomal marker (a) and mitochondrial marker (b). The merged images demonstrate localization of CDs mainly in lysosomal/endosomal compartments, but also their co-localization in mitochondria. Reprinted with permission from [78]; © 2012 Springer.

also be excreted through the renal filtration system [82], and the pathway of the excretion is crucially related to their size: particles with hydrodynamic diameter of 4.6 nm were excreted mainly in the urine, while bigger particles (7.2 nm) were mainly accumulated in reticuloendothelial organs (liver and spleen). The accumulation of heavy metals in these organs, as it was reported in a recent preclinical study, is really problematic [88]. The difference between the toxicity of QDs and CDs is also apparent from the comparison of acute toxicity in living mice. Bao et al. reported LD50 for the injected dose of 16.2 mg of CdSe/CdS QDs per kg of body weight of Kunming mice within 24 h [89]. The death ratio for the injected dose of 26 mg/kg was 60% and for 40 mg/kg it reached 100% [89]. Residues of the QDs were found in the kidneys and intestinal tract after 14 days of injection [89]. In a similar study by Wang et al.,

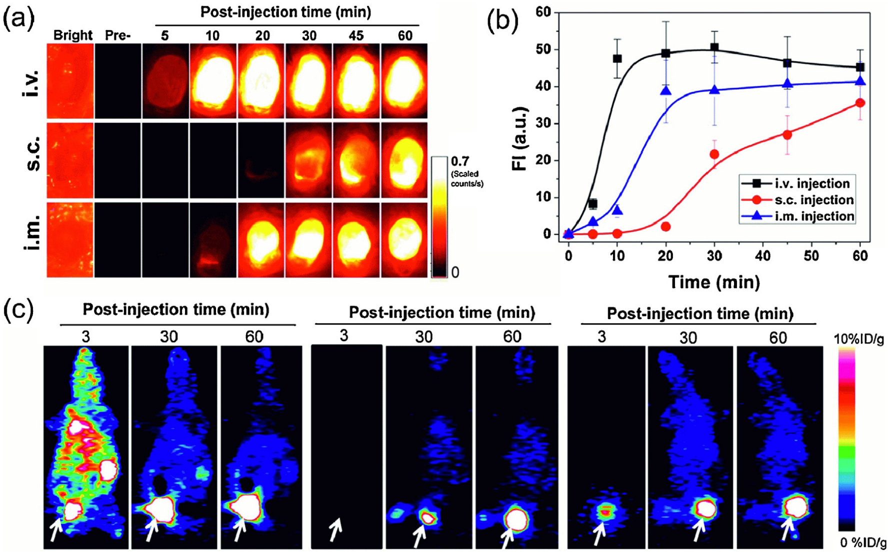

Figure 7 The visualization of renal clearance of PEGylated CDs from the body of mice. (a) Optical images of bladder after different ways of injection (i.v.—intravenous, s.c.—subcutaneous, i.m.—intramuscular). (b) The intensity of the signal in the bladder as a function of time. (c) The visualization of ^{64}Cu—CDs conjugate biodistribution by PET demonstrating the accumulation of CDs in the bladder (white arrow) after various post-injection time. Reprinted with permission from [65]; © 2013 American Chemical Society.

there were no signs of mortality even with extremely high doses of CDs (51 mg/kg, BALB/c mice) [7]. Furthermore, no sub-acute toxicity and no differences in the biochemical and hematological markers in comparison with the control mice after 28 days, since injection, were observed [7].

Advanced bioapplications of CDs in photoacustic imaging and anticancer therapy

A particularly attractive bioapplication of CDs is their use as contrast agents in photoacoustic imaging. This diagnostic technique is based on the fact that some materials — such as CDs — can generate detectable acoustic waves after laser irradiation [90]. It offers excellent spatial resolution and can provide valuable information even in the smallest areas, e.g. for the detection of axillary lymph nodes where cancer cells can be spread in the course of breast cancer. Wu et al. reported application of CDs for photoacoustic visualization of the sentinel lymph nodes and vessels [66]. As can be seen in Figure 8a, CDs exhibited rapid signal enhancement after injection and were removed relatively fast from the vessels.

Moreover, CDs can be used as a therapeutic agent. Markovic et al. [67] and Christensen et al. [91] applied them as *in vitro* photosensitizers allowing generation of reactive oxygen species (ROS) in tumor cells (Figure 8b). However, blue light used in these studies can hardly penetrate through the tissue, as illustrated in Figure 3. For exploring the full potential of ROS generation *in vivo* and the targeted treatment by CDs, two-photon excitation in the biological window can be applied, that seems to be sufficient for optical cell imaging through 1.8 mm thick phantom tissue [92]. Alternatively, it can be accomplished by tuning the PL of CDs into the deep red region of the spectrum.

Yet another important therapeutic tool offered by CDs is their ability to serve as a nanocarrier for drug delivery. In addition to their sufficient uptake at solid tumor sites [65] they may be able to deliver drugs to the targeted tumor locations. Importantly, CDs can be conjugated with various compounds for active targeting. Tang et al. reported loading of the anticancer drug doxorubicin labeled by red fluorescent dye into PEG chains on the surface of green fluorescent CDs [93] (Figure 8c). This conjugate exhibited time dependent sustained doxorubicin release at acidic pH levels, simulating lysosomal uptake in cells of a cancerous tissue. Furthermore, the release could be monitored by optical imaging using Förster resonance energy transfer (FRET) between CDs and doxorubicin. Similarly, oxaliplatin was conjugated with CDs and the prepared hybrid system was successfully tested as a theranostic agent *in vivo* [94]. Important feature of CDs in these types of drug delivery systems is their ability to be quickly removed from the body through the kidneys after drug delivery.

CD-based optoelectronics

Both QDs and CDs are increasingly gaining momentum as materials for light emitting diodes (LEDs). The technology for lighting and displays based on organic light emitting diodes (OLEDs) has been a dominant topic of academic research over the past three decades and is now approaching industrial applications. Quantum dots-based light emitting diodes (QD-LEDs) have already emerged as a competitive choice [95,96], largely due to the ease of solution processability and compatibility with low cost OLED techniques [97]. LED integration of inorganic semiconductor nanocrystals, with their symmetrical and narrow emission, broad absorption, high PL QYs, and high resistance to photo-oxidation for core-shell QDs can overcome the issues of the quality of color emission and limited device lifespan of OLEDs [98].

The first QD-based electroluminescent (EL) device with spin-coated poly-(phenylene vinylene) polymer as a hole

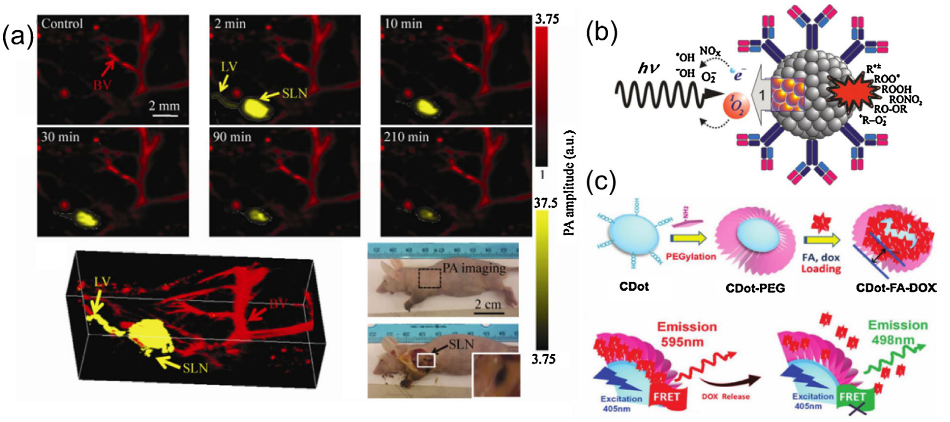

Figure 8 Advanced theranostic applications of CDs: (a) photoacoustic imaging of the sentinel lymph nodes (SLN) and the vessels (LV); (b) ROS generation by CDs after light irradiation; (c) drug delivery system based on CDs and doxorubicin (DOX) for real-time FRET monitoring of drug release. Reprinted with permissions from [66,91,93]. © 2013 Springer; © 2011 American Scientific Publishers; © 2013 John Wiley and Sons.

transport layer and a multilayer film of CdSe nanocrystals as an emitting as well as electron transport layer was demonstrated in 1994 by Colvin et al., with an external quantum efficiency of only 0.01% [99]. As a result of the subsequent development, devices combining an organic hole transport layer and an inorganic metal oxide electron transport layer with emissive QD films showed maximum luminance and power efficiency values over 4200 cd/m^2 and 0.17 lm/W for blue emission, 68,000 cd/m^2 and 8.2 lm/W for green emission, and 31,000 cd/m^2 and 3.8 lm/W for red emission [100,101].

As promising as the solution-processed QD-LEDs are, a serious drawback of the present colloidal QD-LED technology is its reliance on heavy-metal based QDs, still dominated by use of cadmium and lead chalcogenides [102,103]. The reservations in regulatory acceptance of these heavy-metal constituents could potentially hinder the ultimate transition from academic research to commercialization of the QD-LED technology. Toward this end, intensive research studies have been recently performed towards development of QD-LEDs based on cadmium-free compositions [104—106]. At the same time, CDs started to emerge as a non-toxic alternative for applications in displays and solid state lighting [8]. It is useful to distinguish between two types of LEDs using CDs, which rely on two different means of excitation. One is based on electrically exciting the CDs, resulting in LEDs based on the direct electroluminescence (EL) of CDs, and the other is through their optical excitation, which results in color-conversion LEDs using CDs as the nanophosphor component.

CD-based electroluminescent devices

The first electrically driven CD-LED reported by Wang et al. in 2011 [107] used a layered architecture illustrated in Figure 9a and was based on an emissive layer of CDs passivated with 1-hexadecylamine which was sandwiched between a poly(ethylenedioxythiophene):polystyrene sulphonate (PEDOT:PSS) hole injection layer and a 1,3,5-tris(N-phenylbenzimidazol-2-yl) benzene (TPBI) electron transport layer. A maximum external quantum efficiency of 0.083% at a current density of 5 mA/cm^{-2} with a maximum brightness of 35 cd/m^2 was achieved. In 2013, Zhang et al. reported multi-color EL from CDs of the same size. The device consisted of a patterned ITO anode, a 25 nm thick PEDOT:PSS hole injection layer, a 40 nm poly(N,N′-bis(4-butylphenyl)-N,N′-bis(phenyl) benzidine) hole transport layer, a 20 nm CD emissive layer, a 5 nm TPBI electron transport layer, and a cathode composed of a 1 nm LiF and 150 nm aluminum double layer [108]. The blue, cyan, magenta, and white EL emissions could be obtained from the same CD-LEDs operated at different driving voltages, as illustrated in Figure 9b. The maximum brightness of the devices was 24 cd/m^2 and 90 cd/m^2 for blue and white light, respectively. Compared with the first generation QD-LEDs showing relatively low external quantum efficiency (EQE, 0.01%), CD-LEDs have already shown an acceptable brightness and EQE (>0.08%), paving the way towards high quality CDs-based light sources. The performance of the CD-LEDs is expected to be further improved as details of the underlying physical mechanisms of the recombination and charge injection pathways involving CDs emerge from forthcoming studies. Proper choices of energy matched carrier injection layers, suitable ligands enhancing the overall conductivity of CD active layers, and embedding of CDs in a suitable conducting matrix able to keep their high quantum yield will allow us to improve the efficiency of CD EL.

Optical down-conversion CD-based devices

High PL QY and bright blue emission of CDs render them promising component for white LEDs based on the optical down-conversion. The first demonstration of optical down-conversion with CDs using a UV-LED chip is shown in Figure 10a. A 370 nm excitation light source was employed to excite CDs with a PL QY of 47% encased in a superglue. Devices providing bright blue, orange, and warm white colors, when the average size of the particles changed from 2.4 to 3.5 and 4.5 nm, respectively, were obtained [10]. More recently, in order to further improve the color temperature

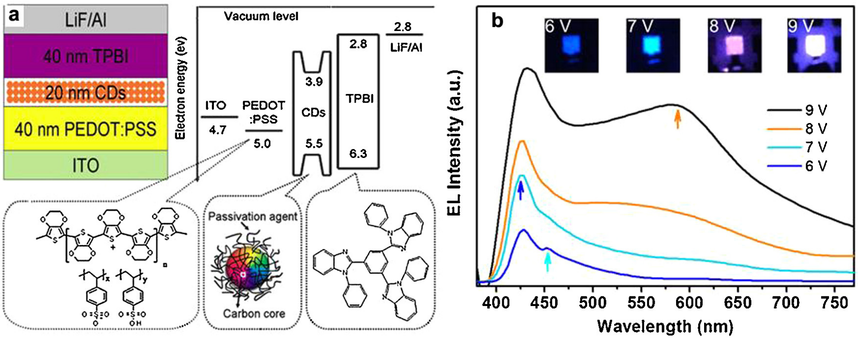

Figure 9 (a) Schematic diagrams of the CD-LED and (b) EL spectra of CDs for different driving voltages with true color photographs of blue, cyan, magenta, and white emitting CD-LEDs shown in inset. Reprinted with permission from [107,108]; © 2011 Royal Chemical Society; © 2013 American Scientific Publishers.

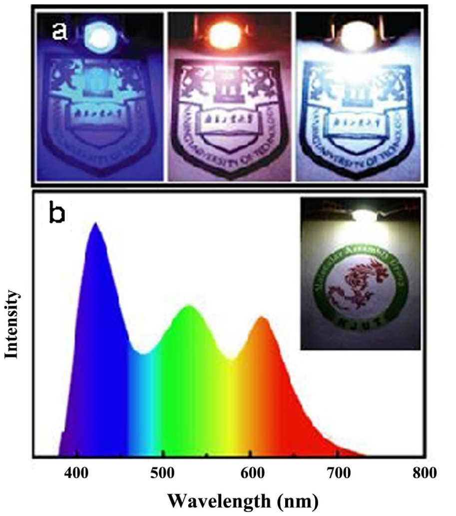

Figure 10 (a) True-color photographs of down-conversion CD-based LED devices with bright blue, orange, and white light. (b) The emission spectrum of the white LED incorporating blue-emitting CDs combined with green and red emitting semiconductor QDs, inset: photograph of the LED device in the dark. Reprinted with permission from [10,109]; © 2012 The Royal Society of Chemistry; © 2013 American Chemical Society.

of CD-based white LEDs, Li et al. fabricated white LEDs by depositing a mixture of CDs with blue emission and two different sizes of CdTe QDs with the green and red emissions in a silicone matrix on a UV—LED chip [109]. The resultant three-band blue—green—red LED (Figure 10b) emitted white light with a color rendering index (CRI) up to 87, indicating that incorporation of CDs together with semiconductor QDs can be a promising solution for white light sources with high CRI. This approach constitutes an effective method to improve the weak yellow/red emission of CD-based optical down-conversion devices through combination of these efficient blue emitters with other luminophores such as QDs. We recently extended this concept towards realization of CD-based white LEDs with a high CRI of 93 by combining low toxic green and red emitting ZnCuInS core/shell QDs with bright blue emitting CDs [110].

Metal-decorated CDs in plasmonic optoelectronic devices

Recent research efforts have been extended to produce CDs with controlled surface properties, allowing the realization of photoinduced electron transfer at the interfaces. Choi et al. [111] employed CDs as a reducing agent and template to prepare CD-supported silver nanoparticles. The electron-donating capability of photoexcited CDs enables to decorate their surface with clustered silver nanoparticles, which results in an improved light-harvesting ability of these hybrid nanoparticles. These new materials have been employed to improve the performance of plasmonic polymer LEDs (with the highest luminous efficiency of 18.54 lm W^{-1} reported up to date) and polymer solar cells as presented in Figure 11.

Summary and outlook

Recently emerged CDs and GDs offer a number of attractive optical characteristics similar to the traditional semiconductor QDs based on metal chalocogenides, while at the same time providing added benefits due to their better biocompatibility and fast renal clearance. Following initial reports on this new kind of fluorophores, which concentrated mostly on the synthesis and photophysics-related studies, considerable progress has been made in applications of CDs in bioimaging, photoacustic imaging, photodynamic therapy, and targeted drug delivery. The key challenge for most of these applications is to improve the PL QY of CDs in the deep-red and near infrared region, where new synthetic strategies are still under intensive development. In respect

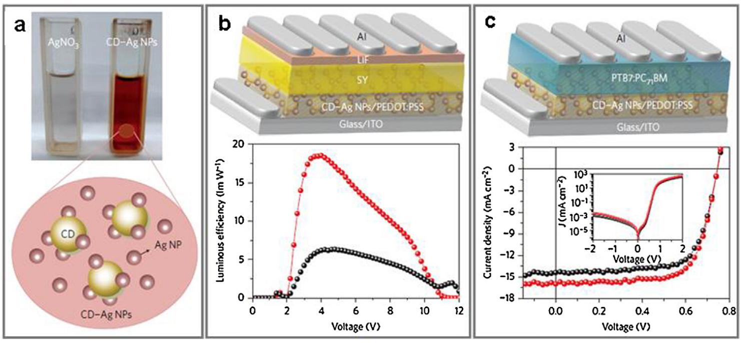

Figure 11 (a) Photographs and schematic illustration of CD-supported silver nanoparticles. (b) Device structure and luminous efficiency of polymer LEDs incorporating CD-supported silver nanoparticles. (c) Device structure and I-V characteristics of CD-supported silver nanoparticles-based polymer solar cells. Reprinted with permission from [111]; © 2013 Nature Publishing Group.

to the optoelectronics application of CDs, the performance of the CD-based LEDs is expected to be further improved with better understanding related to the underlying physical mechanism of the excitation-tunable CD emission. There are two key challenges facing the electrical excitation of CDs: energy level matching and QD luminescence quenching in the solid state and thin films, which we anticipate to be the subject of increasing research attention in the years to come. Finally, the ability of properly functionalized CDs to promote photoinduced electron transfer at the interface allows for fabrication of hybrid materials with a variety of useful functions, such as plasmonic enhancement elements for metal decorated CDs employed in optoelectronic devices.

Acknowledgments

This work was supported by the Operational Program ''Research and Development for Innovations—European Regional Development Fund'' (CZ.1.05/2.1.00/03.0058 of the Ministry of Education, Youth and Sports of the Czech Republic), the Operational Program ''Education for Competitiveness—European Social Fund'' (CZ.1.07/2.3.00/20.0155 of the Ministry of Education, Youth and Sports of the Czech Republic), the project P208/12/G016 by Czech Science Foundation, the Student Project IGA_PrF_2014023 of Palacky University, the Award No. KUS-C1-018-02, made by the King Abdullah University of Science and Technology (KAUST), and the Research Grant Council of Hong Kong S.A.R. (T23-713/11).

References

[1] X. Xu, R. Ray, Y. Gu, H.J. Ploehn, L. Gearheart, K. Raker, W.A. Scrivens, J. Am. Chem. Soc. 126 (2004) 12736.

[2] L. Li, G. Wu, G. Yang, J. Peng, J. Zhao, J.-J. Zhu, Nanoscale 5 (2013) 4015.

[3] R. Liu, D. Wu, X. Feng, K. Müllen, J. Am. Chem. Soc. 133 (2011) 15221.

[4] J. Lu, J. Yang, J. Wang, A. Lim, S. Wang, K.P. Loh, ACS Nano 3 (2009) 2367.

[5] S. Baker, G. Baker, Angew. Chem. Int. Ed. 49 (2010) 6726.

[6] B. Han, W. Wang, H. Wu, F. Fang, N. Wang, X. Zhang, S. Xu, Colloid Surf. B—Biointerfaces 100 (2012) 209.

[7] K. Wang, Z. Gao, G. Gao, Y. Wo, Y. Wang, G. Shen, D. Cui, Nanoscale Res. Lett. 8 (2013) 122.

[8] F. Wang, S. Pang, L. Wang, Q. Li, M. Kreiter, C. Liu, Chem. Mater. 22 (2010) 4528.

[9] S.K. Bhunia, A. Saha, A.R. Maity, S.C. Ray, N.R. Jana, Sci. Rep. 3 (2013) 1473.

[10] X. Guo, C.-F. Wang, Z.-Y. Yu, L. Chen, S. Chen, Chem. Commun. 48 (2012) 2692.

[11] S.H. Jin, D.H. Kim, G.H. Jun, S.H. Hong, S. Jeon, ACS Nano 7 (2013) 1239.

[12] S. Zhu, J. Zhang, S. Tang, C. Qiao, L. Wang, H. Wang, X. Liu, B. Li, Y. Li, W. Yu, X. Wang, H. Sun, B. Yang, Adv. Funct. Mater. 22 (2012) 4732.

[13] K. Hola, A.B. Bourlinos, O. Kozak, K. Berka, K.M. Siskova, M. Havrdova, J. Tucek, K. Safarova, M. Otyepka, E.P. Giannelis, R. Zboril, Carbon 70 (2014) 279.

[14] S. Zhu, S. Tang, J. Zhang, B. Yang, Chem. Commun. 48 (2012) 4527.

[15] J. Shen, Y. Zhu, X. Yang, C. Li, Chem. Commun. 48 (2012) 3686.

[16] M. Bacon, S.J. Bradley, T. Nann, Part. Part. Syst. Charact. 31 (2013) 415.

[17] Y.-P. Sun, B. Zhou, Y. Lin, W. Wang, K.A.S. Fernando, P. Pathak, M.J. Meziani, B.a. Harruff, X. Wang, H. Wang, P.G. Luo, H. Yang, M.E. Kose, B. Chen, L.M. Veca, S.-Y. Xie, J. Am. Chem. Soc. 128 (2006) 7756.

[18] H. Liu, T. Ye, C. Mao, Angew. Chem. Int. Ed. 46 (2007) 6473.

[19] D.V. Kosynkin, A.L. Higginbotham, A. Sinitskii, J.R. Lomeda, A. Dimiev, B.K. Price, J.M. Tour, Nature 458 (2009) 872.

[20] J. Lu, P.S.E. Yeo, C.K. Gan, P. Wu, K.P. Loh, Nat. Nanotechnol. 6 (2011) 247.

[21] T. Gokus, R.R. Nair, A. Bonetti, M. Böhmler, A. Lombardo, K.S. Novoselov, A.K. Geim, A.C. Ferrari, A. Hartschuh, ACS Nano 3 (2009) 3963.

[22] Q.-L. Zhao, Z.-L. Zhang, B.-H. Huang, J. Peng, M. Zhang, D.-W. Pang, Chem. Commun. 41 (2008) 5116.

[23] D. Pan, J. Zhang, Z. Li, M. Wu, Adv. Mater. 22 (2010) 734.

[24] J. Shen, Y. Zhu, X. Yang, J. Zong, J. Zhang, C. Li, New J. Chem. 36 (2012) 97.

[25] M.P. Sk, A. Jaiswal, A. Paul, S.S. Ghosh, A. Chattopadhyay, Sci. Rep. 2 (2012) 383.

[26] C. Jiang, H. Wu, X. Song, X. Ma, J. Wang, M. Tan, Talanta 127 (2014) 68.

[27] A.B. Bourlinos, A. Stassinopoulos, D. Anglos, R. Zboril, V. Georgakilas, E.P. Giannelis, Chem. Mater. 20 (2008) 4539.

[28] A.B. Bourlinos, A. Stassinopoulos, D. Anglos, R. Zboril, M. Karakassides, E.P. Giannelis, Small 4 (2008) 455.

[29] A.B. Bourlinos, R. Zboril, J. Petr, A. Bakandritsos, M. Krysmann, E.P. Giannelis, Chem. Mater. 24 (2012) 6.

[30] O. Kozak, K.K.R. Datta, M. Greplova, V. Ranc, J. Kaslik, R. Zboril, J. Phys. Chem. C 117 (2013) 24991.

[31] H. Zhu, X. Wang, Y. Li, Z. Wang, F. Yang, X. Yang, Chem. Commun. 34 (2009) 5118.

[32] S. Qu, X. Wang, Q. Lu, X. Liu, L. Wang, Angew. Chem. Int. Ed. 51 (2012) 12215.

[33] Y. Guo, Z. Wang, H. Shao, X. Jiang, Carbon 52 (2013) 583.

[34] C.X. Guo, J. Xie, B. Wang, X. Zheng, H. Bin Yang, C.M. Li, Sci. Rep. 3 (2013) 2957.

[35] W. Wei, C. Xu, L. Wu, J. Wang, J. Ren, X. Qu, Sci. Rep. 4 (2014) 3564.

[36] S.C. Hens, W.G. Lawrence, A.S. Kumbhar, O. Shenderova, J. Phys. Chem. C 116 (2012) 20015.

[37] H. Tetsuka, R. Asahi, A. Nagoya, K. Okamoto, I. Tajima, R. Ohta, A. Okamoto, Adv. Mater. 24 (2012) 5333.

[38] J. Wei, J. Qiu, Adv. Eng. Mater. (2014), http://dx.doi.org/10.1002/adem.201400146.

[39] Q. Xu, Q. Zhou, Z. Hua, Q. Xue, C. Zhang, X. Wang, D. Pan, M. Xiao, ACS Nano 7 (2013) 10654.

[40] M. Zheng, Z. Xie, D. Qu, D. Li, P. Du, X. Jing, Z. Sun, ACS Appl. Mater. Interfaces 5 (2013) 13242.

[41] Y. Dong, C. Chen, X. Zheng, L. Gao, Z. Cui, H. Yang, C. Guo, Y. Chi, C.M. Li, J. Mater. Chem. 22 (2012) 8764.

[42] M.L. Mueller, X. Yan, J.A. McGuire, L. Li, Nano Lett. 10 (2010) 2679.

[43] L. Cao, X. Wang, M.J. Meziani, F. Lu, H. Wang, P.G. Luo, Y. Lin, B.a. Harruff, L.M. Veca, D. Murray, S.-Y. Xie, Y.-P. Sun, J. Am. Chem. Soc. 129 (2007) 11318.

[44] P.G. Luo, F. Yang, S.-T. Yang, S.K. Sonkar, L. Yang, J.J. Broglie, Y. Liu, Y.-P. Sun, RSC Adv. 4 (2014) 10791.

[45] S.-C. Pu, M.-J. Yang, C.-C. Hsu, C.-W. Lai, C.-C. Hsieh, S.H. Lin, Y.-M. Cheng, P.-T. Chou, Small 2 (2006) 1308.

[46] D.R. Larson, W.R. Zipfel, R.M. Williams, S.W. Clark, M.P. Bruchez, F.W. Wise, W.W. Webb, Science 300 (2003) 1434.

[47] R. Liu, D. Wu, S. Liu, K. Koynov, W. Knoll, Q. Li, Angew. Chem. 121 (2009) 4668.

[48] H. Li, X. He, Y. Liu, H. Huang, S. Lian, S.-T. Lee, Z. Kang, Carbon 49 (2011) 605.

[49] M.J. Krysmann, A. Kelarakis, P. Dallas, E.P. Giannelis, J. Am. Chem. Soc. 134 (2012) 747.

[50] S. Zhu, Q. Meng, L. Wang, J. Zhang, Y. Song, H. Jin, K. Zhang, H. Sun, H. Wang, B. Yang, Angew. Chem. Int. Ed. 52 (2013) 3953.

[51] Y. Dong, H. Pang, H. Bin Yang, C. Guo, J. Shao, Y. Chi, C.M. Li, T. Yu, Angew. Chem. Int. Ed. 52 (2013) 7800.

[52] D. Qu, M. Zheng, L. Zhang, H. Zhao, Z. Xie, X. Jing, R.E. Haddad, H. Fan, Z. Sun, Sci. Rep. 4 (2014) 5294.

[53] H. Tao, K. Yang, Z. Ma, J. Wan, Y. Zhang, Z. Kang, Z. Liu, Small 8 (2011) 281.

[54] P. Agostinis, K. Berg, K.A. Cengel, T.H. Foster, A.W. Girotti, S.O. Gollnick, S.M. Hahn, M.R. Hamblin, A. Juzeniene, D. Kessel, M. Korbelik, J. Moan, P. Mroz, D. Nowis, J. Piette, B.C. Wilson, J. Golab, CA: Cancer J. Clin. 61 (2011) 250.

[55] Y. Wang, S. Kalytchuk, Y. Zhang, H. Shi, S.V. Kershaw, A.L. Rogach, J. Phys. Chem. Lett. 5 (2014) 1412.

[56] Z. Luo, Y. Lu, L.A. Somers, A.T.C. Johnson, J. Am. Chem. Soc. 131 (2009) 898.

[57] M. Zhang, L. Bai, W. Shang, W. Xie, H. Ma, Y. Fu, D. Fang, H. Sun, L. Fan, M. Han, C. Liu, S. Yang, J. Mater. Chem. 22 (2012) 7461.

[58] P. Yu, X. Wen, Y.-R. Toh, J. Tang, J. Phys. Chem. C 116 (2012) 25552.

[59] Y.-M. Long, C.-H. Zhou, Z.-L. Zhang, Z.-Q. Tian, L. Bao, Y. Lin, D.-W. Pang, J. Mater. Chem. 22 (2012) 5917.

[60] J.C. Vinci, I.M. Ferrer, S.J. Seedhouse, A.K. Bourdon, J.M. Reynard, B.A. Foster, F.V. Bright, L.A. Colon, J. Phys. Chem. Lett. 4 (2013) 239.

[61] H. Li, X. He, Z. Kang, H. Huang, Y. Liu, J. Liu, S. Lian, C.H.a. Tsang, X. Yang, S.-T. Lee, Angew. Chem. Int. Ed. 49 (2010) 4430.

[62] G. Eda, Y.-Y. Lin, C. Mattevi, H. Yamaguchi, H.-A. Chen, I.-S. Chen, C.-W. Chen, M. Chhowalla, Adv. Mater. 22 (2010) 505.

[63] L. Wang, S. Zhu, H. Wang, S. Qu, Y. Zhang, J. Zhang, Q. Chen, H. Xu, W. Han, B. Yang, H. Sun, ACS Nano 8 (2014) 2541.

[64] S. Chapman, M. Dobrovolskaia, K. Farahani, A. Goodwin, A. Joshi, H. Lee, T. Meade, M. Pomper, K. Ptak, J. Rao, R. Singh, S. Sridhar, S. Stern, A. Wang, J.B. Weaver, G. Woloschak, L. Yang, Nano Today 8 (2013) 454.

[65] X. Huang, F. Zhang, L. Zhu, K.Y. Choi, N. Guo, J. Guo, K. Tackett, P. Anilkumar, G. Liu, Q. Quan, H.S. Choi, G. Niu, Y. Sun, S. Lee, ACS Nano 7 (2013) 5684.

[66] L. Wu, X. Cai, K. Nelson, W. Xing, J. Xia, R. Zhang, A.J. Stacy, M. Luderer, G.M. Lanza, L.V. Wang, B. Shen, D. Pan, Nano Res. 6 (2013) 312.

[67] Z.M. Markovic, B.Z. Ristic, K.M. Arsikin, D.G. Klisic, L.M. Harhaji-Trajkovic, B.M. Todorovic-Markovic, D.P. Kepic, T.K. Kravic-Stevovic, S.P. Jovanovic, M.M. Milenkovic, D.D. Milivojevic, V.Z. Bumbasirevic, M.D. Dramicanin, V.S. Trajkovic, Biomaterials 33 (2012) 7084.

[68] H. Wang, J. Shen, Y. Li, Z. Wei, G. Cao, Z. Gai, K. Hong, P. Banerjee, S. Zhou, Biomater. Sci. 2 (2014) 915.

[69] V. Biju, T. Itoh, M. Ishikawa, Chem. Soc. Rev. 39 (2010) 3031.

[70] P.G. Luo, S. Sahu, S.-T. Yang, S.K. Sonkar, J. Wang, H. Wang, G.E. LeCroy, L. Cao, Y.-P. Sun, J. Mater. Chem. B 1 (2013) 2116.

[71] H. Ding, L.-W. Cheng, Y.-Y. Ma, J.-L. Kong, H.-M. Xiong, New J. Chem. 37 (2013) 2515.

[72] S.C. Ray, A. Saha, N.R. Jana, R. Sarkar, J. Phys. Chem. C 113 (2009) 18546.

[73] R. Hardman, Environ. Health Perspect. 114 (2006) 165.

[74] X. Zhang, S. Wang, L. Xu, L. Feng, Y. Ji, L. Tao, S. Li, Y. Wei, Nanoscale 4 (2012) 5581.

[75] S. Ruan, B. Zhu, H. Zhang, J. Chen, S. Shen, J. Qian, Q. He, H. Gao, J. Colloid Interface Sci. 422 (2014) 25.

[76] X. Zhang, S. Wang, C. Zhu, M. Liu, Y. Ji, L. Feng, L. Tao, Y. Wei, J. Colloid Interface Sci. 397 (2013) 39.

[77] S. Sahu, B. Behera, T.K. Maiti, S. Mohapatra, Chem. Commun. 48 (2012) 8835.

[78] N. Li, X. Liang, L. Wang, Z. Li, P. Li, Y. Zhu, J. Song, J. Nanopart. Res. 14 (2012) 1177.

[79] Z. Zhang, J. Hao, J. Zhang, B. Zhang, J. Tang, RSC Adv. 2 (2012) 8599.

[80] K.K.R. Datta, O. Kozak, V. Ranc, M. Havrdova, A.B. Bourlinos, K. Safarova, K. Hola, K. Tomankova, G. Zoppellaro, M. Otyepka, R. Zboril, Chem. Commun. 50 (2014) 10782.

[81] S. Nie, Nanomedicine 5 (2010) 523.

[82] H.S. Choi, W. Liu, P. Misra, E. Tanaka, J.P. Zimmer, B. Itty Ipe, M.G. Bawendi, J.V. Frangioni, Nat. Biotechnol. 25 (2007) 1165.

[83] S.-T. Yang, L. Cao, P.G. Luo, F. Lu, X. Wang, H. Wang, M.J. Meziani, Y. Liu, G. Qi, Y.-P. Sun, J. Am. Chem. Soc. 131 (2009) 11308.

[84] E.J. Goh, K.S. Kim, Y.R. Kim, H.S. Jung, S. Beack, W.H. Kong, G. Scarcelli, S.H. Yun, S.K. Hahn, Biomacromolecules 13 (2012) 2554.

[85] P. Huang, J. Lin, X. Wang, Z. Wang, C. Zhang, M. He, K. Wang, F. Chen, Z. Li, G. Shen, D. Cui, X. Chen, Adv. Mater. 24 (2012) 5104.

[86] M. Nurunnabu, Z. Khatun, K.M. Huh, S.Y. Park, D.Y. Lee, K.J. Cho, Y. Lee, ACS Nano 7 (2013) 6858.

[87] H.Y. Ko, Y.W. Chang, G. Paramasivam, M.S. Jeong, S. Cho, S. Kim, Chem. Commun. 49 (2013) 10290.

[88] L. Ye, K.-T. Yong, L. Liu, I. Roy, R. Hu, J. Zhu, H. Cai, W.-C. Law, J. Liu, K. Wang, J. Liu, Y. Liu, Y. Hu, X. Zhang, M.T. Swihart, P.N. Prasad, Nat. Nanotechnol. 7 (2012) 453.

[89] Y.J. Bao, J.J. Li, Y.T. Wang, L. Yu, L. Lou, W.J. Du, Z.Q. Zhu, H. Peng, J.Z. Zhu, Chin. Chem. Lett. 22 (2011) 843.

[90] M. Xu, L.V. Wang, Rev. Sci. Instrum. 77 (2006) 041101.

[91] I.L. Christensen, Y.-P. Sun, P. Juzenas, J. Biomed. Nanotechnol. 7 (2011) 667.

[92] Q. Liu, B. Guo, Z. Rao, B. Zhang, J.R. Gong, Nano Lett. 13 (2013) 2436.

[93] J. Tang, B. Kong, H. Wu, M. Xu, Y. Wang, Y. Wang, D. Zhao, G. Zheng, Adv. Mater. 25 (2013) 6569.

[94] M. Zheng, S. Liu, J. Li, D. Qu, H. Zhao, X. Guan, X. Hu, Z. Xie, X. Jing, Z. Sun, Adv. Mater. 26 (2014) 3554.

[95] V. Wood, V. Bulović, Nano Rev. 1 (2010) 5202.

[96] N. Gaponik, S.G. Hickey, D. Dorfs, A.L. Rogach, A. Eychmüller, Small 6 (2010) 1364.

[97] A.L. Rogach, J. Lupton, in: K. Mullen, U. Scherf (Eds.), Organic Light Emitting Devices, Wiley-VCH, Weinheim, Germany, 2006, pp. 319—332.

[98] Q. Dai, C.E. Duty, M.Z. Hu, Small 6 (2010) 1577.

[99] V.L. Colvin, M.C. Schlamp, A.P. Alivisatos, Nature 370 (1994) 354.

[100] K. Cho, E.K. Lee, W. Joo, E. Jang, T. Kim, S.J. Lee, S. Kwon, J.Y. Han, B. Kim, B.L. Choi, J.M. Kim, Nat. Photonics 3 (2009) 341.

[101] L. Qian, Y. Zheng, J. Xue, P.H. Holloway, Nat. Photonics 5 (2011) 543.

[102] W. Chung, H. Jung, C.H. Lee, S.H. Kim, Opt. Express 20 (2012) 25071.

[103] Y. Zhang, C. Xie, H. Su, J. Liu, S. Pickering, Y. Wang, W.W. Yu, J. Wang, Y. Wang, J. Hahm, N. Dellas, S.E. Mohney, J. Xu, Nano Lett. 11 (2011) 329.

[104] B. Chen, H. Zhong, W. Zhang, Z. Tan, Y. Li, C. Yu, T. Zhai, Y. Bando, S. Yang, B. Zou, Adv. Funct. Mater. 22 (2012) 2081.

[105] X. Yang, Y. Divayana, D. Zhao, K. Swee Leck, F. Lu, S. Tiam Tan, A. Putu Abiyasa, Y. Zhao, H. Volkan Demir, X. Wei Sun, Appl. Phys. Lett. 101 (2012) 233110.

[106] Z. Tan, Y. Zhang, C. Xie, H. Su, J. Liu, C. Zhang, N. Dellas, S.E. Mohney, Y. Wang, J. Wang, J. Xu, Adv. Mater. 23 (2011) 3553.
[107] F. Wang, Y. Chen, C. Liu, D. Ma, Chem. Commun. 47 (2011) 3502.
[108] X. Zhang, Y. Zhang, Y. Wang, S. Kalytchuk, S.V. Kershaw, Y. Wang, P. Wang, T. Zhang, Y. Zhao, H. Zhang, T. Cui, Y. Wang, J. Zhao, W.W. Yu, A.L. Rogach, ACS Nano 7 (2013) 11234.
[109] C.X. Li, C. Yu, C.F. Wang, S. Chen, J. Mater. Sci. 48 (2013) 6307.
[110] C. Sun, Y. Zhang, Y. Wang, W. Liu, S. Kalytchuk, S.V. Kershaw, T. Zhang, X. Zhang, J. Zhao, W.W. Yu, A.L. Rogach, Appl. Phys. Lett. 104 (2014) 261106.
[111] H. Choi, S.-J. Ko, Y. Choi, P. Joo, T. Kim, B.R. Lee, J.-W. Jung, H.J. Choi, M. Cha, J.-R. Jeong, I.-W. Hwang, M.H. Song, B.-S. Kim, J.Y. Kim, Nat. Photonics 7 (2013) 732.

Katerina Hola is a Ph.D. student in the lab of Prof. Zboril at the Regional Centre of Advanced Technologies and Materials. She received her bachelor degree (2010) in Chemistry at Charles University in Prague. Afterwards, she graduated in Physical Chemistry (2012) at Palacky University in Olomouc. Her research focuses on development of functional nanomaterials for bioapplications.

Dr. Yu Zhang received his BS in Electronic Engineering (2005) and Ph.D. in Circuit and System (2010) from Jilin University, China. Since 2010, he worked at the State Key Laboratory on Integrated Optoelectronics, College of Electronic Science and Engineering, Jilin University. In 2013, he joined Prof. Rogach's group at City University of Hong Kong as a postdoctoral fellow. His current research is focused on the fabrication of nanomaterial-based optoelectronic devices.

Yu Wang received his PhD (2013) from City University of Hong Kong under the supervision of Prof. Andrey L. Rogach. Currently, he is working as a postdoctoral fellow at the Regional Centre of Advanced Technologies and Materials, Palacky University, Czech Republic. His research focuses on synthesis and optical spectroscopy of colloidal semiconductor nanocrystals, carbon dots, lanthanide-based functional materials, and their hybrid structures, for the studies of light emission, self-assembly, charge and energy transfer.

Emmanuel P. Giannelis is the Walter R. Read Professor of Engineering at Cornell University. He received a BS degree in Chemistry from the University of Athens, Greece, and a Ph.D. in Chemistry from Michigan State University. He is currently the co-Director of the KAUST-CU Center for Energy and Sustainability. Giannelis serves or has served on the editorial boards of Small, Polymer, Chemistry of Materials, and Macromolecules. He is a member of several professional organizations and a corresponding member of the European Academy of Sciences. He is the author or co-author of more than 230 papers/book chapters and 18 patents/patent applications, and he has delivered more than 450 invited talks and seminars. His current research focuses on hybrids materials for energy and environmental applications.

Prof. Radek Zboril is a general director of the Regional Centre of Advanced Technologies and Materials at Palacky University in Olomouc, Czech Republic. He is the author or co-author of more than 200 scientific papers dealing with synthesis, characterization, and applications of nanomaterials for environmental, biomedical and industrial applications. His scientific focus includes silver nanoparticles, magnetic nanostructures, iron based nanomaterials and carbon nanostructures (graphene derivatives, carbon dots). He has participated in the development and implementation of several industrial technologies including the large-scale production of iron nanoparticles for *in-situ* groundwater treatment.

Andrey L. Rogach is a Chair Professor of Photonics Materials and the Director of the Centre for Functional Photonics at City University of Hong Kong. He received his Diploma in Chemistry and Ph.D. in Physical Chemistry from the Belarusian State University in Minsk, and worked as a staff scientist at the Institute of Physical Chemistry of the University of Hamburg (1995—2002), and at the Department of Physics of the Ludwig-Maximilians-Universität Munich (2002—2009), Germany, where he completed his Habilitation in Experimental Physics. His research focuses on synthesis, assembly and optical spectroscopy of colloidal semiconductor and metal nanocrystals and their hybrid structures, and their use for photovoltaic, photocatalytic and optoelectronic applications. He serves as an Associate Editor of *ACS Nano*.

View publication stats

C

Graphitic Nitrogen Triggers Red Fluorescence in Carbon Dots

The following pages (104–112) are available only in the printed version of the thesis. The discussed topic was under revision at the time of thesis submission.

The original text can be sent on the email request: katkahola@gmail.com; or lately find under given title.

D

Thiofluorographene-Hydrophilic Graphene Derivative with Semiconducting and Genosensing Properties

Materials Views
www.MaterialsViews.com

ADVANCED MATERIALS
www.advmat.de

COMMUNICATION

Thiofluorographene–Hydrophilic Graphene Derivative with Semiconducting and Genosensing Properties

*Veronika Urbanová, Kateřina Holá, Athanasios B. Bourlinos, Klára Čépe, Adriano Ambrosi, Adeline Huiling Loo, Martin Pumera, František Karlický, Michal Otyepka, and Radek Zbořil**

Graphene, a 2D sheet of sp^2-hybridized carbon atoms, is one of the most important materials in the current century due to its exceptional physical properties.[1–3] Graphene's excellent electronic, optical and thermal properties, chemical inertness, and mechanical stability makes it an ideal system for applications in biotechnology and biomedicine, such as gene and drug delivery, biosensing, bioimaging, and bioelectronics.[4–8] However, pristine graphene exhibits zero bandgap[9] and poor dispersibility in water, which limit its use in many current and future challenging applications. Covalent modification of graphene by attachment of suitable heteroatoms represents an attractive way to tailor its physical, chemical, and bioproperties. Theoretical and experimental works have shown that attachment of hydrogen,[10,11] oxygen,[12] and fluorine[13–16] is a suitable strategy for tuning the bandgap[17] and magnetic and optical properties.[18,19] Hence, the corresponding graphene derivatives, e.g., graphane, graphene oxide (GO), and fluorographene (GF), significantly broaden the application potential of graphene.[20] For example, the development of graphene derivatives for electrochemical sensing might result in fabrication of many new high performing analytical devices based on different strategies reflecting their particular chemical and/or physical properties.[8,21]

GF, as the first stoichiometric graphene derivative ($C/F = 1/1$), was introduced in 2010[14,22] and represents the thinnest known insulator. Importantly, its conductivity and magnetic properties[18] can be tuned by varying the degree of fluorination,[13] making GF an important candidate for electrochemical and sensing applications.[23] Covalent attachment of other functional groups to graphene is challenging because the new functionalities may exhibit entirely different properties to those of graphene, GO or GF. Among all the potential functional groups that can be attached to graphene, those able to communicate with biosystems are particularly desirable because the corresponding graphene derivatives may be applicable in biochemical sensing. From this point of view, sulfur containing groups represent very promising functionalities. It has been already shown that GO containing covalently attached sulfur groups can act as an electrocatalyst for oxygen reduction[24,25] or as an effective platform for immobilization of gold nanoparticles.[26] The synthetic strategy for production of these sulfur-modified graphene oxides (GSO) can be based on exfoliation of graphite oxide in the presence of sulfur gases (H_2S, CS_2, and SO_2),[24] annealing of GO with benzyl disulfide[25] or nucleophilic attack of the epoxide ring of GO.[27] It is worth mentioning that GO represents the most frequently used platform for performing covalent chemistry aimed at attachment of various functional groups.[28]

To the best of our knowledge, there have been no previous reports describing the covalent modification of GF. Here, we present the first example of covalent functionalization of GF by simple nucleophilic substitution of fluorine atoms in a polar solvent. Fluorine was substituted by nucleophilic sulfhydryl groups and this new graphene derivative was used as a low cost biosensor for impedimetric detection of DNA hybridization. Characterization of thiofluorographene by high resolution transmission electron microscopy/energy dispersive X-ray spectroscopy (HRTEM/EDS) technique, X-ray photoelectron spectroscopy (XPS), and Raman spectroscopy was supported by theoretical calculations to elucidate its stability, including the important role of residual fluorine, and predict its bandgap properties. Thus, we present a fairly challenging synthetic strategy for the preparation of new graphene derivatives through simple nucleophilic substitution of GF.

Thiofluorographene, G(SH)F, was prepared by exfoliation of fluorinated graphite under ultrasonication in *N,N*-dimethylformamide (DMF), followed by reaction of GF with sodium hydrosulfide in DMF, as illustrated in **Figure 1**. The sample was afterwards resuspended in water. Details of this synthetic procedure are provided in the Supporting Information.

Successful covalent attachment of sulfur was confirmed by both XPS and Raman spectroscopy. The XPS survey spectrum of thifluorographene (Figure S1a, Supporting Information) revealed the presence of carbon, fluorine, sulfur, and oxygen. The atomic ratios of peak intensities were 16.4 for C/S, 11.8 for

Dr. V. Urbanová, K. Holá, Dr. A. B. Bourlinos, Dr. K. Čépe,
Dr. F. Karlický, Prof. Dr. M. Otyepka, Prof. Dr. R. Zbořil
Regional Centre of Advanced Technologies and Materials
Department of Physical Chemistry, Faculty of Science
Palacky University
Slechtitelu 11, 783 71 Olomouc, Czech Republic
E-mail: radek.zboril@upol.cz

Dr. A. B. Bourlinos
Physics Department
University of Ioannina
Ioannina 45110, Greece

Dr. A. Ambrosi, A. H. Loo, Prof. Dr. M. Pumera
School of Physical and Mathematical Science
Division of Chemistry and Biological Chemistry
Nanyang Technological University
21 Nanyang Link, Singapore

DOI: 10.1002/adma.201500094

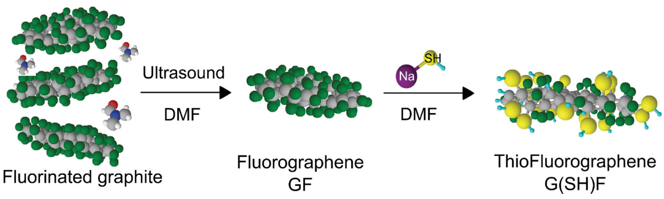

Figure 1. Preparation of thiofluorographene, G(SH)F, by exfoliation of fluorinated graphite and nucleophilic substitution of fluorine by sulfhydryl groups.

C/F, and 11.8 for C/O. The exact atomic composition, as well as deconvolution of the high resolution XPS spectra of C 1*s* and S 2*p*, can be found in Table S1 (Supporting Information). The atomic composition indicated that the functionalization of GF resulted in partial substitution of fluorine atoms by sulfur and formation of aromatic rings via partial defluorination. The high resolution C 1*s* spectrum (**Figure** 2a) also showed partial oxidation of the G(SH)F sample. There are apparent signals from C–O and O–C=O bonds. The presence of hydrophilic groups was also reflected by the good water dispersibility of G(SH)F (Figure S2, Supporting Information). Similarly, the high resolution S 2*p* spectrum revealed the partial presence of sulfur in oxidized forms, such as $-SO_3$ or $-SO_2(OH)$ (Figure 2b). We believe that the oxygen presence is related to the postpreparative treatment and water solubilization.

The Raman spectra of G(SH)F showed the presence of a D-band and G-band at characteristic values of 1350 and 1587 cm^{-1}, respectively (Figure S1c, Supporting Information). This confirmed the partial defluorination of graphene fluoride with formation of aromatic rings. The peak at around 830 cm^{-1} is characteristic for C–S–H bonding inplane and the peak at 1097 cm^{-1} can be attributed to S=O stretching.[29] The other two residual peaks at 566 and 2420 cm^{-1} were slightly decreased compared with typical values reported for C–S and S–H vibrations: C–S and S–H stretching modes typically lie in the regions 590–735 and 2530–2600 cm^{-1}, respectively.[29] Such values were probably reduced in the G(SH)F sample because of the presence of highly electronegative fluorine.

The TEM images revealed that the prepared sample, G(SH)F (see **Figure** 3a), did not significantly differ from the exfoliated GF (Figure S3a, Supporting Information). The thickness of G(SH)F was between 2 and 2.5 nm, derived from the atomic force microscopy measurements (Figure S3b,c, Supporting Information), corresponding to a few layer graphene structure. To better understand the elemental composition of the sample, chemical mapping of a sheet of G(SH)F was performed by STEM/EDS. Figure 3b shows overlying images for carbon and oxygen content obtained by elemental mapping. Oxygen was distributed over the sample in small islands, mainly on the edge of the sheet. On the contrary, sulfur and fluorine were homogenously spread across the sheet (Figure 3c). Importantly, the colors corresponding to sulfur and fluorine did not overlap, confirming successful modification of graphene with –SH groups. Similarly, the regions corresponding to oxygen and fluorine were observed in different regions of the sheet (Figure S4a, Supporting Information). The elemental mapping also confirmed the finding from the XPS analysis that the sulfur was partially present in oxidized form (the areas corresponding to sulfur and oxygen were partially overlaid, Figure S4b, Supporting Information). Clearly, the obtained results suggest the presence of small regions where F/SH substitution was successful and other regions where C–F bonds remained, thus stabilizing the G(SH)F structure.

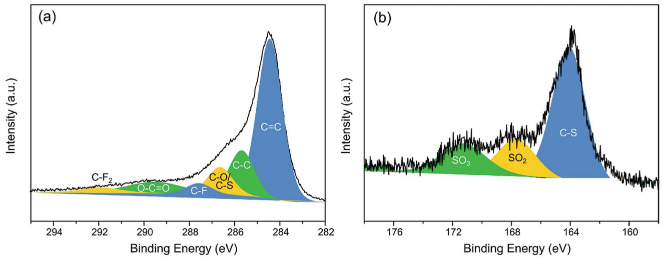

Figure 2. XPS spectra of G(SH)F: a) high resolution C 1s XPS spectrum; and b) high resolution S 2*p* XPS spectrum.

Density functional theory calculations were carried out to identify a suitable structural model for G(SH)F and estimate the electronic structure of this material. It should be noted, that sulfhydryl groups spontaneously desorbed from the pure graphene during all optimizations we performed. As the experimentally prepared G(SH)F still contained a large amount of fluorine atoms, we also examined the stability of sulfhydryl groups in the presence of fluorine atoms on graphene. We considered several positions of –SH groups with respect to the F atom, as shown in **Figure** 4a,b, and both possible directions of –SH adsorption were also taken into account, i.e., under (bottom) and above (top) the graphene plane. The most stable relative position of –F and –SH was the *ortho* top–bottom configuration (Figure 4c), followed by the *meta* top–top and *para* top–bottom configurations. It should be noted that the same preferences have been observed for graphene fluorination.[19] On the contrary, if the –SH group was located too far from –F (behind ring no. 4), it spontaneously desorbed from the graphene surface. These results show that the presence of fluorine atoms covalently bound to graphene is necessary to stabilize the –SH groups onto the graphene surface because the fluorine atom reduces the electron density on carbons to which the –SH groups attach. The F atom draws electron density away from the graphene, making the C–F bond rather ionic in character (Bader analysis suggested charge transfer of ≈0.57 e from C to F versus ≈0.06 e from S to C). The bond length of the covalent C–S bond was 1.87 Å, i.e., slightly longer than the C–S bond in CH_3SH (1.82 Å).[30] On the basis of the above mentioned stability considerations and taking into account the experimental chemical composition, we constructed several

© 2015 WILEY-VCH Verlag GmbH & Co. KGaA, Weinheim

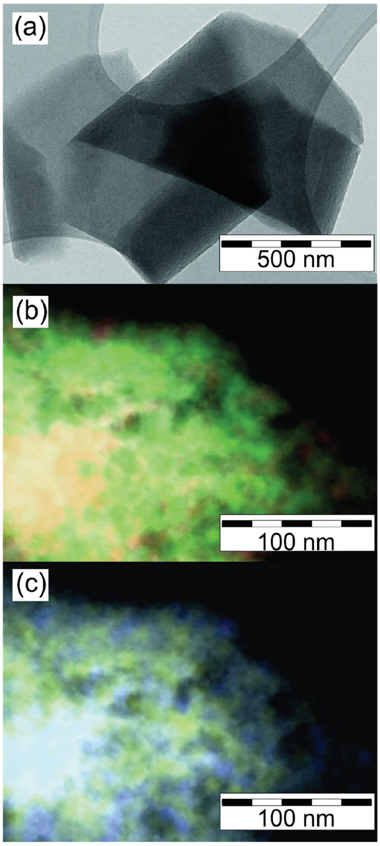

Figure 3. Transmission electron microscopy (TEM) images of G(SH)F: a) edge of the sheet obtained by TEM; b) surface of the sheet with STEM-EDS mapping of elemental composition (carbon: green, oxygen: red); c) STEM-EDS mapping of the same area (sulfur: blue, fluorine: yellow).

simplified models of G(SH)F containing only –F and –SH groups (Figure 4d) and explored the electronic properties of these 2D materials. For all the models, the density of electronic states showed similar features. The bandgaps ranged from 1 to 2 eV (at hybrid HSE06[31] functional level which provides realistic gaps[32] with composition and local arrangement of –SH and –F (Figure 4e); such values are typical for semiconductors. Fermi levels were located within the gaps and mid gap states appeared above the Fermi level (Figure 4e). The defect states within the electronic gap were caused by structural disorder and excitations between intragap states and states below or above the gap. This feature is expected to lead to optical absorption at energies below 1 eV (i.e., in the near infrared region).

Finally, we tested the applicability of the new 2D G(SH)F derivative for impedimetric sensing. Graphene-based impedimetric biosensors have been introduced as an advanced analytical method for detection of specific base sequences, which is important for the rapid diagnosis and treatment of various diseases.[33–37] Impedimetric biosensors for DNA detection provide several superior aspects compared with other DNA biosensors, including simplicity, higher sensitivities, and no requirements for labeling of the targets.[34,35] The operational principle of impedimetric DNA biosensors is commonly based on changes in the interfacial charges and conformation on the electrode surface after DNA probe immobilization and its hybridization with target DNA (see **Figure 5**). These changes can be advantageously monitored by impedance measurements.[38]

Single-stranded DNA probe was simply immobilized on the electrode surface through physical adsorption (see Supporting Information) due to π-stacking between the rings of nucleobases and the graphene derivative. Electrochemical impedance spectroscopy measurements were taken before and after hybridization.

Impedance measurements across a wide range of frequencies were performed in phosphate buffer solution containing $K_3[Fe(CN)_6]/K_4[Fe(CN)_6]$ as redox probe using a DEP chip modified by G(SH)F or GF, as well as a nonmodified one. Impedance spectra representing the electrochemical interaction between the redox probe and surface of modified or nonmodified DEP chips were fitted using a Randles equivalent circuit (Figure S5, Supporting Information).

Typical experimental data (symbol) and fitted data (curve) for an electrode modified with G(SH)F are shown in **Figure 6**a. In this case, the charge transfer (R_{ct}) changed, i.e., diameter of semicircle in observed Nyquist plot,[39] after each modification step of the sensing protocol (for details, see Supporting Information). Immobilization of ssDNA generated a negative charge on the electrode surface originating from the phosphate backbone of the ssDNA probe. Consequently, repulsion of the negatively charged redox probe inhibited electron transfer on the electrode surface, resulting in an increase of R_{ct} after ssDNA probe immobilization. An increase of R_{ct} was observed for electrodes modified by G(SH)F (Figure 6a, red color), GF (Figure S6b, Supporting Information, red color) as well as the nonmodified one (Figure S6a, Supporting Information, red color) compared with the R_{ct} value before ssDNA immobilization (Figures 6a and S6a,b, Supporting Information, black color). Upon hybridization in the presence of fully complementary target DNA, double-helical structure should be formed as a consequence of the complementarity between the probe and target. This conformational change is expected to be accompanied by a decrease in charge transfer resistance that can be explained by partial release of the duplex from electrode surface, and thus increasing availability of the electrode surface toward the redox probe.[40–42] In the case of the electrode modified by G(SH)F (see Figure 6a), hybridization with wild-type (fully complementary target) resulted in a significant decrease of R_{ct}, whereas hybridization with a negative control (noncomplementary target) had no effect on R_{ct}. Finally, when a DEP chip was incubated with a mutant (single-base mismatch target), a smaller decrease in R_{ct} was observed compared with that of wild-type. The lower hybridization efficiency in the latter case was due to the presence of unpaired nucleobases. On the contrary, similar experiments performed with electrodes modified with GF or nonmodified (Figure S6a,b, Supporting Information) did not show such changes in the R_{ct} value. The

© 2015 WILEY-VCH Verlag GmbH & Co. KGaA, Weinheim

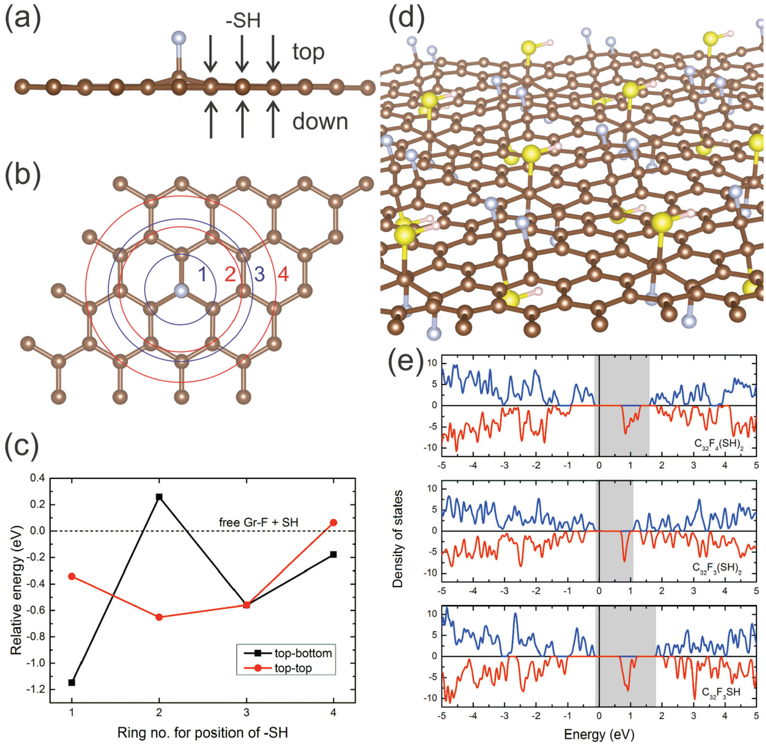

Figure 4. a,b) –SH adsorption sites (side and top views) used to evaluate the stability of –SH in the presence of –F on graphene. Equivalent –SH positions (due to symmetry) are grouped by rings (ring no. 1 for the nearest neighbors, ring no. 2 for second nearest neighbors, etc.) c) Relative energy of –SH group in different positions with respect to free Gr – F + SH. d) Simplified structural model of G(SH). e) Density of states for several simplified models of G(SH)F (chemical composition is designated in each subpanel; grey areas correspond to electronic gaps including midgap states). The Fermi energy was set as zero.

decrease of R_{ct} value appeared to be independent of target DNA type, indicating that any specific interactions occurred between the probe and target. Figure 6b shows a histogram comparing impedimetric detection of DNA hybridization recorded on three different platforms, i.e., DEP chips modified with G(SH)F, GF or nonmodified. The signal represents the R_{ct} ratio variation after hybridization with wild-type, mutant, and noncomplementary target (see caption of Figure 6b).

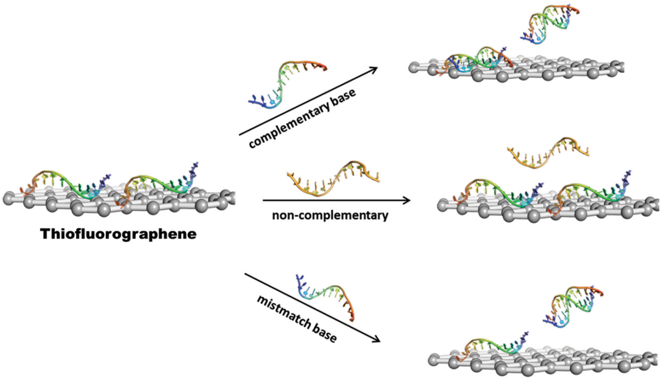

Figure 5. The operational principle of DNA biosensors based on a specific hybridization event between immobilized ssDNA and target DNA in a sample solution.

Clearly, covalently bound sulfur in the G(SH)F derivative enhanced the impedimetric sensing of DNA. This might be because the presence of sulfhydryl groups on the G(SH)F sensing platform allowed better immobilization and, most importantly, orientation of the ssDNA probe, resulting in good accessibility toward the DNA target and a highly efficient hybridization process.

In summary, we have presented a simple way to achieve covalent functionalization of graphene with –SH groups by reaction of GF with sodium hydrosulfide in DMF. After separation and redispersion in water, the hydrophilic thiofluorographene with semiconducting properties was found to

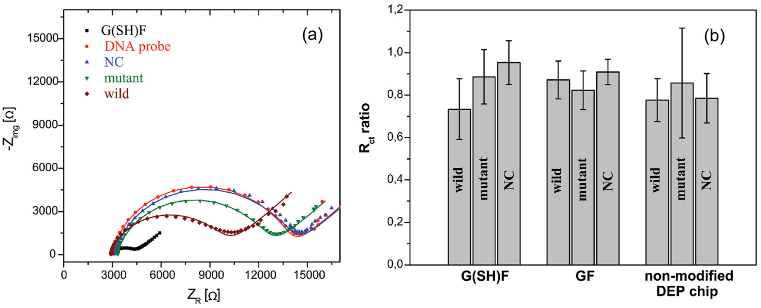

Figure 6. a) Nyquist plots showing responses obtained with DEP chips modified by G(SH)F after the modification with ssDNA probe (●) and different ssDNA target strands: noncomplementary (▲), mutant (▼) and wild-type (◆). All measurements were performed in 0.1 M phosphate buffer containing 10×10^{-3} M $K_3[Fe(CN)_6]/K_4[Fe(CN)_6]$. b) Histogram comparing impedimetric responses recorded with DEP chips modified by either G(SH)F or GF and a nonmodified DEP chip. Signals indicate ΔR_{ct} ratio = $R_{ct(target)} - R_{ct(blank)}/R_{ct(probe)} - R_{ct(blank)}$. Error bars correspond to triplicate experiments.

contain significant amounts of fluorine stabilizing the structure. Such a new graphene derivative could potentially be used as an advanced genosensor, as demonstrated by impedimetric detection of DNA hybridization. The properties could be further tailored by tuning of the SH/F ratio. Moreover, nucleophilic substitution of GF offers a promising strategy for synthesis of other challenging graphene derivatives (e.g., hydroxographene), thus providing an alternative to GO in 2D chemistry applications.

Supporting Information

Supporting Information is available from the Wiley Online Library or from the author.

Acknowledgements

The authors acknowledge support from the Ministry of Education,Youth and Sports of the Czech Republic (LO1305) and the Operational Program "Education for Competitiveness–European Social Fund" (CZ.1.07/2.3.00/20.0155 and CZ.1.07/2.3.00/20.0058 of the Ministry of Education, Youth and Sports of the Czech Republic). Funding received through student project IGA_PrF_2014023 of Palacký University is also gratefully acknowledged. This work was further supported by the Grant Agency of the Czech Republic [Grant No. P208/12/G016]. M. P. acknowledges Tier 2 grant (MOE2013-T2-1-056; ARC 35/13) from the Ministry of Education, Singapore.M.O. acknowledges funding from the Neuron fund for support of science. The authors also acknowledge K. M. Siskova for measurement of Raman spectra.

Received: January 8, 2015
Revised: January 30, 2015
Published online: February 18, 2015

---

[1] K. S. Novoselov, A. K. Geim, S. V. Morozov, D. Jiang, Y. Zhang, S. V. Dubonos, I. V. Grigorieva, A. A. Firsov, *Science* **2004**, *306*, 666.
[2] A. K. Geim, *Science* **2009**, *324*, 1530.
[3] X. Huang, Z. Zeng, Z. Fan, J. Liu, H. Zhang, *Adv. Mater.* **2012**, *24*, 5979.
[4] L. Feng, Z. Liu, *Nanomedicine* **2011**, *6*, 317.
[5] A. Bonanni, A. H. Loo, M. Pumera, *TrAC Trends Anal. Chem.* **2012**, *37*, 12.
[6] I. V. Pavlidis, M. Patila, U. T. Bornscheuer, D. Gournis, H. Stamatis, *Trends Biotechnol.* **2014**, *32*, 312.
[7] K. Yang, L. Feng, X. Shi, Z. Liu, *Chem. Soc. Rev.* **2013**, *42*, 530.
[8] M. Pumera, A. Ambrosi, A. Bonanni, E. L. K. Chng, H. L. Poh, *TrAC Trends Anal. Chem.* **2010**, *29*, 954.
[9] C. N. R. Rao, A. K. Sood, K. S. Subrahmanyam, A. Govindaraj, *Angew. Chem. Int. Ed.* **2009**, *48*, 7752.
[10] D. K. Samarakoon, X.-Q. Wang, *ACS Nano* **2009**, *3*, 4017.
[11] M. Pumera, C. H. A. Wong, *Chem. Soc. Rev.* **2013**, *42*, 5987.
[12] G. Eda, M. Chhowalla, *Adv. Mater.* **2010**, *22*, 2392.
[13] F. Karlický, K. K. R. Datta, M. Otyepka, R. Zbořil, *ACS Nano* **2013**, *7*, 6434.
[14] R. Zbořil, F. Karlický, A. B. Bourlinos, T. A. Steriotis, A. K. Stubos, V. Georgakilas, K. Šafářová, D. Jančík, C. Trapalis, M. Otyepka, *Small* **2010**, *6*, 2885.
[15] J. T. Robinson, J. S. Burgess, C. E. Junkermeier, S. C. Badescu, T. L. Reinecke, F. K. Perkins, M. K. Zalalutdniov, J. W. Baldwin, J. C. Culbertson, P. E. Sheehan, E. S. Snow, *Nano Lett.* **2010**, *10*, 3001.
[16] O. Leenaerts, H. Peelaers, A. D. Hernández-Nieves, B. Partoens, F. M. Peeters, *Phys. Rev. B* **2010**, *82*, 195436.
[17] F. Karlický, R. Zbořil, M. Otyepka, *J. Chem. Phys.* **2012**, *137*, 034709.
[18] R. R. Nair, M. Sepioni, I.-L. Tsai, O. Lehtinen, J. Keinonen, A. V. Krasheninnikov, T. Thomson, A. K. Geim, A. I. Grigorieva, *Nat. Phys.* **2012**, *8*, 199.
[19] F. Karlický, M. Otyepka, *J. Chem. Theory Comput.* **2013**, *9*, 4155.
[20] V. Georgakilas, M. Otyepka, A. B. Bourlinos, V. Chandra, N. Kim, K. C. Kemp, P. Hobza, R. Zboril, K. S. Kim, *Chem. Rev.* **2012**, *112*, 6156.
[21] S. Guo, S. Dong, *J. Mater. Chem.* **2011**, *21*, 18503.
[22] R. R. Nair, W. Ren, R. Jalil, I. Riaz, V. G. Kravets, L. Britnell, P. Blake, F. Schedin, A. S. Mayorov, S. Yuan, M. I. Katsnelson, H.-M. Cheng, W. Strupinski, L. G. Bulusheva, A. V. Okotrub, I. V. Grigorieva, A. N. Grigorenko, K. S. Novoselov, A. K. Geim, *Small* **2010**, *6*, 2877.
[23] X. Chia, A. Ambrosi, M. Otyepka, R. Zbořil, M. Pumera, *Chem. A Eur. J.* **2014**, *20*, 6665.
[24] H. L. Poh, P. Šimek, Z. Sofer, M. Pumera, *ACS Nano* **2013**, *7*, 5262.
[25] Z. Yang, Z. Yao, G. Li, G. Fang, H. Nie, Z. Liu, X. Zhou, X. Chen, S. Huang, *ACS Nano* **2012**, *6*, 205.

© 2015 WILEY-VCH Verlag GmbH & Co. KGaA, Weinheim

[26] D. Du, Z. Zou, Y. Shin, J. Wang, H. Wu, M. H. Engelhard, J. Liu, I. A. Aksay, Y. Lin, *Anal. Chem.* **2010**, *82*, 2989.

[27] H. R. Thomas, A. J. Marsden, M. Walker, N. R. Wilson, J. P. Rourke, *Angew. Chem. Int. Ed.* **2014**, *53*, 7613.

[28] S. Eigler, A. Hirsch, *Angew. Chem. Int. Ed.* **2014**, *53*, 7720.

[29] D. Lin-Vien, N. B. Colthup, W. G. Fateley, J. G. Grasselli, *The Handbook of Infrared and Raman Characteristic Frequencies of Organic Molecules*, Elsevier Inc., Dordrecht, The Netherlands **1991**, pp. 225–250.

[30] Table of Interatomic Distances and Configuration of Molecules and Ions, Special Publication No 11; Supplement 1956–1959, Special Publication No 18, Chemical Society, London 1958, 196.

[31] A. V. Krukau, O. A. Vydrov, A. F. Izmaylov, G. E. Scuseria, *J. Chem. Phys.* **2006**, *125*, 224106.

[32] F. Karlický, M. Otyepka, *Ann. Phys.* **2014**, *526*, 408.

[33] H. Berney, J. West, E. Haefele, J. Alderman, W. Lane, J. K. Collins, *Sens. Actuator B-Chem.* **2000**, *68*, 100.

[34] A. Bonanni, M. del Valle, *Anal. Chim. Acta* **2010**, *678*, 7.

[35] A. Bonanni, M. Pumera, *ACS Nano* **2011**, *5*, 2356.

[36] S. Pan, L. Rothberg, *Langmuir* **2005**, *21*, 1022.

[37] J. Shendure, E. Lieberman Aiden, *Nat. Biotechnol.* **2012**, *30*, 1084.

[38] E. Katz, I. Willner, *Electroanalysis* **2003**, *15*, 913.

[39] S. M. Park, J. S. Yoo, *Anal. Chem.* **2003**, *75*, 455.

[40] F. Davis, A. V. Nabok, S. P. Higson, *J. Biosens. Bioelectron.* **2005**, *20*, 1531.

[41] J. J. Gooding, A. Chou, F. J. Mearns, E. L. S. Wong, K. L. Jericho, *Chem. Commun.* **2003**, 1938.

[42] A. H. Loo, A. Bonanni, M. Pumera, *Electrochem. Commun.* **2013**, *28*, 83.

© 2015 WILEY-VCH Verlag GmbH & Co. KGaA, Weinheim

E

Room temperature organic magnets derived from sp^3 functionalized graphene

nature COMMUNICATIONS

ARTICLE

Received 4 Oct 2016 | Accepted 9 Jan 2017 | Published 20 Feb 2017

DOI: 10.1038/ncomms14525

OPEN

Room temperature organic magnets derived from sp^3 functionalized graphene

Jiří Tuček[1], Kateřina Holá[1], Athanasios B. Bourlinos[1,2], Piotr Błoński[1], Aristides Bakandritsos[1], Juri Ugolotti[1], Matúš Dubecký[1], František Karlický[1], Václav Ranc[1], Klára Čépe[1], Michal Otyepka[1] & Radek Zbořil[1]

Materials based on metallic elements that have *d* orbitals and exhibit room temperature magnetism have been known for centuries and applied in a huge range of technologies. Development of room temperature carbon magnets containing exclusively *sp* orbitals is viewed as great challenge in chemistry, physics, spintronics and materials science. Here we describe a series of room temperature organic magnets prepared by a simple and controllable route based on the substitution of fluorine atoms in fluorographene with hydroxyl groups. Depending on the chemical composition (an F/OH ratio) and sp^3 coverage, these new graphene derivatives show room temperature antiferromagnetic ordering, which has never been observed for any *sp*-based materials. Such 2D magnets undergo a transition to a ferromagnetic state at low temperatures, showing an extraordinarily high magnetic moment. The developed theoretical model addresses the origin of the room temperature magnetism in terms of sp^2-conjugated diradical motifs embedded in an sp^3 matrix and superexchange interactions via –OH functionalization.

---

[1] Regional Centre of Advanced Technologies and Materials, Department of Physical Chemistry, Faculty of Science, Palacky University in Olomouc, Slechtitelu 27, Olomouc 783 71, Czech Republic. [2] Physics Department, University of Ioannina, Ioannina 45110, Greece. Correspondence and requests for materials should be addressed to R.Z. (email: radek.zboril@upol.cz).

Since the first isolation of graphene—2D carbon allotrope—in 2004 (ref. 1), vast efforts have been made to understand its unique mechanical, electronic, optical and transport properties[2–8]. Among other properties, it exhibits superior mechanical strength,[4] a very large specific surface area[9], high carrier mobility[2], transparency[10] and thermal conductivity[6]. Moreover, several peculiar physical phenomena have been observed in graphene such as the ambipolar effect[1], room temperature half-integer quantum Hall effect[7], nonlinear Kerr effect[11] and Casimir effect[12]. Because of its remarkable properties, graphene has great potential in a broad portfolio of technical applications[13] including robust lightweight, thin and flexible display screens[14], field-effect and ballistic transistors[15], spin transistors and spin logic devices[16], photosensitive transistors[17], organic photovoltaic cells[18], organic light-emitting diodes[19] and conductive plates in supercapacitors and lithium-ion, lithium-sulfur and lithium-air batteries[9,20,21].

However, the practical applications of graphene are limited by its zero band gap, hydrophobicity and absence of long-range magnetic ordering. One potentially effective way of eliminating these drawbacks is to instead use covalently functionalized graphene derivatives in which specific atoms or functional groups are covalently bound to the graphene sheet to tune its physicochemical and biochemical properties[22]. Important examples of covalently modified graphene derivatives include graphene oxide[23], graphane[24] and fluorographene[25]. In particular, graphene oxide and fluorographene can be further readily functionalized with various other functional groups (for example, –Cl, –I and –SH), offering further scope for band gap tuning and the introduction of new electronic, optical and sensing properties[23,26,27].

Covalent functionalization has thus made it possible to produce graphene derivatives with modified band gap properties and altered hydrophilicity/hydrophobicity[22,28]. However, development of graphene derivative with room temperature magnetic behaviour is a major unaddressed challenge despite the investment of considerable effort into imprinting stable magnetic centres into graphitic structures and inducing long-range magnetic ordering across 2D carbon networks[29,30]. Several key strategies have been suggested to induce spin-carrying sp^3 (paramagnetic) states in graphene-related structures[29,30] such as formation of defects and vacancies,[30] insertion of non-carbon atoms (for example, boron, nitrogen and sulfur) into the graphene lattice[31–33], cutting of graphene sheets creating edges with a specific geometry (for example, zigzag graphene nanoribbons)[34], covalent functionalization with functional groups[29,30,35–37], light-atom adsorption (that is, adatoms)[38–40], transition-metal-atom adsorption[41] and electric field engineering[42]. Particularly, the pioneering work of Nair *et al.*[43] suggested that it may be possible to imprint paramagnetic centres into graphene by combining defects arising from partial fluorination with appropriate (C–F) functionalization. All these approaches demonstrate the possibility to combine various sources for creation and π-electron system-based coupling of spin-carrying sp^3 states to induce magnetism into graphene. However, π-electron system-mediated interactions are weak and, hence, magnetic ordering collapses at relatively low temperatures ($<$ 100 K). Thus, room temperature magnetism in graphene and graphene derivatives, maintained by the π-electron system, is heavily questioned in literature[13]; if such a behaviour was experimentally observed, the presence of impurities of transition metal origin (Fe, Ni, Co), originating from either the synthesis itself or sample handling, was not properly excluded, leading to misinterpretation of results and inaccurate conclusions[13].

Here we report a discovery of organic graphene-based magnets with a magnetic ordering sustainable up to room temperature due to the suitable sp^3 functionalization. A series of magnetic carbons designated as hydroxofluorographenes are prepared from fluorographene by exchanging some of its fluorine atoms for hydroxyl groups. The chemical composition of hydroxofluorographenes can be controlled through reaction conditions and choice of –OH-containing precursors. Strikingly, hydroxofluorographenes with an appropriate composition (an F/OH ratio) exhibit antiferromagnetic ordering at room temperature, a magnetic behaviour not previously observed for any graphene derivative or *sp*-based material. At low temperatures, these hydroxofluorographenes undergo a transition to a ferromagnetic state with one of the highest magnetization values reported among graphene-based material. Based on the set of experimental data and high throughput first principles calculations on a large number of atomic configurations with varying F/OH ratio, we establish that the unique magnetism is attributed to a network of functionalization-induced sp^2-conjugated carbon diradical motifs embedded in an sp^3 matrix, and the ability of –OH groups to stabilize magnetically ordered state up to room temperature due to emergence of superexchange interactions. Moreover, the suggested theoretical model for hydroxofluorographene system has a universal nature and covers both 'diradical motifs-induced magnetism' appearing at high sp^3 coverages and sustaining up to room temperature and 'defect-induced magnetism', which emerges at lower degrees of sp^3 functionalization with limited sustainability at higher temperatures.

Results

Physicochemical properties of hydroxofluorographenes. The synthesis of hydroxofluorographenes is based on the chemistry of fluorographene (GF), which has been investigated experimentally and computationally by our group, leading to the development of practical procedures for the direct nucleophilic substitution of fluorine[26,27]. The series of five hydroxofluorographenes differing in degree of sp^3 functionalization, an F/OH ratio, and magnetic features were prepared by ultrasonic exfoliation of fluorographite (C_1F_1) in *N*,*N*-dimethylformamide (DMF), after which the exfoliated material was treated with –OH-containing precursors for various reaction temperatures and time. For detailed chemical, structural, morphological and magnetic characterization, we have selected the representative sample, denoted as G(OH)F, prepared by reaction of fluorographene with tetramethylammonium hydroxide in DMF for 3 days (Fig. 1; for more details, see 'Methods' section below).

The overall chemical composition of G(OH)F sample was determined by X-ray photoelectron spectroscopy (XPS) analysis (Supplementary Fig. 1), revealing the average contents of oxygen, fluorine, carbon and nitrogen to be 6.1, 27.2, 65.4 and 1.3 at.%, respectively. To exclude the presence of metals, which would affect magnetic features of the system, we performed inductively coupled plasma mass spectrometry (ICP-MS) analysis confirming their negligible contents generally below 24 ppm (Supplementary Table 1). The C/F ratio of G(OH)F (2.4/1) found from XPS analysis is greater than that of its precursor, fluorographene (1/1), reflecting the sample's partial defluorination and formation of some aromatic sp^2 regions during G(OH)F synthesis. The presence of oxygen, fluorine, carbon and nitrogen was inferred from energy-dispersive X-ray (EDX) spectrum measured for the G(OH)F sample (Supplementary Fig. 2). The small content of nitrogen comes from DMF solvent residues as clearly seen in the thermogravimetric curve (Supplementary Fig. 3a) exhibiting a negligible loss (0.41 wt.%) up to 100 °C due to release of adsorbed water, while the secondary weight decrease (1.11 wt.%) between 108 and 140 °C is evidently related to DMF evolution. To confirm the presence of fluorine and hydroxyl groups in the G(OH)F structure, the G(OH)F sample was

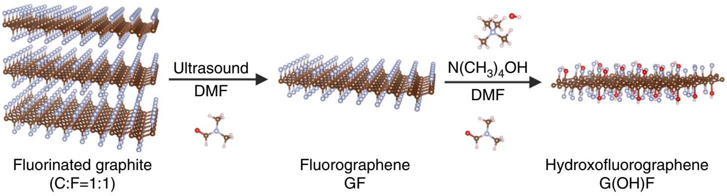

Figure 1 | Representative preparation of G(OH)F. The scheme depicting the chemical procedure towards G(OH)F.

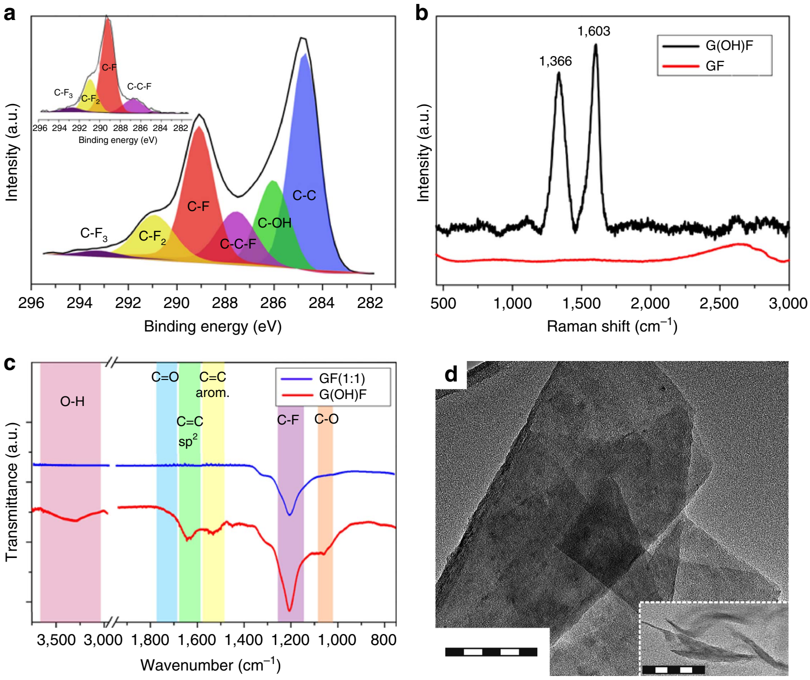

Figure 2 | Physicochemical characterization of GF and G(OH)F. (**a**) High-resolution C 1s spectrum of G(OH)F and GF precursor (inset). (**b**) Raman spectra of G(OH)F (black line) and GF (red line). (**c**) FT-IR spectra of G(OH)F (red line) and GF (blue line). (**d**) HRTEM image (scale bar, 100 nm) of a G(OH)F sheet with an inset (scale bar, 100 nm) demonstrating a single-sheet character of G(OH)F.

subjected to thermal decomposition under nitrogen atmosphere, heating from room temperature to 900 °C, and the release of gases and ions was monitored by mass spectrometry (Supplementary Fig. 3b). The release of hydroxyl ions started once the temperature rose above 200 °C; this was attributed to the removal of covalently attached –OH groups because the adsorbed water molecules were released at temperatures of up to 100 °C. The two peaks appearing in the evolved gas profile for the –OH groups can be well explained in terms of the stability of –OH groups in G(OH)F strongly dependent on their local environment (Supplementary Fig. 3c). Hence, the first peak, with maximum at 220 °C, corresponds to the evolution of less stable –OH groups, which are released before any evolution of fluorine, while the second peak, centred at 260 °C, corresponds to –OH groups released after the onset of fluorine evolution, which would radically change their local environment and stability (Supplementary Fig. 3c). The fluorine ions were detected in a broad range of temperatures with the maximum of fluorine released at 500 °C. Importantly, carbon dioxide and carbon monoxide, whose release typically indicates the presence of carboxylic and epoxy groups, were not detected at any temperature.

The successful attachment of hydroxyl groups was also confirmed by high-resolution C 1s XPS data (Fig. 2a) showing that the product contained C–O and C–C bonds, which were not present in the XPS pattern of the GF precursor (inset in Fig. 2a). Formation of aromatic sp^2 regions was also indicated by Raman spectroscopy (Fig. 2b): Raman spectrum of the G(OH)F sample exhibited a characteristic G-band at 1,603 cm^{-1} and a disorder-induced D-band at 1,366 cm^{-1}, whereas pristine fluorographene is Raman-inactive[44]. The Fourier transform infrared (FT-IR) spectrum of G(OH)F featured vibrations in the range of 1,510–1,670 cm^{-1} corresponding to aromatic regions, and C–F vibrations at 1,200 cm^{-1} (Fig. 2c). Importantly, its FT-IR spectrum also showed peaks associated with covalent C–OH bonds that were not observed in the FT-IR spectrum of fluorographene, namely a C–O vibration peak at 1,058 cm^{-1} and a broad O–H vibration peak at

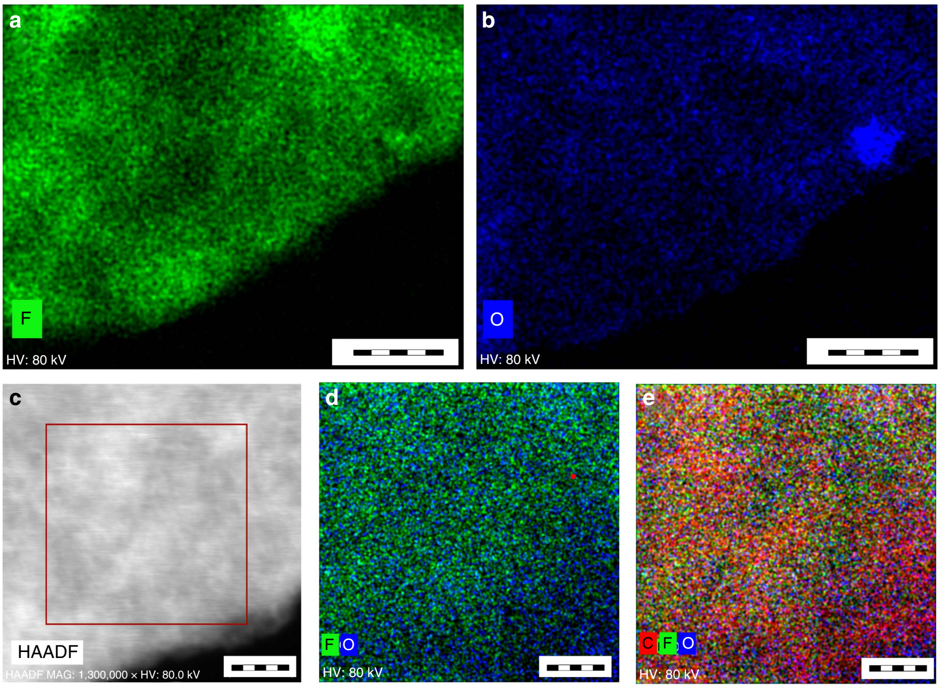

Figure 3 | Chemical mapping of a G(OH)F sheet by STEM-HAADF. (**a**) Distribution of fluorine atoms on the G(OH)F sheet (scale bar, 50 nm). (**b**) Distribution of oxygen atoms on the G(OH)F sheet (scale bar, 50 nm). (**c**) STEM/HAADF image of the G(OH)F sheet (scale bar, 10 nm). (**d**) Combined F/O chemical mapping of the G(OH)F sheet (scale bar, 6 nm). (**e**) Combined C/F/O chemical mapping of the G(OH)F sheet (scale bar, 6 nm).

3,250 cm^{-1}. These results indicate that a well-defined covalently modified graphene derivative containing aromatic rings and two characteristic functional groups, C–OH and C–F, can be prepared from fluorographene via a simple synthetic procedure involving chemical exfoliation followed by nucleophilic substitution. The stoichiometric formula for this representative material is approximately $C_{18}(OH)_{1.8}F_{7.2}$ with C_{18} as a supercell used in the theoretical model (see below).

Atomic force microscopy experiments indicated that after the exfoliation process, the sample consisted of single-layered sheets less than 1 nm thick (Supplementary Fig. 4), however, a few-layered sheets with thickness of several nanometres were observed as well. Similarly, very thin highly transparent single sheets were observed by high-resolution transmission electron microscopy (HRTEM) (Fig. 2d). The distribution of fluorine and oxygen within the sheet was investigated by scanning transmission electron microscope–high-angle annular dark-field imaging (STEM–HAADF) chemical mapping (Fig. 3), which showed that fluorine and oxygen (–OH) groups were distributed rather homogeneously within the G(OH)F structure, without any large fluorine (or oxygen) islands (Fig. 3e).

Magnetic properties of hydroxofluorographenes. To exclude the effect of tetramethylammonium hydroxide and possible trace impurities contained in this precursor on magnetic behaviour of the system, we measured the temperature evolution of mass magnetic susceptibility (χ_{mass}), confirming its solely diamagnetic character within the whole temperature range (Supplementary Fig. 5). In the case of other precursor, GF, the temperature profile of χ_{mass} can be fitted employing the Curie law ($\chi_{\mathrm{mass}} = C/T$, where C is the Curie constant and T is the temperature) and temperature-independent diamagnetic contribution (Supplementary Fig. 6). However, the paramagnetic response of GF is very weak due to minor defects in the GF structure; its magnetic behaviour is dominated by the diamagnetic term in accordance with the previous study[43]. Thus, both precursors used for synthesis of G(OH)F exhibit non-magnetic behaviour.

Importantly, the substitution of some of F atoms of GF by –OH groups produces a material with radically different magnetic properties. Observed magnetic features are not definitely driven by tiny impurities identified by ICP-MS as the sum of their χ_{mass}, considering the magnetic moments of detected elements and recalculating their magnetic response to their weight in the sample and under an external magnetic field of 10 kOe, is four orders lower than the measured χ_{mass} of G(OH)F. Contrary to GF, the temperature dependence of χ_{mass} for G(OH)F is not described by the Curie or Curie–Weiss laws from 5 to 300 K, implying a magnetically ordered state up to room temperature. More strikingly, at room temperature, G(OH)F exhibits antiferromagnetic (AFM) behaviour as χ_{mass} (or $1/\chi_{\mathrm{mass}}$) decreases (or increases) with lowering the temperature (Fig. 4a and Supplementary Fig. 7). Thus, at room temperature, G(OH)F shows AFM ordering, a behaviour never observed for any 2D organic material having only *s* and/or *p* electrons. At low temperatures, an abrupt increase in χ_{mass} is observed followed by a saturation trend, which is characteristic of ferromagnetic (FM) materials. The passage from the AFM to FM regime is also clearly evident from the $1/\chi_{\mathrm{mass}}$ versus temperature curve with an inflection point at ~62 K (Supplementary Fig. 7). Thus, below ~62 K (the FM/AFM transition temperature,

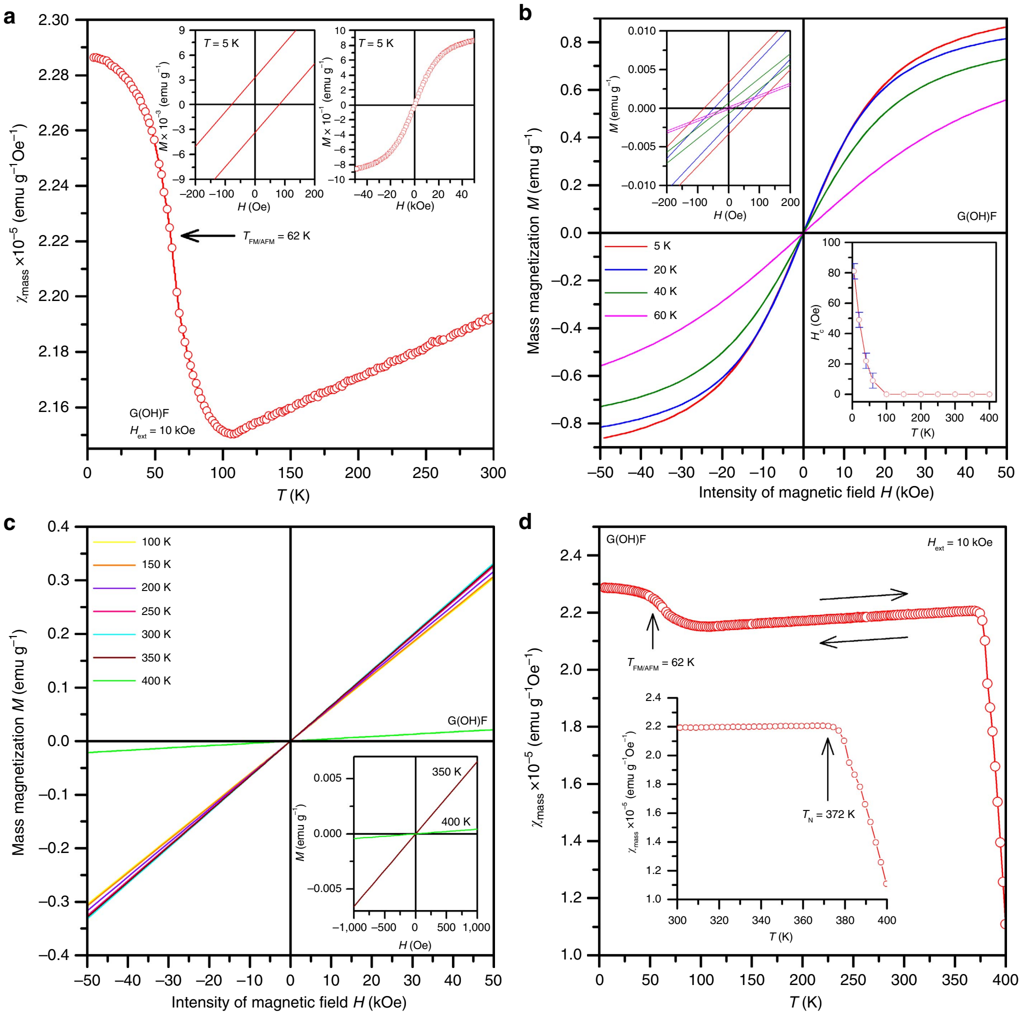

Figure 4 | Magnetization measurements. (**a**) Temperature evolution of the mass magnetic susceptibility (χ_{mass}) of G(OH)F, measured under an external magnetic field (H_{ext}) of 10 kOe. The insets show the hysteresis loops of G(OH)F at 5 K, which indicate non-zero coercivity and a saturation magnetization of almost 1 emu g^{-1}. (**b**) Isothermal magnetization curves of G(OH)F at temperatures of 5–60 K. The insets show the profile of the hysteresis loops around the origin and the temperature dependence of coercivity (H_C). (**c**) Isothermal magnetization curves of G(OH)F, recorded from 100 to 400 K. The inset shows the profile of the isothermal magnetization curves at 350 and 400 K, demonstrating a dramatic decrease in the curve's gradient upon increasing temperature above 350 K; this implies a transition from an AFM state to a paramagnetic regime. (**d**) Temperature evolution of χ_{mass} of G(OH)F, measured under an external magnetic field of 10 kOe. The arrows show the reversibility of the χ_{mass} profile on warming the sample from 5 to 400 K and then cooling from 400 to 5 K. The inset depicts the behaviour of χ_{mass} between 300 and 400 K including its sudden drop above 370 K, which is indicative of a transition from an AFM state to the paramagnetic regime with a Néel transition temperature of about 372 K. Note: the paramagnetic signal from the non-interacting paramagnetic centres was subtracted from the χ_{mass} data.

$T_{\mathrm{FM/AFM}}$), G(OH)F behaves in an FM manner. In other words, the FM state is a ground magnetic state for G(OH)F and the AFM regime can be regarded as thermally excited state. It is worth noting that similar FM-AFM transitions have been observed in various molecular radical-based systems[45]. The low-temperature FM state was further supported by G(OH)F isothermal magnetization curve, measured at 5 K: the curve exhibits hysteresis with a coercivity of ~80 Oe (inset in Fig. 4a). Moreover, the magnetization of G(OH)F saturates above a value of 1 emu g^{-1}, placing G(OH)F among the strong magnetic graphene-based systems including doped and functionalized graphenes and graphene derivatives. However, unlike other graphene-based materials, which also show FM features at low temperatures[13,28], G(OH)F synthesized as described above does not lose its magnetic ordering at room temperature; instead, it passes from an FM to AFM state as the temperature raises.

To address the evolution/sustainability of the magnetic properties of G(OH)F, we performed measurements of the material's hysteresis loops and χ_{mass} under heating from

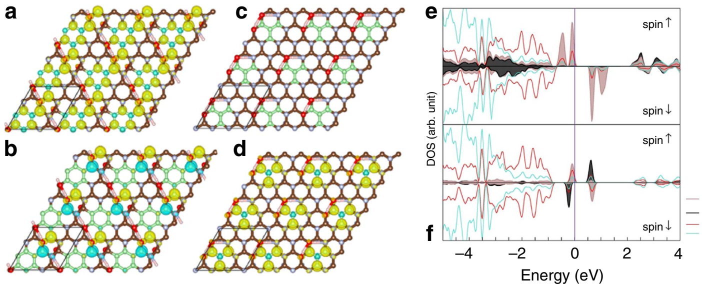

Figure 5 | Spin densities and densities of states. (**a**,**b**) The *m*-xylylene-like motif (green) of G(OH)F embedded in an sp^3 lattice with the corresponding FM (**a**) and AFM (**b**) phases, with up/down spin densities shown in yellow/blue. (**c**,**d**) sp^3-embedded trimethylenemethane-like motif with the corresponding FM spin density. Brown/green, blue, red and pink balls represent carbon, fluorine, oxygen and hydrogen atoms, respectively. (**e**) DOS of the GS FM phase. (**f**) DOS of the AFM phase. For (**e**) and (**f**), orbital contributions of individual atoms (labelled in the inset legend) are presented in both spectra. Electronic states of carbon atoms with up/down magnetic moments are plotted by brown/black line. Electronic states with the same spin direction can hybridize with each other. The hybridization involves the occupied and unoccupied spin-up states (**e**) and the occupied and unoccupied spin-up or spin-down states (**f**). Such kind of coupling not involving a finite density of states at E_F is termed as the superexchange interaction. Both DOS spectra show a significant contribution of oxygen orbitals to the midgap states, which implies an important role of -OH group in the superexchange interactions.

5 to 400 K and cooling from 400 to 5 K (Fig. 4b–d and Supplementary Fig. 7). Between 5 and 60 K, the isothermal magnetization curves of G(OH)F reveal hysteresis with non-zero coercivity and remanent magnetization that both decrease with increasing temperature as would be expected for an FM ground state (Fig. 4b and its insets). Above 60 K, the hysteretic behaviour disappears and profiles of the isothermal magnetization curves are consistent with those expected for an AFM system (Fig. 4c). Importantly, above 350 K, the gradient of the magnetization versus field curve decreases sharply, implying a transition from an AFM to paramagnetic regime (inset in Fig. 4c,d), with the Néel temperature of ~372 K (see the sudden increase and/or drop in $1/\chi_{\mathrm{mass}}$ and/or χ_{mass}, respectively, above 370 K in Fig. 4d and Supplementary Fig. 7). Importantly, the profile of the χ_{mass} versus T curve is reversible at temperatures of 5–400 K, meaning that mild thermal treatment does not cause any irreversible structural or magnetic changes in the material (arrows in Fig. 4d). In the paramagnetic region, the χ_{mass} profile fits well with the Curie–Weiss law ($\chi_{\mathrm{mass}} = C/(T+\theta)$, where θ is the Weiss temperature) for AFM materials with $\theta \approx 186$ K. The difference between the values of T_N and θ can be explained by different (not defects-like) origin of magnetic moments in the G(OH)F system and AFM state not being the ground magnetic state. More strikingly, the temperature evolution of coercivity and remanent magnetization in the FM state does not follow any formulas valid for *d*-electron driven magnetism (that is, Brillouin function, Bloch function and so on), further indicating a completely new source of magnetic moments—motifs—induced in the G(OH)F lattice (insets in Fig. 4b).

Discussion

To explain the origin and sustainability of magnetism in G(OH)F systems and effect of chemical composition on magnetic features, we applied a high throughput theoretical screening of random structures of $C_{18}(OH)_yF_x$ (that is, with a large number (more than 1,400) of configurations, see Supplementary Table 2 listing abundances of FM and AFM ground states in % of $C_{18}(OH)_yF_x$), simulating thus reliably a random nature of the derivatization. We focused on identification of the nature of magnetic motifs driving room temperature magnetism, origin of FM-AFM transition, role of –OH groups in magnetic communication of these motifs and effect of $C_{18}(OH)_yF_x$ (an F/OH ratio) on magnetic properties of the system.

Regarding the magnetism origin, we identified energetically stable diradical motifs, typically consisting of sp^2-conjugated islands embedded in an sp^3 matrix, which were responsible for the observed magnetic behaviour. A prototypical example is the *m*-xylylene motif, which comprises eight sp^2 carbon atoms and has an FM ground state (GS) with a spin moment $S = 1$ and an FM-AFM spin-flip gap of 0.012 eV (Fig. 5a,b). Another important motif consists of four conjugated sp^2 carbon atoms in a triangular configuration that resembles trimethylenemethane (Fig. 5c,d). Structures containing the trimethylenemethane motif have a spin moment $S = 1$ (FM GS) and an FM-AFM spin-flip gap of 0.012 eV. It is worth noting that both *m*-xylylene and trimethylenemethane are typical organic diradicals that are known sources of molecular magnetism[46]. Structural details of both prototypical diradical motifs are depicted in Supplementary Fig. 8. The presence of diradical motifs with FM GS and small FM-AFM spin-flip gap is consistent with the experimental FM-AFM transition observed for G(OH)F at ~62 K.

The electronic structure displayed as density of states (DOS) of G(OH)F with the *m*-xylylene-like motif both in the FM and AFM phase (Fig. 5e,f) provides insight into the nature of G(OH)F magnetism. The DOS in the vicinity of the Fermi level (E_F) is dominated by spin-polarized midgap states. Two midgap states per spin channel are visible in the FM phase (Fig. 5e), and only one channel is occupied. The midgap states reflect an imbalance of graphene bipartite lattice, $N = N_A - N_B$, where N_A and N_B are the number of atoms belonging to each sublattice. As the GS spin of imbalanced bipartite lattice is given by $2S = |N_A - N_B|$ (ref. 47), both diradical motifs have $N = 2$ and, hence, $S = 1$. The spin-polarized midgap states and bulk of positive (up) spin density reside within the diradical motif on the majority sublattice, while the electronic states of the minority sublattice form a band extending from 2.1 eV above E_F. Note that the electronic states with the same spin direction hybridize with each other.

The DOS plot indicates on the superexchange interactions[48] in maintaining the GS FM ordering within the diradical motifs. A substantial contribution of the oxygen *p* states of the bridging hydroxyl group (located between diradical motifs) to the midgap states (Fig. 5e) shows the important role of –OH groups in stabilizing the FM GS through the coupling between magnetic diradical motifs. The importance of –OH functionalization in self-sustainability of magnetic ordering is further demonstrated by the fact that fully fluorinated analogue of the *m*-xylylene motif, that is, the system comprising *m*-xylylene-like sp^2 island surrounded by a fully fluorinated sp^3 network, is predicted to have a paramagnetic GS with an AFM-FM spin-flip energy of 0.001 eV (ref. 43). Introduction of a single –OH group to the supercell only slightly enhances the stability of the *m*-xylylene motif's FM state, by about -0.03 eV with respect to its fully fluorinated counterpart. A more significant stabilization of the FM GS was observed when two hydrogen-bonded –OH groups were introduced in close proximity to the sp^2 island; this increased the stability of the FM state relative to the AFM state by 0.08 eV. In addition, a strong overlap of the –OH and –F orbitals in a broad binding energy range starting from −18.5 eV highlights the importance of –OH groups preventing migration of fluorine atoms over the graphene surface and suppressing formation of non-magnetic islands, which are formed in partially fluorinated graphenes[43,49,50].

The DOS spectra of the AFM phase (Fig. 5f) are virtually identical as those for FM one up to the valence band maximum. The important differences appear in the occupation of the midgap states. The occupied (unoccupied) spin-up (spin-down) states are localized on the C atoms carrying positive spin density, while the opposite occupation resides on the C atoms with negative spin density. As hydroxyl group substantially contributes to the midgap states, we conclude that the AFM superexchange is driven by the magnetic coupling[48,51] in which –OH group plays the significant role. Needless to say that the orientation of the hydroxyl group does not affect the FM-AFM transition observed at $\sim$62 K as both *ab initio* molecular dynamic simulations and arbitrary rotation of the –OH groups did not induce the phase change. Thus, the experimentally observed FM-AFM transition, inherent to organic-based materials with radical motifs[42], is in good agreement with a low-energy gain of superexchange interaction of the FM state, which is inversely proportional[52] to the energy difference between hybridized states ($\sim$2.6 eV).

It is worth to mentioning that magnetism of graphene-based materials is intimately related to the appearance of midgap states in their electronic structure[28,29]. The origin of these midgap states is usually ascribed to defects or edges in the structure of graphene-based materials. Here we first identify the new principal source of magnetism in graphene derivatives based on creation of diradical domains through an appropriate sp^3 functionalization. Such diradical motifs embedded in an sp^3 lattice are thus clearly necessary but not sufficient for maintenance of the magnetic regime, which is further stabilized by the presence of neighbouring –OH groups. They show multiple roles in the system contributing to formation and stabilization of diradical motifs, superexchange interaction among them and suppression of adatoms lateral diffusion.

To support the principle role of –OH groups on magnetism, we further performed a high-temperature treatment of the G(OH)F sample. If it is exposed to a temperature above 200 °C, the room temperature magnetism is lost (after thermal treatment, G(OH)F behaves in a diamagnetic manner; Supplementary Fig. 9) as –OH groups start to leave the structure of G(OH)F (see, for comparison, Supplementary Fig. 3b). It confirms that –OH groups have an essential role on establishing and maintaining magnetically ordered state up to room temperature. In addition, defects such as vacancies, voids and edges cannot be considered as key factors capable to imprint the observed FM and AFM behaviour at low and room temperature, respectively.

Furthermore, we modelled the effect of the partial 3D layering of G(OH)F sheets on the magnetic features of the G(OH)F system. Here the individual layers in bulk G(OH)F samples were supposed to be bound by both dispersive forces and hydrogen-bonding between –OH groups. The theoretical calculations show that the magnetic properties of bulk G(OH)F are identical to those of the monolayered material (Supplementary Fig. 10). This indicates that magnetism of G(OH)F originates from the individual sheets and is not a consequence of their stacking. In other words, the potential contribution of 3D layering to the observed magnetism can be clearly ruled out.

To address the effect of chemical composition (OH and F contents) on magnetic properties of hydroxofluorographenes, we then constructed the magnetization map based on density functional theory (DFT) calculations for the $C_{18}(OH)_yF_x$ basic studied cell (Fig. 6). The magnetization map shows the propensity for the formation of FM ground states as a function of the F and OH content of the material (as also listed in Supplementary Table 2). Importantly, there are regions corresponding to the magnetically ordered FM ground states ranging from green to magnetically strongest red parts depending on the particular composition. Nevertheless, the blue regions corresponding to non-magnetic states are also present in a significant portion—the fact evidencing for a principal effect of chemical composition on magnetic features of G(OH)F system. In particular, two magnetically interesting islands appear, that is, upper island corresponding to G(OH)F systems with relatively high sp^3 functionalization (above $\sim$50%) and higher OH and F contents and lower island with considerably lower degree of sp^3 functionalization, centred at the $C_{18}F_4$ stoichiometry, surprisingly with very low OH content. Importantly, the stoichiometry of the G(OH)F sample, thoroughly discussed above, lies within the region of the upper island (sample denoted as No. 1 in the magnetization map in Fig. 6), where the magnetism originates from the presence of sp^2-conjugated diradical motifs embedded in an sp^3 matrix. Computational predictions are thus consistent with available experimental data. In this region, the $sp^3/(sp^2+sp^3)$ ratio is above the site percolation limit of honeycomb lattice (0.697)[52], which indicates that the number of sp^3 atoms is sufficient (above 5.5 for the supercell containing 18 carbon atoms) to cage the sp^2 islands.

To confirm the presence of diradical motifs experimentally, we prepared and measured the electron paramagnetic resonance (EPR) spectra (Supplementary Fig. 11) for the $C_{18}F_{11.5}$ sample whose $sp^3/(sp^2+sp^3)$ ratio was above the percolation limit (0.735), favouring the emergence of diradical motifs according to our theory. This sample exhibited a similar level of sp^3 functionalization like G(OH)F sample, which is, however, antiferromagnetic ($S=0$) and thus EPR silent. The EPR resonances recorded at two different temperatures clearly indicate the presence of radical species. In particular, overlapping signals originating from uncoupled $S=1/2$ centres (strong resonance signals around $g\approx2$) together with spin-coupled $S=1/2$ systems were observed, leading to the formation of triplet species ($S=1$). The EPR signatures of $S=1$ systems exhibited small E/D ratios (about 0.1) and became clearly visible upon lowering the temperature. The axial zero-field-splitting parameter (D) for the $S=1$ system was found to be equal to $\sim$790 MHz, which corresponds to an average distance of $\sim$4.6 Å between the interacting $S=1/2$ spins (point-dipole approach). Note that the distance between the two interacting $S=1/2$ spins corresponds well with the distance between the methylene groups in the *m*-xylylene motif ($\sim$4.887 Å). The EPR data thus unambiguously confirmed the presence of diradical motifs in fluorographene systems of sufficiently high sp^3 content.

To validate the theoretical magnetization map, we further prepared four additional samples (samples denoted as No. 2–No. 5 in Fig. 6) exploiting various reaction conditions and –OH sources (for details, see 'Methods' section below) and determined their chemical composition by XPS (Supplementary Figs 12 and 13). Here it is worth noting that the experimental scope for preparing the strongest magnetic systems will be limited by thermodynamics (Supplementary Fig. 14) and ability to prepare hydroxofluorographene systems with suitable and stable distributions of –OH and –F moieties (in this context, the facile migration of fluorines in lightly fluorinated graphenes may be problematic[43]). Nevertheless, the magnetic properties of all four additional derivatives with chemical compositions of $C_{18}(OH)_{1.5}F_6$, $C_{18}(OH)_2F_3$, $C_{18}(OH)_{2.6}F_{4.7}$ and $C_{18}(OH)_{2.4}F_7$

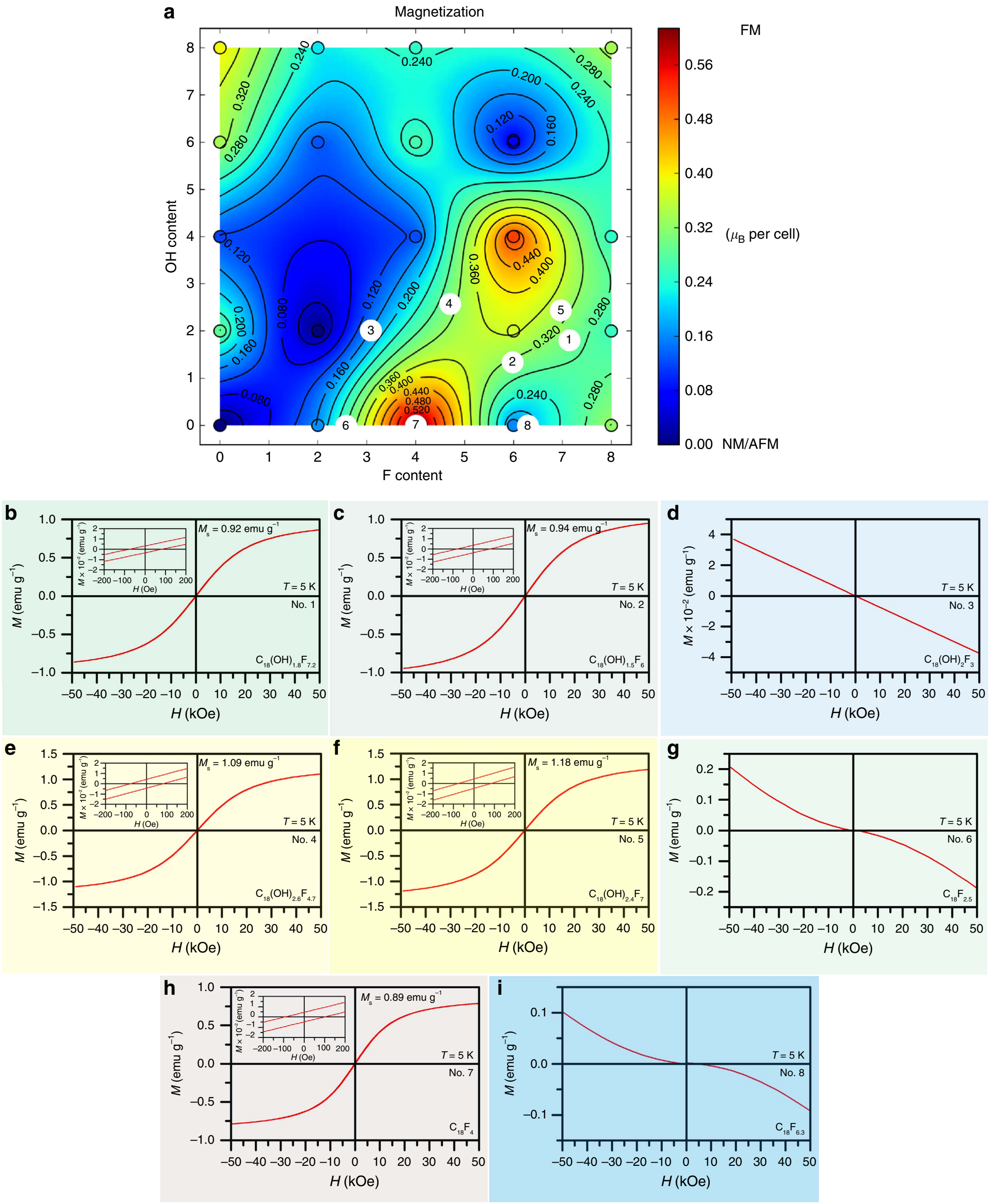

fit to the magnetization map with an excellent correlation and confirm the profound influence of the $C_{18}(OH)_yF_x$ stoichiometry (Fig. 6 and Supplementary Figs 12 and 13). In particular, $C_{18}(OH)_2F_3$ is a diamagnet, in full accordance with the map (it lies in one of the blue regions in Fig. 6). Conversely, $C_{18}(OH)_{1.5}F_6$, $C_{18}(OH)_{2.6}F_{4.7}$ and $C_{18}(OH)_{2.4}F_7$ are magnetically sustainable 2D materials with an FM GS (all lying in green-yellow region) and very similar transition temperature to the AFM state at ~62 K. The identical transition temperature, thus independent on chemical composition, is viewed as another proof of the same source of magnetism based on diradical motifs. The slight changes in saturation magnetization (from ~0.9 to ~1.2 emu g^{-1}; Fig. 6) stem from different strength of superexchange interactions associated to the content of –OH groups.

To further validate our theory, provide additional support for the essential role of –OH groups in the magnetism of hydroxofluorographenes, and explore the potentially different origins of magnetism in fluorographene and hydroxofluorographene systems, we also synthesized three partially fluorinated fluorographenes without –OH groups by simple thermal defluorination of the exfoliated C_1F_1 sample (for details on synthesis, see the 'Methods' section). The stoichiometries of these new systems are $C_{18}F_{2.5}$, $C_{18}F_4$ and $C_{18}F_{6.3}$ and the samples are denoted as No. 6, 7 and 8, respectively, in the magnetization map in Fig. 6 (for detailed XPS and magnetic characterization, see Supplementary Figs 15, 16 and 17). In full agreement with the magnetization map derived from our computational studies (Fig. 6), $C_{18}F_{2.5}$ is diamagnetic but contains some paramagnetic centres in perfect correspondence with the work by Nair *et al.*[43] reporting such behaviour for fluorographenes with lower fluorine coverages. Importantly, beyond the study by Nair *et al.*[43], the $C_{18}F_4$ exhibits even an FM GS as predicted by our magnetic model and experimentally confirmed (Fig. 6). However, it undergoes a transition to a paramagnetic state with the Curie temperature of 22 K. The different nature of transition temperature and inability to maintain magnetic ordering up to room temperature imply the different origin of magnetism in fluorographenes compared with hydroxofluorographenes. In particular, the structure of $C_{18}F_4$ can be considered as sp^3 structural defect in the sp^2 graphene lattice (Supplementary Fig. 18). This is further confirmed experimentally by detailed magnetic analysis of $C_{18}F_4$ (Supplementary Fig. 17). In particular, the temperature evolution of coercivity and saturation magnetization of $C_{18}F_4$ agrees very closely with predictions based on theoretical expressions for magnetism due to *d*-electrons (that is, models based on Brillouin and Bloch functions), implying that its magnetism is due to localized defect-induced magnetic moments[53,54]. These results starkly contrast with our observations for G(OH)F systems that exhibit room temperature magnetic ordering, whose experimental saturation magnetization and coercivity data cannot be fitted using models based on expressions for *d*-electron magnetism. Finally, the $C_{18}F_{6.3}$ sample is again diamagnetic with some paramagnetic centres in agreement with the theoretical magnetization map (Fig. 6). Here the magnetic ordering is lost due to a lack of conduction electrons related to the increased degree of functionalization.

The comparison of magnetic behaviour of GF and G(OH)F systems demonstrates the differences between the 'defect-induced magnetism' observed for GF systems with lower levels of sp^3 functionalization and the 'diradical motif-based magnetism' observed in the highly functionalized G(OH)F system. At the same time, these data show that our theoretical model (that is, the magnetization map presented in Fig. 6) is robust, universal and capable of explaining the behaviour of both system types with different origins of magnetism.

In summary, we report a new class of graphene derivatives, which behave as antiferromagnetic materials at room temperature, representing examples of *sp*-based systems with room temperature magnetism. They become ferromagnets as the temperature is lowered showing remarkable magnetization. These organic magnets are prepared via simple, scalable and controllable reactions of fluorographene with suitable –OH-containing organic precursors. An interplay between thermodynamically preferred defluorination and nucleophilic substitution affects the products' final stoichiometry and thus their magnetic features. The magnetism in hydroxofluorographenes with an appropriate stoichiometry stems from the presence of diradical motifs coupled via superexchange interactions and stabilized by –OH groups, which also mediate the coupling. The newly constructed theoretical model addresses the effect of system stoichiometry on magnetic features in an excellent agreement with experimental data. More importantly, this robust model has a universal character covering the aspects of the 'defect-induced magnetism' and 'diradical motif-triggered magnetism' appearing in the field of graphene magnetism depending on degree of sp^3 functionalization.

We believe that this work would open the doors for preparing a wider family of graphene-based 2D room temperature magnets whose magnetic properties can be tuned by controlling the sp^3 functionalization. Definitely, the theoretical model based on diradical motifs communicating through superexchange interactions should be further extended also for other graphene-based systems. The developed room temperature carbon magnets also offer a huge space for testing in potential applications in various fields including, for example, spintronics and magnetically separable nanocarriers.

Methods

Chemicals. Fluorinated graphite (C_1F_1) and tetramethylammonium hydroxide (25% w/w aqueous solution) were purchased from Sigma-Aldrich. Partly fluorinated graphites ($C_1F_{0.55}$ and $C_1F_{0.8}$) were purchased from Alfa Aesar.

Figure 6 | Magnetic properties as a function of $C_{18}(OH)_yF_x$ stoichiometry. (**a**) The mean magnetization map indicates which $C_{18}(OH)_yF_x$ ($x = 0$–8, $y = 0$–8) stoichiometries are likely to exist in ferromagnetic and non-magnetic ground states. Both -F and -OH groups are assumed to be randomly distributed across the sample (as suggested by STEM-HAADF elemental mapping, cf. Fig. 3) at zero temperature and the possibility of kinetically controlled -F/-OH migration is not considered. The white circles indicate experimentally studied samples: 1—$C_{18}(OH)_{1.8}F_{7.2}$ (ferromagnetic in the ground state), 2—$C_{18}(OH)_{1.5}F_6$ (ferromagnetic in the ground state), 3—$C_{18}(OH)_2F_3$ (diamagnetic in the ground state), 4—$C_{18}(OH)_{2.6}F_{4.7}$ (ferromagnetic in the ground state), 5—$C_{18}(OH)_{2.4}F_7$ (ferromagnetic in the ground state), 6—$C_{18}F_{2.5}$ (diamagnetic in the ground state), 7—$C_{18}F_4$ (ferromagnetic in the ground state) and 8—$C_{18}F_{6.3}$ (diamagnetic in the ground state). (**b**) The isothermal magnetization (*M*) curve of $C_{18}(OH)_{1.8}F_{7.2}$ (Sample No. 1) as a function of an external magnetic field (*H*), recorded at a temperature of 5 K. (**c**) *M* versus *H* curve of $C_{18}(OH)_{1.5}F_6$ (Sample No. 2), recorded at a temperature of 5 K. (**d**) *M* versus *H* curve of $C_{18}(OH)_2F_3$ (Sample No. 3), recorded at a temperature of 5 K. (**e**) *M* versus *H* curve of $C_{18}(OH)_{2.6}F_{4.7}$ (Sample No. 4), recorded at a temperature of 5 K. (**f**) *M* versus *H* curve of $C_{18}(OH)_{2.4}F_7$ (Sample No. 5), recorded at a temperature of 5 K. (**g**) *M* versus *H* curve of $C_{18}F_{2.5}$ (Sample No. 6), recorded at a temperature of 5 K. (**h**) *M* versus *H* curve of $C_{18}F_4$ (Sample No. 7), recorded at a temperature of 5 K. (**i**) *M* versus *H* curve of $C_{18}F_{6.3}$ (Sample No. 8), recorded at a temperature of 5 K. The insets in panel (**b**,**c**,**e**,**f** and **h**) show the behaviour of the respective hysteresis loops around the origin with the saturation magnetization (M_S) indicated.

DMF (p.a. grade) was obtained from PENTA, Czech Republic, and used without further purification.

Detailed synthesis of samples. To synthesize a few-layered fluorographene (GF) dispersion in DMF, fluorinated graphite (C:F, 1:1) (250 mg, Aldrich, grey powder) was suspended in 50 ml DMF. The mixture was sonicated for 2 h in an ultrasound bath and the temperature of the bath was kept below 30 °C. The suspension was then left to stand for 1 day to allow any undispersed material to settle. The clear, pale grey supernatant colloid was then collected and used in the preparation of hydroxofluorographene.

To synthesize hydroxofluorographene (G(OH)F, $C_{18}(OH)_{1.8}F_{7.2}$), 2 g of an aqueous tetramethylammonium hydroxide solution (25% w/w, Aldrich) was added to 50 ml of a fluorographene (C_1F_1) dispersion in DMF (prepared as described above) with a concentration of 0.8 mg ml^{-1}. The base initially precipitates in DMF but the precipitate gradually dissolves upon stirring. After 3 days' stirring at room temperature in a sealed vessel, the suspension was centrifuged at 5,000 r.p.m. for 10 min. The centrifuged solid was washed several times with water until its pH became neutral and then re-suspended in 6–8 ml water by sonication in an ultrasound bath (45 min). This dispersion was left to stand for 1 day to allow undispersed particles to settle and then centrifuged at 1,000 r.p.m. for 20 min to yield a clear black colloid containing aqueous dispersed hydroxofluorographene layers. Completely the same synthetic procedure was also applied to prepare hydroxofluorographenes ($C_{18}(OH)_2F_3$ and $C_{18}(OH)_{1.5}F_6$, respectively) from partly fluorinated graphites ($C_1F_{0.55}$ and $C_1F_{0.8}$, respectively).

Among several pathways tested for obtaining different hydroxylated graphene fluoride derivatives, two such reactions are described, as more appropriate for the scope of the present work. To synthesize $C_{18}(OH)_{2.6}F_{4.7}$, 50 mg of graphite fluoride was dispersed in 2 ml DMF and 0.7 ml H_2O_2 (30%, Aldrich) was added. The $C_{18}(OH)_{2.4}F_7$ sample was prepared by adding 0.7 ml tert-butyl hydroperoxide solution in decane (5.0–6.0 M, Aldrich) and 50 mg potassium tert-butoxide (Aldrich) in a 50 mg graphite fluoride dispersion in 2 ml DMF. Both mixtures were heated under stirring at 90 °C for 3 days. Work up of products was performed similarly with the previous ones.

Partially fluorinated fluorographenes, that is, with a composition of $C_{18}F_{2.5}$, $C_{18}F_4$ and $C_{18}F_{6.3}$, and the sample with the composition of $C_{18}F_{11.5}$ used for the EPR measurements, were obtained by thermal treatment of commercial fluorinated graphite under inert atmosphere at 800 °C for 4 h, at 625 °C for 4 h, at 550 °C for 5 h and at 550 °C for 1 h 52 min, respectively. The thermal treatments were performed in an open α-Al_2O_3 crucible using a Netzsch STA 449C Jupiter instrument. A temperature programme with a heating rate of 5 °C min^{-1} (10 °C min^{-1} for $C_{18}F_{11.5}$) from 40 °C to the final temperature was used. According to XPS analysis, the samples presented also small amounts of nitrogen and oxygen (atomic content, $C_{18}F_{2.5}$: N 2.0%, O 2.1%; $C_{18}F_4$: N 1.0%, O 1.4%; $C_{18}F_{6.3}$: O 0.6%; $C_{18}F_{11.5}$: O 3.1%).

Thermal annealing of G(OH)F. G(OH)F was thermally annealed by heating under inert atmosphere from room temperature to 220 °C at a rate of 5 °C min^{-1}, with a subsequent 3 h isotherm at 220 °C.

Characterization techniques. The exact composition of the precursors ($C_1F_{0.55}$, $C_1F_{0.8}$ and C_1F_1) and derived G(OH)F and partially fluorinated graphene (that is, $C_{18}F_x$, $x = 2.5$, 4, 6.3 and 11.5) samples was determined by XPS carried out with a PHI VersaProbe II (Physical Electronics) spectrometer using an Al K$_\alpha$ source (15 kV, 50 W). The obtained data were evaluated with the MultiPak (Ulvac-PHI, Inc.) software package. The detection of residual metal content in the G(OH)F sample was performed by ICP-MS. The exact amount of the G(OH)F sample (10 mg) was immersed in a concentrated nitric acid (≥99.999% trace metals basis) and heated for 2 h at 100 °C. Afterwards, the mixture was transferred into 10 ml volumetric flask, diluted with water and the undissolved graphene was caught by a 200 nm Millipore filter. The obtained concentration of metals in the solution was recalculated to the amount of the tested sample (analogically, diluted nitric acid was used as a blank). FT-IR spectra were obtained using an iS5 FT-IR spectrometer (Thermo Nicolet) with a Smart Orbit ZnSe ATR technique (650–4,000 cm^{-1}). Raman spectra were recorded on a DXR Raman microscope using the 532 nm excitation line of a diode laser. HRTEM images were obtained using an FEI TITAN 60–300 HRTEM microscope with an X-FEG type emission gun, operating at 300 kV. STEM–HAADF analyses for EDX mapping of elemental distributions on the G(OH)F sheets were performed with an FEI TITAN 60–300 HRTEM microscope operating at 80 kV. For HRTEM, STEM–HAADF and EDX experiments, an aqueous solution of G(OH)F with a concentration of 0.1 mg ml^{-1} was redispersed by ultrasonication for 5 min. A drop of the sonicated sample was then deposited on a carbon-coated copper grid and slowly dried at laboratory temperature for 24 h to reduce its content of adsorbed water. Atomic force microscopy images and appropriate height profiles were recorded in semi-contact mode (HA-NC tips, mica substrate) on an NTEGRA Aura instrument. Thermogravimetric analysis and evolved gas analysis were performed on a STA449 C Jupiter-Netzsch instrument with a heating rate of 1 °C min^{-1}. The masses of released gases in the range of 12–60 m/z were determined with a QMS 403 Aolos mass spectrometer (Netzsch), starting at 100 °C to avoid overloading the spectrometer with adsorbed water. A superconducting quantum interference device magnetometer (MPMS XL-7 type, Quantum Design, USA) was employed for the magnetization measurements. The temperature dependence of the magnetization of tetramethylammonium hydroxide, C_1F_1 precursor and seven final products (that is, $C_{18}(OH)_2F_3$, $C_{18}(OH)_{1.5}F_6$, $C_{18}(OH)_{2.6}F_{4.7}$, $C_{18}(OH)_{2.4}F_7$, $C_{18}F_{2.5}$, $C_{18}F_4$ and $C_{18}F_{6.3}$) was recorded in the sweep mode over the temperature interval from 5 to 300 K under an external magnetic field of 10 kOe; the temperature evolution of magnetization of the $C_{18}(OH)_{1.8}F_{7.2}$ sample was monitored in the sweep mode over the temperature interval from 5 to 400 K and back under an external magnetic field of 10 kOe. The hysteresis loops of the $C_{18}(OH)_{1.8}F_{7.2}$ and $C_{18}F_4$ samples were measured at a series of temperatures in the interval from 5 to 400 K and from 5 to 300 K, respectively, in external magnetic fields ranging from −50 to +50 kOe. The hysteresis loops of the $C_{18}(OH)_2F_3$, $C_{18}(OH)_{1.5}F_6$, $C_{18}(OH)_{2.6}F_{4.7}$, $C_{18}(OH)_{2.4}F_7$, $C_{18}F_{2.5}$ and $C_{18}F_{6.3}$ samples were measured at a temperature of 5 K and in external magnetic fields from −50 to +50 kOe. The magnetization values were corrected assuming the response of the sample holder, sample capsule and respective Pascal constants. EPR spectra were recorded on a JEOL JES-X-320 operating at X-band frequency (~9.15 GHz), equipped with a variable temperature control ES 13060DVT5 apparatus, and were performed on the powder $C_{18}F_{11.5}$ sample (~2 mg loaded onto the EPR tube). The cavity Q quality factor was kept above 6,000, highly pure quartz tube was employed (Suprasil, Wilmad, <0.5 OD) to load the sample powders. The g value accuracy was obtained by comparing the resonance signals of the $C_{18}F_{11.5}$ sample with that of MnO standard (JEOL-internal standard). The experimental conditions for measuring EPR spectra were adjusted as follows: frequency = 9.15584 GHz, modulation frequency = 100 kHz, modulation amplitude = 0.8 mT, time constant = 30 ms, applied microwave power = 0.8 mW, sweep time = 480 s and phase = 0°s.

Computational methods. Atomistic calculations were performed using the spin-polarized DFT and projected augmented wave potentials representing atomic cores as implemented in the VASP package[55–57]. The PBE xc functional[58] was used with a plane wave cutoff of 500 eV. The Brillouin zone integrations were performed with 2 × 2 × 1 (structure and cell optimization) and 10 × 10 × 1 (final runs; magnetism) Γ point-centred k-point Monkhorst-Pack meshes[59] per 3 × 3 supercell. The electronic density of states was calculated using the tetrahedron method[60] employed denser k-point sampling 16 × 16 × 1. Open circles in Fig. 6 label the explored 21 unique stoichiometries $C_{18}(OH)_yF_x$. For each stoichiometry at least 64 random structures were generated. The optimized structures were converged to energy of less than 10^{-4} eV, and a convergence criterion of 10^{-6} eV for each SCF cycle. The thermodynamic stability of all reported configurations was analysed in terms of the stabilization energy $E_{stab} = [E(\text{model}) - N_F{}^*E(F) - N_{OH}{}^*E(OH) - N_C{}^*E(C)]/(N_F + N_{OH} + N_C)$, where E(model), E(F) and E(OH) denote the total energy of the supercell model, F atom, –OH group and C atom, respectively and N_F, N_{OH} and N_C denote the number of F atoms, –OH groups and C atoms, respectively. The spin coupling constant or spin-flip gap per supercell was calculated as $E_{SF} = E_{LS} - E_{HS}$, where E_{LS} and E_{HS} are the total low-spin and total high-spin energy for a given configuration, respectively. The mean magnetization was obtained as average over 32 low-energy samples from 64 per cell as a function of x and y in the formula of $C_{18}(OH)_yF_x$. The colour-coded maps were generated by linear fitting among valid data points represented by circles.

To address the role of 3D stacking on the magnetic properties of the G(OH)F system, calculations including vdW-correction DFT-D3 of Grimme[61] were carried out for a hypothetical bulk. We considered typical stacking patterns, namely AA and AB; the relaxed interlayer distance for the most energetically stable structure was 5.9 Å. The energetically most stable structure together with the corresponding density of states plot is presented in Supplementary Fig. 10.

Data availability. The data that support the findings of this study are available from the corresponding author upon request.

References

1. Novoselov, K. S. *et al.* Electric field effect in atomically thin carbon films. *Science* **306,** 666–669 (2004).
2. Novoselov, K. S. *et al.* Two-dimensional gas of massless Dirac fermions in graphene. *Nature* **438,** 197–200 (2005).
3. Zhang, Y. B., Tan, Y. W. & Stormer, H. L. Experimental observation of the quantum Hall effect and Berry's phase in graphene. *Nature* **438,** 201–204 (2005).
4. Lee, C., Wei, X. D., Kysar, J. W. & Hone, J. Measurement of the elastic properties and intrinsic strength of monolayer graphene. *Science* **321,** 385–388 (2008).
5. Castro Neto, A. H., Guinea, F., Peres, N. M. R., Novoselov, K. S. & Geim, A. K. The electronic properties of graphene. *Rev. Modern Phys.* **81,** 109–162 (2009).
6. Balandin, A. A. *et al.* Superior thermal conductivity of single-layer graphene. *Nano Lett.* **8,** 902–907 (2008).
7. Kane, C. L. & Mele, E. J. Quantum spin Hall effect in graphene. *Phys. Rev. Lett.* **95,** 226801 (2005).

8. Geim, A. K. & Novoselov, K. S. The rise of graphene. *Nat. Mater.* **6,** 183–191 (2007).
9. Stoller, M. D., Park, S. J., Zhu, Y. W., An, J. H. & Ruoff, R. S. Graphene-based ultracapacitors. *Nano Lett.* **8,** 3498–3502 (2008).
10. Nair, R. R. *et al.* Fine structure constant defines visual transparency of graphene. *Science* **320,** 1308 (2008).
11. Tse, W. K. & MacDonald, A. H. Giant magneto-optical Kerr effect and universal Faraday effect in thin-film topological insulators. *Phys. Rev. Lett.* **105,** 057401 (2010).
12. Fialkovsky, I. V., Marachevsky, V. N. & Vassilevich, D. V. Finite-temperature Casimir effect for graphene. *Phys. Rev. B* **84,** 035446 (2011).
13. Georgakilas, V., Perman, J. A., Tucek, J. & Zboril, R. Broad family of carbon nanoallotropes: classification, chemistry, and applications of fullerenes, carbon dots, nanotubes, graphene, nanodiamonds, and combined superstructures. *Chem. Rev.* **115,** 4744–4822 (2015).
14. Bae, S. *et al.* Roll-to-roll production of 30-inch graphene films for transparent electrodes. *Nat. Nanotechnol.* **5,** 574–578 (2010).
15. Tapaszto, L., Dobrik, G., Lambin, P. & Biro, L. P. Tailoring the atomic structure of graphene nanoribbons by scanning tunnelling microscope lithography. *Nat. Nanotechnol.* **3,** 397–401 (2008).
16. Han, W., Kawakami, R. K., Gmitra, M. & Fabian, J. Graphene spintronics. *Nat. Nanotechnol.* **9,** 794–807 (2014).
17. Sun, Z. H. & Chang, H. X. Graphene and graphene-like two-dimensional materials in photodetection: Mechanisms and methodology. *ACS Nano* **8,** 4133–4156 (2014).
18. Liu, Z. F. *et al.* Organic photovoltaic devices based on a novel acceptor material: Graphene. *Adv. Mater.* **20,** 3924–3930 (2008).
19. Wu, J. B. *et al.* Organic light-emitting diodes on solution-processed graphene transparent electrodes. *ACS Nano* **4,** 43–48 (2010).
20. Xu, Y. X. *et al.* Holey graphene frameworks for highly efficient capacitive energy storage. *Nat. Commun.* **5,** 4554 (2014).
21. Zhao, M. Q. *et al.* Unstacked double-layer templated graphene for high-rate lithium-sulphur batteries. *Nat. Commun.* **5,** 3410 (2014).
22. Georgakilas, V. *et al.* Functionalization of graphene: covalent and non-covalent approaches, derivatives and applications. *Chem. Rev.* **112,** 6156–6214 (2012).
23. Joshi, R. K., Alwarappan, S., Yoshimura, M., Sahajwalla, V. & Nishina, Y. Graphene oxide: the new membrane material. *Appl. Mater. Today* **1,** 1–12 (2015).
24. Elias, D. C. *et al.* Control of graphene's properties by reversible hydrogenation: evidence for graphane. *Science* **323,** 610–613 (2009).
25. Zboril, R. *et al.* Graphene fluoride: a stable stoichiometric graphene derivative and its chemical conversion to graphene. *Small.* **24,** 2885–2891 (2010).
26. Urbanova, V. *et al.* Thiofluorographene-hydrophilic graphene derivative with semiconducting and genosensing properties. *Adv. Mater.* **27,** 2305–2310 (2015).
27. Dubecky, M. *et al.* Reactivity of fluorographene: a facile way toward graphene derivatives. *J. Phys. Chem. Lett.* **6,** 1430–1434 (2015).
28. Kuila, T. *et al.* Chemical functionalization of graphene and its applications. *Prog. Mater. Sci.* **57,** 1061–1105 (2012).
29. Yazyev, O. V. Emergence of magnetism in graphene materials and nanostructures. *Rep. Prog. Phys.* **73,** 056501 (2010).
30. Palacios, J. J., Fernandez-Rossier, J. & Brey, L. Vacancy-induced magnetism in graphene and graphene ribbons. *Phys. Rev. B* **77,** 195428 (2008).
31. Yazyev, O. V. & Helm, L. Defect-induced magnetism in graphene. *Phys. Rev. B* **75,** 125408 (2007).
32. Ito, Y. *et al.* Tuning the magnetic properties of carbon by nitrogen doping of its graphene domains. *J. Am. Chem. Soc.* **137,** 7678–7685 (2015).
33. Tuček, J. *et al.* Sulfur doping induces strong ferromagnetic ordering in graphene: effect of concentration and substitution mechanism. *Adv. Mater.* **28,** 5045–5053 (2016).
34. Magda, G. Z. *et al.* Room-temperature magnetic order on zigzag edges of narrow graphene nanoribbons. *Nature* **514,** 608–611 (2014).
35. Khurana, G., Kumar, N., Kotnala, R. K., Nautiyal, T. & Katiyar, R. S. Temperature tuned defect induced magnetism in reduced graphene oxide. *Nanoscale* **5,** 3346–3351 (2013).
36. Eng, A. Y. S. *et al.* Searching for magnetism in hydrogenated graphene: using highly hydrogenated graphene prepared *via* birch reduction of graphite oxides. *ACS Nano* **7,** 5930–5939 (2013).
37. Zhou, J. *et al.* Ferromagnetism in semihydrogenated graphene sheet. *Nano Lett.* **9,** 3867–3870 (2009).
38. Gonzalez-Herrero, H. *et al.* Atomic-scale control of graphene magnetism by using hydrogen atoms. *Science* **352,** 437–441 (2016).
39. Li, Y., Ren, J. C., Zhang, R. Q., Lin, Z. J. & van Hove, M. A. Atomic nitrogen chemisorption on graphene with extended line defects. *J. Mater. Chem.* **22,** 21167–21172 (2012).
40. Wang, Z. G., Qin, S. J., Wang, C. L. & Hui, Q. Fluorine adsorption on the graphene films: from metal to insulator. *Comput. Mater. Sci.* **97,** 14–19 (2015).
41. Cao, C., Wu, M., Jiang, J. Z. & Cheng, H. P. Transition metal adatom and dimer adsorbed on graphene: Induced magnetization and electronic structures. *Phys. Rev. B* **81,** 205424 (2010).
42. Nair, R. R. *et al.* Dual origin of defect magnetism in graphene and its reversible switching by molecular doping. *Nat. Commun.* **4,** 2010 (2013).
43. Nair, R. R. *et al.* Spin-half paramagnetism in graphene induced by point defects. *Nat. Phys.* **8,** 199–202 (2012).
44. Nair, R. R. *et al.* Fluorographene: a two-dimensional counterpart of teflon. *Small.* **6,** 2877–2884 (2010).
45. Cho, D., Ko, K. C. & Lee, J. Y. Organic magnetic diradicals (radical-coupler-radical): standardization of couplers for strong ferromagnetism. *J. Phys. Chem. A* **118,** 5112–5121 (2014).
46. Rajca, A. Organic diradicals and polyradicals: from spin coupling to magnetism? *Chem. Rev.* **94,** 871–893 (1994).
47. Lieb, E. H. 2 theorems on the Hubbard model. *Phys. Rev. Lett.* **62,** 1201–1204 (1989).
48. Belhadji, B. *et al.* Trends of exchange interactions in dilute magnetic semiconductors. *J. Phys. Condens. Matter* **19,** 436227 (2007).
49. Ao, Z. *et al.* Enhancement of the stability of fluorine adatoms on defective graphene and at graphene/fluorographene interface. *ACS Appl. Mater. Interfaces* **7,** 19659–19665 (2015).
50. Sadeghi, A., Neek-Amal, M. & Peeters, F. M. Diffusion of fluorine on and between graphene layers. *Phys. Rev. B* **91,** 014304 (2015).
51. Kim, S. W., Kim, H. J., Choi, J. H., Scheicher, R. H. & Cho, J. H. Contrasting interedge superexchange interactions of graphene nanoribbons embedded in h-BN and graphene. *Phys. Rev. B* **92,** 035443 (2015).
52. Feng, X. M., Deng, Y. J. & Blote, H. W. J. Percolation transitions in two dimensions. *Phys. Rev. E* **78,** 031136 (2008).
53. Makarova, T. L. *et al.* Edge state magnetism in zigzag-interfaced graphene *via* spin susceptibility measurements. *Sci. Rep.* **5,** 13382 (2015).
54. Enoki, T. & Takai, K. The edge state of nanographene and the magnetism of the edge-state spins. *Solid State Commun.* **149,** 1144 (2009).
55. Kresse, G. & Furthmüller, J. Efficient iterative schemes for ab initio total-energy calculations using a plane-wave basis set. *Phys. Rev. B* **54,** 11169–11186 (1996).
56. Kresse, G. & Joubert, D. From ultrasoft pseudopotentials to the projector augmented-wave method. *Phys. Rev. B* **59,** 1758–1775 (1999).
57. Blöchl, P. E. Projector augmented-wave method. *Phys. Rev. B* **50,** 17953–17979 (1994).
58. Perdew, J. P., Burke, K. & Ernzerhof, M. Generalized gradient approximation made simple. *Phys. Rev. Lett.* **77,** 3865–3868 (1996).
59. Monkhorst, H. J. & Pack, J. D. Special points for Brillouin-zone integrations. *Phys. Rev. B* **13,** 5188–5192 (1976).
60. Blöchl, P. E., Jepsen, O. & Andersen, O. K. Improved tetrahedron method for Brillouin-zone integrations. *Phys. Rev. B* **49,** 16223–16233 (1994).
61. Grimme, S., Antony, J., Ehrlich, S. & Krieg, S. A consistent and accurate ab initio parametrization of density functional dispersion correction (dft-d) for the 94 elements H-Pu. *J. Chem. Phys.* **132,** 154104 (2010).

Acknowledgements

The authors acknowledge the support from the Ministry of Education, Youth and Sports of the Czech Republic (LO1305) and the assistance provided by the Research Infrastructure NanoEnviCz, supported by the Ministry of Education, Youth and Sports of the Czech Republic under Project No. LM2015073. M.O. acknowledges the Neuron fund for supporting science and the Czech Science Foundation (P208/12/G016) and ERC grant (ERC-2015-CoG). The authors deeply thank Dr. Giorgio Zoppellaro (from the Regional Centre of Advanced Technologies and Materials, Faculty of Science, Palacky University in Olomouc, Czech Republic) for measuring and interpreting the EPR spectra. The authors also thank Dr. Joelle Hoggan and her team at Sees-editing Ltd., UK, for professional language corrections of the manuscript.

Author contributions

J.T. performed magnetization data analysis and participated in writing the manuscript, K.H. prepared the samples and performed data analysis, A.B.B. and J.U. prepared the samples, A.B. prepared the samples and performed data analysis, P.B., M.D. and F.K. carried out theoretical computations and participated in writing the manuscript, V.R. performed Raman and FT-IR measurements, K.C. performed microscopic experiments, M.O. carried out theoretical computations and participated in writing the manuscript and R.Z. came with the idea of imprinting magnetism to a graphene-based system through functionalization, designed the experiments and participated in writing the manuscript.

Additional information

Supplementary Information accompanies this paper at http://www.nature.com/naturecommunications

Competing financial interests: The authors declare no competing financial interests.

Reprints and permission information is available online at http://npg.nature.com/reprintsandpermissions/

How to cite this article: Tuček, J. *et al.* Room temperature organic magnets derived from *sp*^{3} functionalized graphene. *Nat. Commun.* **8,** 14525 doi: 10.1038/ncomms14525 (2017).

Publisher's note: Springer Nature remains neutral with regard to jurisdictional claims in published maps and institutional affiliations.

This work is licensed under a Creative Commons Attribution 4.0 International License. The images or other third party material in this article are included in the article's Creative Commons license, unless indicated otherwise in the credit line; if the material is not included under the Creative Commons license, users will need to obtain permission from the license holder to reproduce the material. To view a copy of this license, visit http://creativecommons.org/licenses/by/4.0/

© The Author(s) 2017

Poděkování/ Acknowledgment

Výčet lidí, kterým je záhodno poděkovat, se na tuto stránku nemá šanci vejít. Tak jen ve zkratce. Děkuji svému školiteli, prof. Radku Zbořilovi za trpělivost, důvěru a pomyslný bič, kterým mě hnal dopředu. Děkuji Karlovi a malé Ká, že mě donutil to nevzdat. Velké díky patří také mé rodině, kolegům a přátelům.

I would like to thank to my dear email-consulting supervisor, to Thanos Bourlinos. I appreciate his perspective in the carbon nanoworld so much. I wouldn't agree more with his quote that "the coal is the most useful carbon material of all times and nothing can beat it". My big thank you also goes to my English-speaking colleagues and friends.

Bureaucracy

Bibliographical identification

Author's name: Kateřina Holá

Title: **Functional groups on Carbon Nanomaterials: The Matter That Matters**

Department: Department of Physical Chemistry

Type of thesis: Dissertation

Supervisor: prof. RNDr. Radek Zbořil, Ph.D.

Year: 2017

Abstract: Carbon nanomaterials have a significant importance in materials science worldwide. Their superiority lies in the variability of their main building block, the C–C bond. This unit can build diverse *sp*^{3} and *sp*^{2}-based nanoarchitectures and even covalently incorporate various non-metallic elements. All members of the carbon nanomaterials family (fullerenes, carbon nanotubes, nanodiamonds or graphene) possess extraordinary mechanic, optical, electronic or magnetic properties. In addition, their functionalization can dramatically boost their properties and improve scientific or technical importance in various applications. This dissertation gives a brief view how the functional groups can determine the application potential of current carbon nanomaterials. Mainly, the last frontiers of carbon nanomaterials, fluorographene (GF) and carbon quantum dots (CDs), are discussed in detail. The attention is paid to the functional groups of CDs and how they can affect CD photoluminescence. Similarly, the study focuses how the functional groups on GF can induce magnetism in its honeycomb lattice or boost its genosensing properties. The given results will clearly demonstrate that the functional groups on carbon nanomaterials are the matter that really matters.

Keywords: Carbon Dots, Fluorographene, Origin of Photoluminiscence, Red-shifted fluorescence, Organic magnet, Genosensing, Advanced Applications.

Number of pages: 146
Number of appendixes: 5
Language: English

Bibliografická identifikace

Jméno a příjmení: Kateřina Holá

Title: **Funkční skupiny uhlíkových nanomateriálů**

Pracoviště: Katedra Fyzikální Chemie

Typ práce: Dizertační

Školitel: prof. RNDr. Radek Zbořil, Ph.D.

Rok: 2017

Abstract:

Uhlíkové nanostrukutry představují jedny z nejstudovanějších materiálů současnosti. Jejich neobvyklé vlastnosti jsou dány především variabilitou jejich stavebního prvku, uhlíkovou vazbou. Je to základní kámen rozličných nanomateriálových struktur a zároveň je schopna navázat i mnoho prvků z *p*-bloku. Základní charakteristikou uhlíkových materiálů jsou především jejich výjimečné mechanické, optické, elektronické či magnetické vlastnosti. Tyto vlastnosti však mohou být značně vylepšeny funkčními skupinami, které tak mohou ovlivnit reálné aplikace. Tato práce ve zkratce shrnuje dosavadní znalosti, jak mohou být aplikace uhlíkových nanomateriálů ovlivněny funkčními skupinami. Především se však věnuje uhlíkovým tečkám a fluorografenu. Pozornost je věnována způsobu, jak funkční skupiny ovlivňují fluorescenci uhlíkových teček, jak může hydroxylová skupina ve fluorografenu indukovat magnetismus a také jak sulfhydrylová skupina na fluorografenu může vylepšit elektrochemickou detekci DNA. Uvedené příklady tak jednoznačně ukazují, že velkou roli ve vlastnostech uhlíkových materiálů hrají především jejich funkční skupiny, někdy i větší než uhlíková struktura samotná.

Klíčová slova: Uhlíkové tečky, Fluorografene,Původ fotoluminiscence, Posun fluorescence do červené oblasti, Organický magnet, Genosensing, Pokročilé aplikace.

Počer stánek: 146
Počet příloha: 5
Jazyk: Angličtina